Effect of inoculation, cooling rate and charge composition on gray iron microstructure

Hirš, Ana-Marija; Glavaš, Zoran; Štrkalj, Anita

VIII INTERNATIONAL SCIENTIFIC CONFERENCE

MATERIAL SCIENCE.
NONEQUILIBRIUM PHASE TRANSFORMATIONS

05-08.09.2022, VARNA, BULGARIA

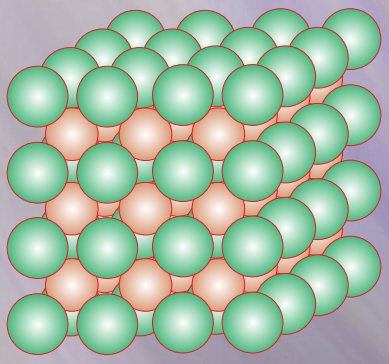

PROCEEDINGS

ISSN 2535-0218 (Print)
ISSN 2535-0226 (Online)

SCIENTIFIC-TECHNICAL UNION OF MECHANICAL ENGINEERING
BULGARIA

1000 Sofia, 108 Rakovski str., office 411,
www.material-science.eu, office@material-science.eu
www.mech-ing.com, phone: +359 2 9877290

VIII INTERNATIONAL SCIENTIFIC CONFERENCE

MATERIAL SCIENCE

„NONEQUILIBRIUM PHASE TRANSFORMATIONS”

05-08 SEPTEMBER, 2022, VARNA, BULGARIA

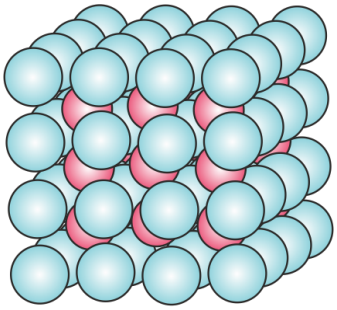

MATERIAL SCIENCE

NONEQUILIBRIUM PHASE TRANSFORMATIONS

YEAR VI ISSUE 1 (5) SEPTEMBER 2022

ISSN: (Print) 2535-0218

ISSN: (Online) 2535-0226

PROCEEDINGS

ORGANIZERS:

SCIENTIFIC TECHNICAL UNION OF MECHANICAL ENGINEERING “INDUSTRY 4.0”

NATIONAL UNIVERSITY OF SCIENCE AND TECHNOLOGY „MISIS” - RUSSIA
INSTITUTE OF METALLURGY AND MATERIALS SCIENCE „A.A.BAIKOV”, RAS - RUSSIA
SCIENTIFIC PRODUCTION ASSOCIATION WBH - GERMANY
TECHNICAL UNIVERSITY VARNA – BULGARIA

INTERNATINOAL EDITORIAL BOARD

C O N T E N T S

Towards the theory of evolution of spherical and ellipsoidal particles in metastable melts and solutions

Margarita A. Nikishina, Eugenya V. Makoveeva, Irina V. Alexandrova, Alexey P. Malygin, Svetlana V. Bulycheva, Dmitri V. Alexandrov
Ural Federal University, Russian Federation
Dmitri.Alexandrov@urfu.ru

Abstract: *This study is concerned with the dynamical laws for particle velocities in supercooled and supersaturated liquids. The cases of spherical and ellipsoidal particle shapes are considered. Also, we consider various growth conditions such as stationary and non-stationary approximations, the shift of crystallization temperature caused by the phase interface curvature, and the kinetics of atoms sticking to the solid-liquid boundary. The dynamical laws under consideration are in good agreement with experiments.*
Keywords*: CRYSTAL GROWTH, PARTICULATE ASSEMBLAGES, METASTABLE LIQUIDS, PHASE TRANSFORMATIONS*

1. Introduction

Experimental data and theory show that the time evolution of particle system in metastable liquids is determined by the growth law of each individual particle. In this case, the properties and structure of the solidified material depend on the behaviour of the whole system of particles as well as on interaction mechanisms between individual particles [1-6]. To simplify the mathematical model, the phase transformation from a supercooled (supersaturated) liquid into a solid is conveniently divided into stages, where one or another dominant factor occurs [7]. Usually, an initial phase is distinguished, where the degree of metastability (supersaturation or supercooling) of the medium remains almost unchanged with time. This is due to the fact that in this phase a small number of particles are formed that cannot drastically change the characteristics of the crystallizing system (e.g. particle size distribution function or degree of metastability). When the number of nucleating and growing particles increases, the system changes its characteristics significantly. For example, the supercooling of a fluid is significantly altered by the release of latent solidification heat in the intermediate phase of the phase transformation [8-11]. Possible inter-particle interaction in the intermediate phase of the process is neglected due to the large distances between the particles. When enough particles are formed, this hypothesis becomes inapplicable and the process proceeds to the final stage where various scenarios of system evolution are possible: Ostwald ripening, coagulation and disintegration of particles [12-24].

There are a number of other factors that can significantly influence the phase transformation phenomenon. In this regard, we can mention the removal of particles of a certain size from the metastable liquid, the admixture influx or the heat sink (crystallisers and crystal granulators) [25-28], simultaneous crystallisation and polymerisation of evolving particles [29, 30], consideration of buoyancy forces [31], electromagnetic forces [32] etc. A number of essential hypotheses are often used to describe the dynamics of individual particles, simplifying mathematical models (e.g., the spherical shape of crystals and the constancy of their growth rates), as well as experimental laws of their evolution [33, 34]. These approaches can give strong deviations with observations at strong supercoolings (supersaturations) of the metastable medium due to significant deviations of the temperature (concentration) field near the crystal from its stationary values. This leads to the necessity to consider non-stationary equations of heat conduction and impurity diffusion in the problem with a free boundary of phase transformation. Note that such a Stefan-type problem does not have exact analytical solution even for a spherical particle shape. This leads to the necessity to construct an approximate non-stationary solution to the growth problem of a single particle. Another key factor strongly influencing the state of metastable liquid is the shape of real crystals, which is far from spherical [35, 36]. One option to take into account the non-spherical shape and construct analytical solutions is to approximate the particle by means of an ellipsoid. In this paper, we consider the influence of such factors as non-stationarity of temperature and impurity concentration distributions around the growing particle, nonsphericity of its shape, curvature of interphase growth boundary and kinetics of atoms sticking to such boundary.

2. Spherical Particles

Let us begin our consideration of the evolution of spherical particles with single- and two-component media. Here we pay our attention to the stationary scenario considering the shift in the crystallization temperature as a result of phase interface curvature, and the kinetics of atoms sticking to the solid-liquid boundary. We then consider the effect of non-stationarity of the temperature and solute concentration distributions during the growth of spherical crystals.

2.1 Stationary Growth

Here we are dealing with the simplest stationary approximation of temperature and solute concentration distributions around the growing spherical particle.

2.1.1 Spherical Particles Evolving in Pure Supercooled Melts

The steady-state evolution of a spherical particle in pure undercooled melt is described by the stationary thermal conductivity equation

$$\frac{\partial^2\theta}{\partial\rho^2}+\frac{2}{\rho}\frac{\partial\theta}{\partial\rho}=0,\ \ \rho>\Sigma(\tau), \tag{1}$$

where θ is the melt temperature, ρ is the spatial coordinate, τ is the time, and Σ is the moving boundary of growing particle, which divides the solid and liquid phases. At this boundary, we have the balance condition of the form

$$\frac{d\Sigma}{d\tau}=-\frac{\lambda_l}{L_V}\frac{\partial\theta}{\partial\rho}=\beta_*(\theta_*-\theta),\ \ \rho=\Sigma(\tau), \tag{2}$$

where λ_l stands for the thermal conductivity of liquid, L_V is the latent heat of crystallization, θ_* is the crystallization temperature of single-component melt, and β_* is the kinetic parameter for thermal problem. Also, we assume that the far-field temperature is fixed

$$\theta\to\theta_l,\ \ \rho\gg\Sigma(\tau). \tag{3}$$

Equation (1) can be easily integrated. By defining integration constants from the boundary conditions (2) and (3), we find the temperature profile $\theta(\rho,\tau)$ in the melt and the growth velocity $d\Sigma/d\tau$ of spherical crystal

$$\theta(\rho,\tau)=\theta_l+\frac{q_\theta\beta_*\Delta\theta\Sigma^2(\tau)}{\big(1+q_\theta\beta_*\Sigma(\tau)\big)\rho},\ \ \rho>\Sigma(\tau), \tag{4}$$

$$\frac{d\Sigma}{d\tau}=\frac{\beta_*\Delta\theta}{1+q_\theta\beta_*\Sigma(\tau)}, \tag{5}$$

where $\Delta\theta=\theta_*-\theta_l$ represents the metastability degree (supercooling), and $q_\theta=L_V/\lambda_l$. If the supercooling does not change, we obtain the solid-liquid boundary of spherical particle in the form

(6) $$\Sigma(\tau)=\frac{1}{q_\theta\beta_*}\left(\sqrt{1+q_\theta\beta_*(2\beta_*\Delta\theta\tau+2\Sigma_0+q_\theta\beta_*\Sigma_0^2)}-1\right),$$

where $\Sigma_0=\Sigma(0)$ is the initial crystal radius.

The radius ρ of spherical crystal can be expressed through its volume v as $\rho(\tau)=(3v(\tau)/4\pi)^{1/3}$. Taking this into account, we find the growth velocity of crystal volume

(7) $$\frac{dv}{d\tau}=4\pi\Sigma^2(\tau)\frac{d\Sigma}{d\tau}=\left(\frac{3v(\tau)}{4\pi}\right)^{2/3}\frac{4\pi\beta_*\Delta\theta}{1+q_\theta\beta_*(3v/4\pi)^{1/3}}.$$

Note that the growth law (5) can be simplified when dealing with small ($\Sigma\ll 1/q_\theta\beta_*$ - kinetic growth) and large ($\Sigma\gg 1/q_\theta\beta_*$ - diffusion growth) particles

(8) $$\frac{d\Sigma}{d\tau}=\beta_*\Delta\theta,\ \ \Sigma\ll 1/q_\theta\beta_*,$$
$$\frac{d\Sigma}{d\tau}=\frac{\Delta\theta}{q_\theta\Sigma(\tau)},\ \ \Sigma\gg 1/q_\theta\beta_*.$$

As a special note, although we use the stationary thermal conductivity equation (1), the temperature distribution in the melt (4) depends on time τ through the moving boundary $\Sigma(\tau)$.

2.1.2 Spherical Particles Evolving in Supersaturated Solutions

In this subsection, we pay our attention to the question of how a spherical particle evolves in a supersaturated solution. The stationary diffusion equation for solute concentration $\sigma(\rho,\tau)$ reads as

(9) $$\frac{\partial^2\sigma}{\partial\rho^2}+\frac{2}{\rho}\frac{\partial\sigma}{\partial\rho}=0,\ \ \rho>\Sigma(\tau).$$

This equation should be supplemented by the mass balance boundary condition

(10) $$(1-k_e)\sigma\frac{d\Sigma}{d\tau}=-D\frac{\partial\sigma}{\partial\rho},\ \ \frac{d\Sigma}{d\tau}=\beta_*\left(\sigma-\sigma_p\right),\ \ \rho=\Sigma(\tau),$$

where k_e and D represent the segregation and diffusion coefficients, and β_* is the kinetic parameter for concentration problem. Also, we assume that the far-field solute concentration is fixed

(11) $$\sigma\to\sigma_l,\ \ \rho\gg\Sigma(\tau).$$

An important point showing the difference between thermal and concentration problems is the difference in the boundary conditions (2) and (10). Indeed, condition (10) contains the nonlinear term $\sigma\, d\Sigma/d\tau$ as compared to linear contributions in expression (2).

Equation (9) implies that $\sigma(\rho,\tau)$ is a linear function of variable ρ. The coefficients of this distribution depend on τ and should be found from two conditions (10) and (11). The third boundary condition (expression (10)) leads us to the quadratic dependence for $d\Sigma/d\tau$. Keeping in mind that the crystal growth rate is sufficiently small in stationary conditions and omitting the quadratic term, we arrive at the following concentration profile in a supersaturated solution and particle growth velocity

(12) $$\sigma(\rho,\tau)=\sigma_l-\frac{q_\sigma\beta_*\Delta\sigma\Sigma^2(\tau)}{\left(1+q_\sigma\beta_*\Sigma(\tau)\right)\rho},\ \ \rho>\Sigma(\tau),$$

(13) $$\frac{d\Sigma}{d\tau}=\frac{\beta_*\Delta\sigma}{1+q_\sigma\beta_*\Sigma(\tau)},$$

where $\Delta\sigma=\sigma_l-\sigma_p$ stands for the system supersaturation (σ_p is the saturation concentration), and $q_\sigma=\sigma_p(k_e-1)/D$. Expression (13) assumes that the particle surface evolves as

(14) $$\Sigma=\frac{1}{q_\sigma\beta_*}\left(\sqrt{1+q_\sigma\beta_*(2\beta_*\Delta\sigma\tau+2\Sigma_0+q_\sigma\beta_*\Sigma_0^2)}-1\right).$$

Taking this into consideration, we obtain the growth velocity of crystal volume

(15) $$\frac{dv}{d\tau}=4\pi\Sigma^2(\tau)\frac{d\Sigma}{d\tau}=\left(\frac{3v(\tau)}{4\pi}\right)^{2/3}\frac{4\pi\beta_*\Delta\sigma}{1+q_\sigma\beta_*(3v/4\pi)^{1/3}}.$$

The growth law (13) can be simplified as before when dealing with small ($\Sigma\ll 1/q_\sigma\beta_*$ - kinetic growth) and large ($\Sigma\gg 1/q_\sigma\beta_*$ - diffusion growth) particles

(16) $$\frac{d\Sigma}{d\tau}=\beta_*\Delta\sigma,\ \ \Sigma\ll 1/q_\sigma\beta_*,$$
$$\frac{d\Sigma}{d\tau}=\frac{\Delta\sigma}{q_\sigma\Sigma(\tau)},\ \ \Sigma\gg 1/q_\sigma\beta_*.$$

2.1.3 Spherical Particles Evolving in Binary Melts

Here we study the steady-state growth law of a single particle in supercooled two-component melt. For such a system, we have the temperature conductivity and diffusion equations (1) and (9). These equations should be supplemented with the boundary conditions at particle's surface

(17) $$\frac{d\Sigma}{d\tau}=-\frac{\lambda_l}{L_V}\frac{\partial\theta}{\partial\rho}=\beta_*\left(\theta_p(\sigma)-\theta\right)=\frac{D}{(k_e-1)\sigma}\frac{\partial\sigma}{\partial\rho},\ \ \rho=\Sigma(\tau),$$

where the crystallization temperature $\theta_p(\sigma)$ is assumed to be a linear function of solute concentration, i.e. $\theta_p(\sigma)=\theta_*-m_e\sigma$ (θ_* is the crystallization temperature of a single-component melt, and m_e is the constant liquidus slope). Substituting the solutions of equations (1) and (9) into the far-field conditions (3) and (11), as well as the heat and mass balances (17), we come to the temperature and concentration profiles and particle's growth velocity

(18) $$\theta(\rho,\tau)=\theta_l-\frac{\theta_1}{\rho},\ \ \sigma(\rho,\tau)=\sigma_l-\frac{\sigma_1}{\rho},\ \ \rho>\Sigma(\tau),$$

(19) $$\frac{d\Sigma}{d\tau}=\beta_*\left(\Delta\theta+\frac{m_e\sigma_1}{\Sigma(\tau)}\left(1-\frac{Dq_\theta}{m_e(k_e-1)(\sigma_l-\sigma_1/\Sigma)}\right)\right)=f(\Sigma),$$

where the time-dependent functions $\theta_1(\Sigma(\tau))$ and $\sigma_1(\Sigma(\tau))$ are given by

$$\theta_1(\Sigma)=\frac{Dq_\theta\sigma_1(\Sigma)}{(k_e-1)(\sigma_l-\sigma_1(\Sigma)/\Sigma(\tau))},$$

$$\sigma_1(\Sigma)=\frac{1}{2}\left(-T(\Sigma)\pm\sqrt{T^2(\Sigma)+4\Delta\theta\Sigma^2(\tau)\sigma_l/m_e}\right),$$

$$T(\Sigma)=\frac{D}{\beta_*(k_e-1)m_e}+\frac{\Delta\theta\Sigma(\tau)}{m_e}-\sigma_l\Sigma(\tau)+\frac{Dq_\theta\Sigma(\tau)}{(k_e-1)m_e},$$

where the supercooling of two-component system reads as $\Delta\theta=\theta_*-m_e\sigma_l-\theta_l$. Expression (19) leads us to the following integral function defining the dependence between particle's radius and time

(20) $$t=\int_{\Sigma(0)}^{\Sigma}\frac{d\Sigma_1}{f(\Sigma_1)}.$$

The growth velocity of crystal volume evolving in a two-component melt is as follows

(21) $$\frac{dv}{d\tau}=4\pi\left(\frac{3v(\tau)}{4\pi}\right)^{2/3}f\left(\left(\frac{3v(\tau)}{4\pi}\right)^{1/3}\right).$$

Let us especially emphasize that particle's growth velocity $d\Sigma/d\tau$ accordingly to expressions (5), (13) and (19) depends on the current radius $\Sigma(\tau)$ while the growth velocity of crystal volume $dv/d\tau$ accordingly to expressions (7), (15) and (21) depends on the current volume $v(\tau)$.

2.2 The Effects of Particle's Curvature and Atomic Kinetics

Dealing with the effects of particle's curvature and atomic kinetics we should modify the crystallization temperature as follows [37-40]

$$\theta_p = \theta_* - \chi/\rho - \mu_k^{-1}\, d\Sigma/d\tau. \tag{22}$$

Here $\chi = \theta_* s/L_V$, s is particle's surface tension, and μ_k stands for the kinetic factor. In this subsection, as before, we omit the temperature and concentration derivatives with respect to time in the thermal conductivity and diffusion equations.

2.2.1 Spherical Particles Evolving in Pure Supercooled Melts

The growth model for a spherical particle reads as

$$\frac{\partial^2\theta}{\partial\rho^2} + \frac{2}{\rho}\frac{\partial\theta}{\partial\rho} = 0, \quad \rho > \Sigma(\tau),$$

$$\frac{d\Sigma}{d\tau} = -\frac{\lambda_l}{L_V}\frac{\partial\theta}{\partial\rho} = \beta_*\left(\theta_* - \frac{\chi}{\rho} - \frac{1}{\mu_k}\frac{d\Sigma}{d\tau} - \theta\right), \quad \rho = \Sigma(\tau), \tag{23}$$

$$\theta \to \theta_l, \quad \rho \gg \Sigma(\tau).$$

Let us omit all mathematical manipulations and represent the solution to this problem as

$$\theta(\rho,\tau) = \theta_l + \frac{q_\theta\tilde{\beta}_*\Sigma^2(\tau)(\Delta\theta - \chi/\rho)}{\left(1 + q_\theta\tilde{\beta}_*\Sigma(\tau)\right)\rho}, \quad \rho > \Sigma(\tau),$$

$$\frac{d\Sigma}{d\tau} = \frac{\tilde{\beta}_*(\Delta\theta - \chi/\rho)}{1 + q_\theta\tilde{\beta}_*\Sigma(\tau)}, \quad \tilde{\beta}_* = \frac{\beta_*}{1 + \beta_*/\mu_k},$$

$$\Delta\theta = \theta_* - \theta_l, \quad q_\theta = \frac{L_V}{\lambda_l}, \tag{24}$$

$$\tau = \frac{q_\theta(\Sigma^2 - \Sigma_*^2)}{2\Delta\theta} + \frac{\chi q_\theta}{\Delta\theta^2}\left(1 + \frac{\Delta\theta}{\chi\tilde{\beta}_* q_\theta}\right)\left(\Sigma - \Sigma_* + \frac{\chi}{\Delta\theta}\ln\left|\frac{\Sigma\Delta\theta - \chi}{\Sigma_*\Delta\theta - \chi}\right|\right), \quad \Sigma_* = \Sigma(0).$$

Expressions (5) and (24) show that the melt supercooling $\Delta\theta$ undergoes the shift χ/ρ while the kinetics of atoms sticking to particle's surface renormalizes the kinetic parameter β_* as $\tilde{\beta}_*$.

Rewriting (24) through the growth velocity of crystal volume, we obtain

$$\frac{dv}{d\tau} = 4\pi\left(\frac{3v(\tau)}{4\pi}\right)^{2/3}\frac{\tilde{\beta}_*\left(\Delta\theta - \chi\left(\frac{4\pi}{3v}\right)^{1/3}\right)}{1 + q_\theta\tilde{\beta}_*\left(\frac{3v}{4\pi}\right)^{1/3}}. \tag{25}$$

2.2.2 Spherical Particles Evolving in Binary Melts

Let us now consider how a spherical crystal evolves in a two-component supercooled melt. The corresponding boundary-value problem reads as

$$\frac{\partial^2\theta}{\partial\rho^2} + \frac{2}{\rho}\frac{\partial\theta}{\partial\rho} = 0, \quad \frac{\partial^2\sigma}{\partial\rho^2} + \frac{2}{\rho}\frac{\partial\sigma}{\partial\rho} = 0, \quad \rho > \Sigma(\tau),$$

$$\frac{d\Sigma}{d\tau} = -\frac{\lambda_l}{L_V}\frac{\partial\theta}{\partial\rho} = \beta_*\left(\theta_* - \frac{\chi}{\rho} - \frac{1}{\mu_k}\frac{d\Sigma}{d\tau} - m_e\sigma - \theta\right) = \frac{D}{(k_e - 1)\sigma}\frac{\partial\sigma}{\partial\rho}, \quad \rho = \Sigma(\tau), \tag{26}$$

$$\theta \to \theta_l, \quad \sigma \to \sigma_l, \quad \rho \gg \Sigma(\tau).$$

The model (26) takes into account the shift of crystallization temperature caused by the phase interface curvature, and the kinetics of atoms sticking to the solid-liquid boundary. The solution to this problem can be written in the form of

$$\theta(\rho,\tau) = \theta_l - \frac{\theta_2(\Sigma)}{\rho}, \quad \sigma(\rho,\tau) = \sigma_l - \frac{\sigma_2(\Sigma)}{\rho}, \quad \rho > \Sigma(\tau),$$

$$\frac{d\Sigma}{d\tau} = \tilde{\beta}_*\left[\Delta\theta - \frac{\chi}{\rho} + \frac{m_e\sigma_2(\Sigma)}{\Sigma(\tau)}\left(1 - \frac{Dq_\theta}{m_e(k_e - 1)(\sigma_l - \sigma_2(\Sigma)/\Sigma)}\right)\right] \equiv g(\Sigma), \quad \tau = \int_{\Sigma(0)}^{\Sigma}\frac{d\Sigma_1}{g(\Sigma_1)}, \tag{27}$$

$$\Delta\theta = \theta_* - \theta_l - m_e\sigma_l,$$

$$\theta_2(\Sigma) = -\frac{Dq_\theta\sigma_2(\Sigma)}{(k_e - 1)(\sigma_l - \sigma_2(\Sigma)/\Sigma(\tau))},$$

$$\sigma_2(\Sigma) = \frac{1}{2}\left(-W(\Sigma) \pm \sqrt{W^2(\Sigma) + 4(\Delta\theta - \chi/\Sigma)\Sigma^2\sigma_l/m_e}\right),$$

$$W(\Sigma) = \frac{D}{\beta_*(k_e - 1)m_e} + \frac{D}{\mu_k(k_e - 1)m_e} - \sigma_l\Sigma(\tau) + \left(\Delta\theta - \frac{\chi}{\Sigma(\tau)}\right)\frac{\Sigma(\tau)}{m_e} + \frac{Dq_\theta\Sigma(\tau)}{(k_e - 1)m_e}.$$

Keeping this in mind, we get the growth velocity of crystal volume

$$\frac{dv}{d\tau} = 4\pi\left(\frac{3v(\tau)}{4\pi}\right)^{2/3} g\left(\left(\frac{3v(\tau)}{4\pi}\right)^{1/3}\right). \tag{28}$$

An important point is that the growth velocity of particle's radius $d\Sigma/d\tau$ given by the laws (24) and (27) is a function of Σ only. In addition, the growth velocity of particle's radius $dv/d\tau$ given by the laws (25) and (28) is a function of v only.

2.3 Nonstationary Growth

The growth of crystal produces the latent heat of solidification in a supercooled melt or displaces the dissolved impurity in a supersaturated solution. These phenomena lead to essential dependence of crystal growth on time. By this is meant that temperature and solute concentration derivatives with respect to time should be taken into account in the thermal conductivity and diffusion equations. Dealing with such time-derivatives, the moving-boundary problem of particle's growth becomes the Stefan-type problem, which does not have an exact analytical solution. To construct an approximate analytical solution to this problem one can use the technique of equivalent spheres [41-43] that surround the evolving crystals. So, let us assume that such a sphere of radius $\Sigma_e \gg \Sigma(\tau)$ surrounds a spherical particle (Fig. 1). To simplify the matter, we neglect the size of nucleated particle ($\Sigma(0) = 0$). Also, we completely neglect the effects of particle's curvature and atomic kinetics. How to include these factors into the analysis developed below is a subject for future research studies.

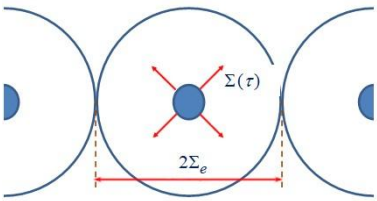

Fig. 1 *A scheme of spherical particles evolution in a metastable liquid.*

2.3.1 Spherical Particles Evolving in Pure Supercooled Melts

The model characterizing the crystal growth process in a supercooled one-component melt reads as

$$\frac{\partial^2\theta}{\partial\rho^2} + \frac{2}{\rho}\frac{\partial\theta}{\partial\rho} = \frac{1}{a}\frac{\partial\theta}{\partial\tau}, \quad \Sigma(\tau) < \rho < \Sigma_e,$$

$$\frac{d\Sigma}{d\tau} = -\frac{\lambda_l}{L_V}\frac{\partial\theta}{\partial\rho} = \beta_*(\theta_* - \theta), \quad \rho = \Sigma(\tau), \tag{29}$$

$$\partial\theta/\partial\rho = 0, \ \ \rho = \Sigma_e,$$

where a represents the temperature diffusivity coefficient. Applying the differential series technique and the Laplace-Carson integral transform method one can find an approximate solution to the problem (29). A detailed description of mathematics is given in Ref. [41]. By restricting ourselves to the first two terms of the asymptotic solution, we obtain

$$\Sigma(\tau) = \beta_*\Delta\theta\left(1 - \frac{\beta_*^2 q_\theta \Delta\theta}{2}\tau\right)\tau,$$
$$\frac{d\Sigma}{d\tau} = \beta_*\Delta\theta(1 - \beta_*^2 q_\theta \Delta\theta\tau), \tag{30}$$

where the melt supercooling is $\Delta\theta = \theta_* - \theta_l$. Here the first term in $d\Sigma/d\tau$ coincides with expression (5) at $\Sigma \ll 1/q_\theta\beta_*$ (kinetic regime of crystal growth). The second term demonstrates the influence of time-derivative $\partial\theta/\partial\tau$ in the thermal conductivity equation. Let us estimate this term as follows $\beta_*^2 q_\theta \Delta\theta\tau \sim 10^{-2}\tau$ s^{-1} (typical estimate for metallic systems). By this is meant that the time-derivative $\partial\theta/\partial\tau$ is substantial at times $\tau \sim 10$ s after the appearance of a nucleated crystal. It means that the growth laws (5) and (8) do not describe the nonstationarity effects in contrast with expressions (30).

It is significant that the growth time τ can be eliminated from expressions (30). In this case, we obtain the following dependence between the growth velocity and particle's radius

$$\frac{d\Sigma}{d\tau} = \beta_*\Delta\theta(1 - 2\beta_* q_\theta \Sigma)^{1/2}. \tag{31}$$

This expression contains the previously found growth velocity (5) at $\Sigma \ll 1/q_\theta\beta_*$:

$$\frac{d\Sigma}{d\tau} = \beta_*\Delta\theta(1 - 2\beta_* q_\theta \Sigma)^{1/2} \approx \beta_*\Delta\theta(1 - \beta_* q_\theta \Sigma)$$
$$\approx \beta_*\Delta\theta(1 + \beta_* q_\theta \Sigma)^{-1} = \frac{\beta_*\Delta\theta}{1 + \beta_* q_\theta \Sigma}. \tag{32}$$

Expression (31) leads us to the growth velocity of crystal volume

$$\frac{dv}{d\tau} = 4\pi\left(\frac{3v(\tau)}{4\pi}\right)^{2/3}\beta_*\Delta\theta\left(1 - 2\beta_* q_\theta\left(\frac{3v(\tau)}{4\pi}\right)^{1/3}\right)^{1/2}. \tag{33}$$

2.3.2 Spherical Particles Evolving in Supersaturated Solutions

The model describing the crystal growth process in a supersaturated solution takes the form

$$\frac{\partial^2\sigma}{\partial\rho^2} + \frac{2}{\rho}\frac{\partial\sigma}{\partial\rho} = \frac{1}{D}\frac{\partial\sigma}{\partial\tau}, \ \ \Sigma(\tau) < \rho < \Sigma_e,$$
$$\frac{d\Sigma}{d\tau} = \beta_*\big(\sigma - \sigma_p\big) = \frac{D}{(k_e - 1)\sigma}\frac{\partial\sigma}{\partial\rho}, \ \ \rho = \Sigma(\tau), \tag{34}$$
$$\partial\sigma/\partial\rho = 0, \ \ \rho = \Sigma_e.$$

The approximate analytical solution to this problem was found in Ref. [42] in the form of

$$\Sigma(\tau) = \beta_*\Delta\sigma\left(1 - \frac{\beta_*^2 q_\sigma \Delta\sigma}{2}\tau\right)\tau,$$
$$\frac{d\Sigma}{d\tau} = \beta_*\Delta\sigma(1 - \beta_*^2 q_\sigma \Delta\sigma\tau), \tag{35}$$

where the supersaturation is $\Delta\sigma = \sigma_l - \sigma_p$. Note that formulas (30) and (35) can be obtained one from the other by substituting $\Delta\theta$ by $\Delta\sigma$ and q_θ by q_σ.

Now let us rewrite (35) in the form of

$$\frac{d\Sigma}{d\tau} = \beta_*\Delta\sigma(1 - 2\beta_* q_\sigma \Sigma)^{1/2}. \tag{36}$$

This expression contains previously derived expression (13) for $\Sigma \ll 1/q_\sigma\beta_*$:

$$\frac{d\Sigma}{d\tau} = \beta_*\Delta\sigma(1 - 2\beta_* q_\sigma \Sigma) = \frac{\beta_*\Delta\sigma}{1 + \beta_* q_\sigma \Sigma}.$$

Expression (36) leads us to the growth velocity of crystal volume

$$\frac{dv}{d\tau} = 4\pi\left(\frac{3v(\tau)}{4\pi}\right)^{2/3}\beta_*\Delta\sigma\left(1 - 2\beta_* q_\sigma\left(\frac{3v(\tau)}{4\pi}\right)^{1/3}\right)^{1/2}. \tag{37}$$

The theory under consideration is compared in Fig. 2 with experiments for potash alum crystal growth [44]. As is easily seen, our formulas well describe experimental points.

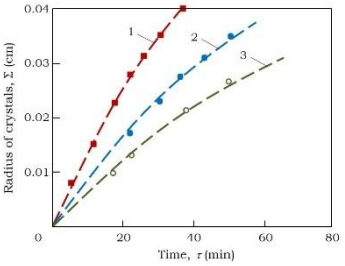

Fig. 2 *Nonstationary behaviour of crystal radius (35) (dashed curves) and experimental data of Ref. [44] (symbols). Physical parameters used in calculations are* $\boldsymbol{\Delta\sigma = 7.7\cdot 10^{-2}}$ *kmol (kg H₂O)⁻¹,* $\boldsymbol{\beta_* = 1.9\cdot 10^{-2}}$ *cm kg H₂O min⁻¹ kmol⁻¹ (1);* $\boldsymbol{\Delta\sigma = 6.2\cdot 10^{-2}}$ *kmol (kg H₂O)⁻¹,* $\boldsymbol{\beta_* = 1.5\cdot 10^{-2}}$ *cm kg H₂O min⁻¹ kmol⁻¹ (2);* $\boldsymbol{\Delta\sigma = 5.4\cdot 10^{-2}}$ *kmol (kg H₂O)⁻¹,* $\boldsymbol{\beta_* = 1.25\cdot 10^{-2}}$ *cm kg H₂O min⁻¹ kmol⁻¹ (3);* $\boldsymbol{\beta_*^2 q_\sigma = 17\cdot 10^{-2}}$ *kg H₂O min⁻¹ kmol⁻¹.*

2.3.3 Spherical Particles Evolving in Binary Melts

Dealing with the nonstationary evolution of a spherical crystal in a supercooled two-component melt, we come to the boundary-value problem

$$\frac{\partial^2\theta}{\partial\rho^2} + \frac{2}{\rho}\frac{\partial\theta}{\partial\rho} = \frac{1}{a}\frac{\partial\theta}{\partial\tau}, \ \ \Sigma(\tau) < \rho < \Sigma_e,$$
$$\frac{\partial^2\sigma}{\partial\rho^2} + \frac{2}{\rho}\frac{\partial\sigma}{\partial\rho} = \frac{1}{D}\frac{\partial\sigma}{\partial\tau}, \ \ \Sigma(\tau) < \rho < \Sigma_e,$$
$$\frac{d\Sigma}{d\tau} = -\frac{\lambda_l}{L_V}\frac{\partial\theta}{\partial\rho} = \beta_*\big(\theta_p(\sigma) - \theta\big), \ \ \rho = \Sigma(\tau), \tag{38}$$
$$\frac{d\Sigma}{d\tau} = \frac{D}{(k_e - 1)\sigma}\frac{\partial\sigma}{\partial\rho}, \ \ \rho = \Sigma(\tau),$$
$$\partial\theta/\partial\rho = 0, \ \ \partial\sigma/\partial\rho = 0, \ \ \rho = \Sigma_e,$$

where the crystallization temperature is given by $\theta_p(\sigma) = \theta_* - m_e\sigma$.

An approximate analytical solution to this problem found in Ref. [43] takes the form

$$\Sigma(\tau) = \beta_*\Delta\theta\left(1 - \frac{\beta_*^2 q_\theta P\Delta\theta}{2}\tau\right)\tau,$$
$$\frac{d\Sigma}{d\tau} = \beta_*\Delta\theta(1 - \beta_*^2 q_\theta P\Delta\theta\tau), \tag{39}$$

where $\Delta\theta = \theta_* - \theta_l - m_e\sigma_l$, and $P = 1 + (1 - k_e)m_e\sigma_l/(q_\theta D)$. Combining expressions (39), we find the growth velocity as a function of $\Delta\theta$ and Σ of the form

$$\frac{d\Sigma}{d\tau} = \beta_*\Delta\theta(1 - 2\beta_* q_\theta P\Sigma)^{1/2}. \tag{40}$$

Note that this growth law transforms to expression (31) if $\sigma_l = 0$ ($P = 1$). Expression (40) for the growth velocity of crystal volume reads as follows

$$\frac{dv}{d\tau} = 4\pi\left(\frac{3v}{4\pi}\right)^{2/3}\beta_*\Delta\theta\left(1 - 2\beta_* q_\theta P\left(\frac{3v}{4\pi}\right)^{1/3}\right)^{1/2}. \quad (41)$$

2.4 Summary Remarks

As a special note, the theory developed in sections 2.1-2.3 considers various aspects of evolution of a spherical crystal in metastable liquids. Unfortunately, it is impossible to combine all of these aspects together and derive a unified growth law even for a spherical particle. This is due to the fact that we are dealing with a Stefan-type moving-boundary problem containing nonlinear boundary conditions. The only way is to generalize the growth laws (5), (24) and (31), leading to the following relationship for the rate of evolution of a spherical particle

$$\frac{d\Sigma}{d\tau} = \tilde{\beta}_*\left(\Delta\theta - \frac{\chi}{\Sigma}\right)\left(1 - 2\tilde{\beta}_* q_\theta \Sigma\right)^{1/2}. \quad (42)$$

When deriving (42), we have used expression (32). Also, it is possible to generalize the growth velocity of crystal volume (expressions (7), (25) and (33)) as

$$\frac{dv}{d\tau} = 4\pi\left(\frac{3v}{4\pi}\right)^{2/3}\tilde{\beta}_*\left(\Delta\theta - \chi\left(\frac{4\pi}{3v}\right)^{1/3}\right) \times\left(1 - 2\tilde{\beta}_* q_\theta\left(\frac{3v}{4\pi}\right)^{1/3}\right)^{1/2}. \quad (43)$$

We compare in Fig. 3 the particle evolution velocity obtained for the stationary and nonstationary thermal conductivity equation, the shift of crystallization temperature caused by the phase interface curvature, the kinetics of atoms sticking to the solid-liquid boundary, and generalized law (42). It is significant to note that all of them are substantially different. This is because each of these growth laws considers only one or a few key physical aspects.

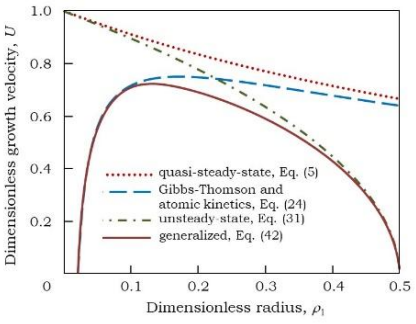

Fig. 3 *The dimensionless rate* $\boldsymbol{U = \tilde{\beta}_*^{-1}\Delta\theta^{-1}d\Sigma/d\tau}$ *of particle growth in a metastable liquid as a function of dimensionless radius* $\boldsymbol{\rho_1 = \tilde{\beta}_* q_\theta \Sigma}$. *The curves are based on the growth velocities (5), (24), (31), and (42). The system parameters for crystal growth in Ti are [39, 45, 46]:* $\boldsymbol{q_\theta = 498\cdot 10^7}$ *K s m*$^{-2}$, $\boldsymbol{\chi = 42\cdot 10^{-7}}$ *m K,* $\boldsymbol{\mu_k = 42\cdot 10^{-2}}$ *m s*$^{-1}$ *K*$^{-1}$, $\boldsymbol{\Delta\theta = 100}$ *K, and* $\boldsymbol{\beta = 10^{-4}}$ *m s*$^{-1}$ *K*$^{-1}$.

3. Ellipsoidal Particles

Let us now turn to the study of the evolution of a system of nonspherical particles in a metastable system. From the mathematical point of view deviations from the spherical form in the first approximation it is convenient to consider by means of ellipsoidal coordinates [47] (Fig. 4). Using this approach we assume that crystals have an ellipsoidal shape during their growth in a liquid.

Let us use here the curvilinear coordinate system of a prolate ellipsoid [47], where particle's surface is defined as $s = s_0 = const$. So, the Cartesian (x, y and z) and ellipsoidal (s, h and ϕ) coordinates are connected as follows

$$x^2 = a^2(s^2-1)(1-h^2)\cos^2\phi\,, \quad y^2 = a^2(s^2-1)(1-h^2)\sin^2\phi\,, \quad z = ash, \quad (44)$$

where a characterizes the dimensions of particles, $s \geq 1$, and $-1 \leq h \leq 1$, $0 \leq \phi \leq 2\pi$.

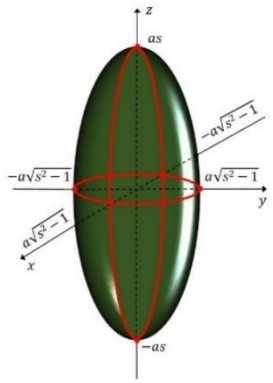

Fig. 4 *A scheme of prolate ellipsoidal particle.*

3.1 Stationary Growth

Let us analyze here how the ellipsoidal crystal grows in a supercooled one-component and binary melt as well as in a supersaturated solution. Hereafter, we will neglect time derivatives of temperature and solute concentration in the thermal conductivity and diffusion equations.

3.1.1 Ellipsoidal Particles Evolving in Pure Supercooled Melts

The ellipsoidal particle growing in a supercooled one-component melt is described by the following heat transfer model

$$\frac{d}{ds}\left((s^2-1)\frac{d\theta}{ds}\right) = 0, \quad s > s_0,$$
$$\dot{s} = -\frac{\lambda_l}{L_V a^2}\frac{\partial\theta}{\partial s} = \frac{\beta_*}{a}(\theta_* - \theta), \quad s = s_0, \quad (45)$$
$$\theta \to \theta_l, \quad s \gg 1.$$

The analytical solution to this model takes the form [48, 49]

$$\theta(s) = \theta_l + \theta_3 \ln\left(\frac{s-1}{s+1}\right), \quad \dot{s}_0 = -\frac{2\varepsilon_1\theta_3}{s_0^2-1},$$
$$\theta_3 = \frac{(\beta_*/a)(\theta_* - \theta_l)}{(\beta_*/a)\ln\left(\frac{s_0-1}{s_0+1}\right) - \frac{2\varepsilon_1}{s_0^2-1}}, \quad \varepsilon_1 = \frac{\lambda_l}{L_V a^2}, \quad (46)$$

where $\Delta\theta = \theta_* - \theta_l$. The solid/liquid surface $s_0 = s_0(v)$ of ellipsoidal particle evolves as

$$s_0^3 - s_0 - \frac{3v}{4\pi a^3} = 0. \quad (47)$$

Applying Cardano's formula for cubic equations to (47), we can find $s_0(v)$. As this takes place, the growth velocity of crystal volume is given by

$$\frac{dv}{d\tau} = \frac{4\pi a^3}{3}[3s_0^2(v) - 1]\dot{s}_0(s_0(v), \Delta\theta). \quad (48)$$

Note that the crystal volume evolves as a function of current particle's volume v and melt supercooling $\Delta\theta$.

3.1.2 Ellipsoidal Particles Evolving in Supersaturated Solutions

Let us now turn to the model of evolution of ellipsoidal particles in a supersaturated solution, which has the form

$$\frac{d}{ds}\left((s^2-1)\frac{d\sigma}{ds}\right)=0,\ \ s>s_0,$$

(49)
$$\dot{s}=-\frac{D}{(1-k_e)a^2\sigma}\frac{\partial\sigma}{\partial s}=\frac{\beta_*}{a}(\sigma-\sigma_p),\ \ s=s_0,$$

$$\sigma\to\sigma_l,\ \ s\gg 1.$$

The analytical solution to this model has the form [49, 50]

(50)
$$\sigma(s)=\sigma_l+\sigma_3\ln\left(\frac{s-1}{s+1}\right),$$
$$\dot{s}_0=\frac{\beta_*}{a}\left[\Delta\sigma+\sigma_3\ln\left(\frac{s_0-1}{s_0+1}\right)\right],$$

where σ_3 should be found from the quadratic equation

$$\ln^2\left(\frac{s_0-1}{s_0+1}\right)\sigma_3^2+b_0\sigma_3+\sigma_l\Delta\sigma=0,$$

$$b_0=(\sigma_l+\Delta\sigma)\ln\left(\frac{s_0-1}{s_0+1}\right)+\frac{2D}{a\beta_*(1-k_e)(s_0^2-1)},$$

and $\Delta\sigma=\sigma_l-\sigma_p$.

Taking this into account, we arrive at the growth velocity of crystal volume in a supersaturated solution

(51)
$$\frac{dv}{d\tau}=\frac{4\pi a^3}{3}[3s_0^2(v)-1]\dot{s}_0(s_0(v),\Delta\sigma).$$

It is significant to note that $s_0(v)$ is defined by expression (47).

3.1.3 Ellipsoidal Particles Evolving in Binary Melts

The boundary-value model that describes the growth of ellipsoidal crystal in a supercooled two-component melt reads as

$$\frac{d}{ds}\left((s^2-1)\frac{d\theta}{ds}\right)=0,\ \ \frac{d}{ds}\left((s^2-1)\frac{d\sigma}{ds}\right)=0,\ \ s>s_0,$$

(52)
$$\dot{s}=-\frac{\lambda_l}{L_V a^2}\frac{\partial\theta}{\partial s}=\frac{\beta_*}{a}(\theta_*-m_e\sigma-\theta),\ \ s=s_0,$$
$$\dot{s}=-\frac{D}{(1-k_e)a^2\sigma}\frac{\partial\sigma}{\partial s},\ \ s=s_0,$$
$$\theta\to\theta_l,\ \ \sigma\to\sigma_l,\ \ s\gg 1,$$

where $\Delta\theta=\theta_*-\theta_l-m_e\sigma_l$. The analytical solution to this model can be written as [50]

$$\theta(s)=\theta_l+\theta_4\ln\left(\frac{s-1}{s+1}\right),\ \ \sigma(s)=\sigma_l+\sigma_4\ln\left(\frac{s-1}{s+1}\right),$$
$$\dot{s}_0=-\frac{2\varepsilon_1\theta_4}{s_0^2-1},$$

(53)
$$\theta_4=\frac{(\beta_*/a)\left(\theta_*-\theta_l-m_e\sigma_l-m_e\sigma_4\ln\left(\frac{s_0-1}{s_0+1}\right)\right)}{(\beta_*/a)\ln\left(\frac{s_0-1}{s_0+1}\right)-\frac{2\varepsilon_1}{s_0^2-1}}$$
$$=\frac{D\sigma_4}{a^2\varepsilon_1(1-k_e)\left[\sigma_l+\sigma_4\ln\left(\frac{s_0-1}{s_0+1}\right)\right]},$$

where σ_4 should be found from the following equation

(54)
$$\alpha\sigma_4^2+\beta\sigma_4+\gamma=0,$$
$$\alpha=\beta_* m_e a\varepsilon_1(1-k_e)\ln^2\left(\frac{s_0-1}{s_0+1}\right),$$
$$\gamma=-\beta_*(\theta_*-\theta_l-m_e\sigma_l)a\varepsilon_1(1-k_e)\sigma_l,$$
$$\beta=\beta_*\ln\left(\frac{s_0-1}{s_0+1}\right)[m_e\sigma_l a\varepsilon_1(1-k_e)$$
$$+\frac{D}{a}-(\theta_*-\theta_l-m_e\sigma_l)a\varepsilon_1(1-k_e)]-\frac{2\varepsilon_1 D}{s_0^2-1}.$$

Keeping this in mind, we find the growth velocity of crystal volume in a supercooled two-component melt

(55)
$$\frac{dv}{d\tau}=\frac{4\pi a^3}{3}[3s_0^2(v)-1]\dot{s}_0(s_0(v),\Delta\theta),$$
$$\Delta\theta=\theta_*-\theta_l-m_e\sigma_l.$$

Note that $s_0(v)$ and $\dot{s}_0=\dot{s}_0(s_0(v),\Delta\theta)$ in (55) are respectively defined by expressions (47) and (53), (54).

3.2 Evolution of Not Heavily Stretched Ellipsoids ($s_0\gg 1$)

Here we consider small deviations from spherical shape of particles if $s_0\gg 1$ (Fig. 5).

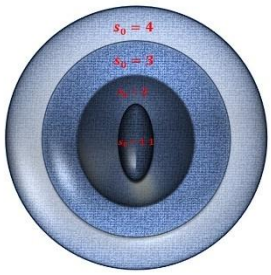

Fig. 5 *A scheme of ellipsoidal crystal for various* $\boldsymbol{s_0}$.

3.2.1 Ellipsoidal Particles Evolving in Pure Supercooled Melts

So, considering not heavily stretched ellipsoidal particles ($s_0-1\approx s_0$ and $s_0+1\approx s_0$), we obtain ($\Delta\theta=\theta_*-\theta_l$)

(56)
$$s_0\approx\left(\frac{3v}{4\pi}\right)^{1/3}\frac{1}{a},\ \ \theta_3\approx-\frac{\beta_* s_0^2\Delta\theta}{2a\varepsilon_1},$$
$$\dot{s}_0=\frac{\beta_*\Delta\theta}{a},\ \ \frac{dv}{d\tau}=4\pi\left(\frac{3v}{4\pi}\right)^{2/3}\beta_*\Delta\theta.$$

This expression gives the same growth velocity of crystal volume as expression (8) in the case of kinetic mode approximation.

Let us now expand the natural logarithm at $s_0\gg 1$ as follows

(57)
$$\ln\left(\frac{s_0-1}{s_0+1}\right)=\ln\left(1-\frac{2}{s_0+1}\right)\approx-\frac{2}{s_0+1}-\frac{2}{(s_0+1)^2}.$$

Now combining (46)-(48) and (57) at $s_0\gg 1$, we get

(58)
$$s_0\approx\left(\frac{3v}{4\pi}\right)^{1/3}\frac{1}{a},\ \ \theta_3\approx-\frac{\beta_* s_0^2\Delta\theta q_\theta a}{2(1+\beta_* s_0 q_\theta a)},$$
$$\dot{s}_0=\frac{\beta_*\Delta\theta}{a\left(1+\beta_* q_\theta\left(\frac{3v}{4\pi}\right)^{1/3}\right)},$$
$$\frac{dv}{d\tau}=4\pi\left(\frac{3v}{4\pi}\right)^{2/3}\frac{\beta_*\Delta\theta}{1+\beta_* q_\theta\left(\frac{3v}{4\pi}\right)^{1/3}}.$$

Note that $dv/d\tau$ from (7) and (56) are identical.

3.2.2 Ellipsoidal Particles Evolving in Supersaturated Solutions

Let us now expand $\ln[(s_0-1)/(s_0+1)]\approx 0$ at $s_0\gg 1$. Taking this into account, we obtain the following formulas from expressions (50) and (51)

$$s_0 \approx \left(\frac{3v}{4\pi}\right)^{1/3}\frac{1}{a},\quad \sigma_3 \approx -\frac{\sigma_l \Delta\sigma}{b_0},$$

$$b_0 \approx \frac{2D}{a\beta_*(1-k_e)s_0^2},\qquad \dot{s}_0 = \frac{\beta_*\Delta\sigma}{a}, \tag{59}$$

$$\frac{dv}{d\tau} = 4\pi\left(\frac{3v}{4\pi}\right)^{2/3}\beta_*\Delta\sigma.$$

Note that expressions (16) and (59) are identical for the kinetic scenario of crystal growth.

3.2.3 Ellipsoidal Particles Evolving in Binary Melts

Now we rewrite formulas (53) and (55) with allowance for $s_0 - 1 \approx s_0$ and $s_0 + 1 \approx s_0$ ($\Delta\theta = \theta_* - \theta_l - m_e\sigma_l$) in the form of

$$s_0 \approx \left(\frac{3v}{4\pi}\right)^{1/3}\frac{1}{a},\quad \theta_4 \approx -\frac{\beta_* s_0^2 \Delta\theta}{2a\varepsilon_1},$$

$$\dot{s}_0 = \frac{\beta_*\Delta\theta}{a},\quad \frac{dv}{d\tau} = 4\pi\left(\frac{3v}{4\pi}\right)^{2/3}\beta_*\Delta\theta. \tag{60}$$

It is significant to note that expressions (56) and (60) valid for one-component and two-components melts are identical for $s_0 \gg 1$. They differ only in the supercooling $\Delta\theta$.

3.3 Summary Remarks

Expressions (56) and (58) derived for $s_0 \gg 1$ and formulas (7), (25), (33) and (43) derived for spherical particles enable us to introduce a unified formula for the growth velocity of crystal volume

$$\frac{dv}{d\tau} = 4\pi\left(\frac{3v(\tau)}{4\pi}\right)^{2/3}\tilde{\beta}_*\left(\Delta\theta - \chi\left(\frac{4\pi}{3v(\tau)}\right)^{1/3}\right) \times\left(1 - 2\tilde{\beta}_* q_\theta\left(\frac{3v(\tau)}{4\pi}\right)^{1/3}\right)^{1/2}, \tag{61}$$

where the melt supercooling for a one-component system is given by $\Delta\theta = \theta_* - \theta_l$. The generalized evolutionary law (61) comprises the shift of crystallization temperature caused by the phase interface curvature, the kinetics of atoms sticking to the solid-liquid boundary, and nonstationary temperature field around the growing particle. The value of the generalized law (61) consists also in the fact that it can be used both for spherical and ellipsoidal particles. The unified law (61) can also be used for supersaturated solutions. In this case, $\Delta\theta = \theta_* - \theta_l$ and q_θ in (61) should be replaced by $\Delta\sigma = \sigma_l - \sigma_p$ and q_σ for supersaturated solutions and $\Delta\theta = \theta_* - \theta_l - m_e\sigma_l$ and $q_\theta P$ for supercooled two-component melts.

Now we compare the theory under question with experiments. For this purpose, we introduce the total mass of particles $M = \rho_s N v$, where ρ_s is the density of solid material, N is the total number of particles, and v is the volume of single particle. Keeping this in mind we come to the growth velocity of particles $dM/d\tau = \rho_s N dv/d\tau$, where $dv/d\tau$ should be substituted from the generalized law (61). Next introducing $R_g = [4\pi(3v/(4\pi))^{2/3}N\ ]^{-1}$, one can get

$$R_g = \tilde{\gamma}_*\left(\Delta\theta - \chi\left(\frac{4\pi}{3v}\right)^{1/3}\right)\left(1 - 2\tilde{\beta}_* q_\theta\left(\frac{3v}{4\pi}\right)^{1/3}\right)^{1/2}, \tag{62}$$

where $\tilde{\gamma}_* = \rho_s\tilde{\beta}_*$.

In Figs. 6 and 7, we present the theory under consideration and experiments of Ref. [51] (here we have used the desupersaturation curve given in Ref. [51]). Also, to use expression (62) for a supersaturated solution, we changed $\Delta\theta$ and q_θ by $\Delta\sigma$ and q_σ.

In Fig. 8, we compare expression (62) with experiments [52] for citric acid monohydrate crystal growth in a liquid fluidized bed (R_g, $\Delta\sigma$ and average size of crystals are from Fig. 2 and table 1 in Ref. [52].)

From the good agreement between theory and experiments in Figs. 6, 7 and 8 one can conclude that generalized laws of particle volume growth (61) and (62) describe laboratory data quite well.

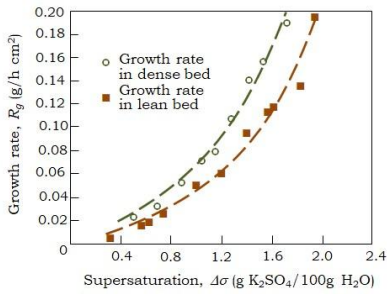

Fig. 6 *The generalized growth law (62) is compared with experiments [51] (symbols) for potassium sulfate crystals evolving in a fluidized bed crystallizer. Physical parameters are* $\boldsymbol{\chi_\sigma = \beta_*^2 q_\sigma = 5\cdot 10^{-2}}$ *h⁻¹* $\boldsymbol{[\Delta\sigma]^{-1}}$, $\boldsymbol{\gamma = \rho_s\beta_* = 1.15\cdot 10^{-1}}$ *g h⁻¹ cm⁻²* $\boldsymbol{[\Delta\sigma]^{-1}}$*(dense bed), and* $\boldsymbol{\chi_\sigma = 5.5\cdot 10^{-2}}$ *h⁻¹* $\boldsymbol{[\Delta\sigma]^{-1}}$, $\boldsymbol{\gamma = 8\cdot 10^{-2}}$ *g h⁻¹ cm⁻²* $\boldsymbol{[\Delta\sigma]^{-1}}$*(lean bed);* $\boldsymbol{\chi = 0}$, $\boldsymbol{\mu_k = 0}$.

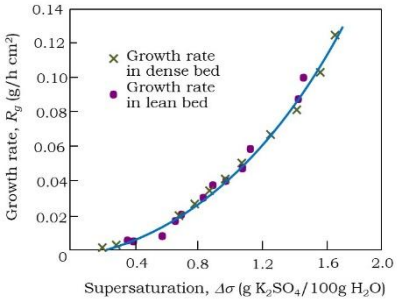

Fig. 7 *The generalized growth law (62) is compared with experiments [51] (symbols) for potassium sulfate crystals evolving in a fluidized bed crystallizer. Physical parameters are* $\boldsymbol{\chi_\sigma = 4.9\cdot 10^{-2}}$ *h⁻¹* $\boldsymbol{[\Delta\sigma]^{-1}}$, $\boldsymbol{\gamma = 8.2\cdot 10^{-2}}$ *g h⁻¹ cm⁻²* $\boldsymbol{[\Delta\sigma]^{-1}}$*(dense and lean beds);* $\boldsymbol{\chi = 0}$, $\boldsymbol{\mu_k = 0}$.

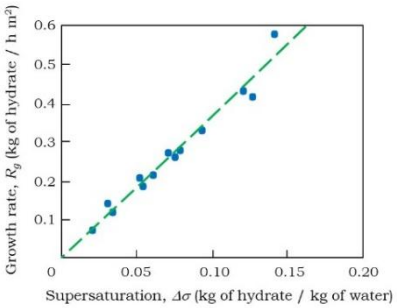

Fig. 8 *The generalized growth law (62) is compared with experiments [52] (symbols) for citric acid monohydrate crystals evolving in a liquid fluidized bed. Physical parameters are* $\boldsymbol{\kappa = \beta_* q_\sigma = 180}$ *m⁻¹,* $\boldsymbol{\gamma = 6}$ *kg of water h⁻¹ m⁻².*

4. Conclusion

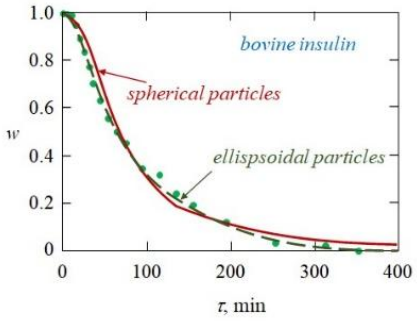

Fig. 9 *Dimensionless supersaturation* $\boldsymbol{w = \Delta\sigma/\Delta\sigma_0}$ *versus time* $\boldsymbol{\tau}$ *for bovine insulin accordingly to the present theory and experiments [73, 74].*

In conclusion, let us compare the growth theory of spherical and ellipsoidal crystals with experimental data [73, 74] for bovine insulin. Fig. 9 illustrates the dynamics of dimensionless supersaturation $w = \Delta\sigma/\Delta\sigma_0$ ($\Delta\sigma_0$ is the initial supersaturation). As is easily seen, the ellipsoidal shape of crystals better describes the supersaturation removal than the spherical shape. The theory under consideration can be used to describe different cases of the evolution of particulate assemblages in metastable media (see, among others, Ref. [75]).

This work was supported by the Russian Science Foundation (Grant no. 18-19-00008).

5. References

1. A.C. Zettlemoyer, *Nucleation* (Dekker, New York, 1969)
2. J.W. Mullin, *Crystallization* (Butterworth, London, 1972)
3. S. Martin, P. Kauffman, J. Fluid Mech. **64**, 507 (1974)
4. Y.A. Buyevich, D.V. Alexandrov, IOP Conf. Ser.: Mater. Sci. Eng. **192**, 012001 (2017)
5. D.V. Alexandrov, A.P. Malygin, J. Phys. A: Math. Theor. **46**, 455101 (2013)
6. D.V. Alexandrov, P.K. Galenko, Philos. Trans. R. Soc. A **378**, 20190243 (2020)
7. D.V. Alexandrov, I.G. Nizovtseva, Proc. R. Soc. A **470**, 20130647 (2014)
8. Yu.A. Buyevich, V.V. Mansurov, J. Cryst. Growth **104**, 861 (1990)
9. D.V. Alexandrov, A.P. Malygin, Modelling Simul. Mater. Sci. Eng. **22**, 015003 (2014)
10. D.V. Alexandrov, Phys. Lett. A **378**, 1501 (2014)
11. D.A. Barlow, J. Cryst. Growth **470**, 8 (2017)
12. I.M. Lifshitz, V.V. Slyozov, J. Phys. Chem. Solids **19**, 35 (1961)
13. E.M. Lifshitz, L.P. Pitaevskii, *Physical kinetics* (Pergamon, Oxford, 1981)
14. J.R. Hunt, J. Fluid Mech. **122**, 169 (1982)
15. D.V. Alexandrov, Commun. Theor. Phys. **68**, 269 (2017)
16. Y. Enomoto, A. Okada, J. Phys.: Condens. Matter. **2**, 4531 (1990)
17. A.V. Alyab'eva, Yu.A. Buyevich, V.V. Mansurov, J. Phys. II (France) **4**, 951 (1994)
18. S. Simons, J. Phys. A: Math. Gen. **29**, 1139 (1996)
19. D.V. Alexandrov, J. Phys. Chem. Solids **91**, 48 (2016)
20. D.V. Alexandrov, I.V. Alexandrova, Philos. Trans. R. Soc. A **378**, 20190247 (2020)
21. D.V. Alexandrov, Phil. Mag. Lett. **96**, 355 (2016)
22. D.V. Alexandrov, J. Phys.: Condens. Matter **28**, 035102 (2016)
23. D.V. Alexandrov, J. Mater. Science **52**, 6987 (2017)
24. D.V. Alexandrov, J. Cryst. Growth **457**, 11 (2017)
25. Yu.A. Buyevich, V.V. Mansurov, I.A. Natalukha, Chem. Eng. Sci. **46**, 2573 (1991)
26. D.V. Alexandrov, Chem. Eng. Sci. **117**, 156 (2014)
27. E.V. Makoveeva, D.V. Alexandrov, Philos. Trans. R. Soc. A **376**, 20170327 (2018)
28. E.V. Makoveeva, D.V. Alexandrov, Philos. Trans. R. Soc. A **377**, 20180210 (2019)
29. Yu.A. Buyevich, I.A. Natalukha, Chem. Eng. Sci. **49**, 3241 (1994)
30. A.A. Ivanov, I.V. Alexandrova, D.V. Alexandrov, Philos. Trans. R. Soc. A **377**, 20180215 (2019)
31. D.V. Alexandrov, Phil. Mag. Lett. **96**, 132 (2016)
32. A.O. Ivanov, A.Yu. Zubarev, Physica A **251**, 348 (1998)
33. R.F. Strickland-Constable, *Kinetics and mechanisms of crystallization* (Academic Press, London, 1968)
34. P. Bennema, Theory and experiment for crystal growth from solutions: Implications for industrial crystallization, in *Industrial Crystallization*, edited by J.W. Mullin (Springer, Boston, MA, 1976)
35. M. Ocaña, M.P. Morales, C.J. Serna, J. Colloid Int. Sci. **171**, 85 (1995)
36. T. Sugimoto, A. Muramatsu, J. Colloid Int. Sci. **184**, 626 (1996)
37. W. Kurz, D.J. Fisher, *Fundamentals of solidification* (Trans. Tech. Publ., Aedermannsdorf, 1989)
38. D. Herlach, P. Galenko, D. Holland-Moritz, *Metastable solids from undercooled melts* (Elsevier, Amsterdam, 2007)
39. E.V. Makoveeva, D.V. Alexandrov, Phys. Lett. A **384**, 126259 (2020)
40. E.V. Makoveeva, D.V. Alexandrov, Eur. Phys. J. Special Topics **229**, 2923 (2020)
41. D.V. Alexandrov, J. Phys. A: Math. Theor. **51**, 075102 (2018)
42. D.V. Alexandrov, I.G. Nizovtseva, I.V. Alexandrova, Int. J. Heat Mass Trans. **128**, 46 (2019)
43. D.V. Alexandrov, I.V. Alexandrova, Philos. Trans. R. Soc. A **377**, 20180209 (2019)
44. K. Toyokura, K. Yamazoe, J. Mogi, N. Yago, Y. Aoyama, Secondary nucleation of potash alum, in *Industrial Crystallization*, edited by J.W. Mullin (Springer, Boston, MA, 1976)
45. P.K. Galenko, K. Reuther, O.V. Kazak, D.V. Alexandrov, M. Rettenmayr, Appl. Phys. Lett. **111**, 031602 (2017)
46. I.V. Alexandrova, D.V. Alexandrov, Philos. Trans. R. Soc. A **378**, 20190245 (2020)
47. G.A. Korn, T.M. Korn, *Mathematical handbook for scientists and engineers: definitions, theorems, and formulas for reference and review* (McGraw-Hill Book Company, New York, 1968)
48. M.A. Nikishina, D.V. Alexandrov, Eur. Phys. J. Special Topics **229**, 2937 (2020)
49. M.A. Nikishina, D.V. Alexandrov, Math. Meth. Appl. Sci. **44**, 12252 (2021)
50. M.A. Nikishina, D.V. Alexandrov, Eur. Phys. J. Special Topics **231**, 1107 (2022)
51. J. Garside, C. Gaska, J.W. Mullin, J. Cryst. Growth **13/14**, 510 (1972)
52. C. Laguerie, H. Angelino, Growth rate of citric acid monohydrate crystals in a liquid fluidized bed, in *Industrial Crystallization*, edited by J.W. Mullin (Springer, Boston, MA, 1976)
53. D.V. Alexandrov, J. Phys. A: Math. Theor. **48**, 245101 (2015)
54. D.V. Alexandrov, A.A. Ivanov, I.V. Alexandrova, Philos. Trans. R. Soc. A **376**, 20170217 (2018)
55. D.V. Alexandrov, A.Y. Zubarev, Philos. Trans. R. Soc. A **377**, 20180353 (2019)
56. D.V. Alexandrov, A.A. Ivanov, I.V. Alexandrova, J. Phys. A: Math. Theor. **52**, 015101 (2019)
57. D.V. Alexandrov, A.Y. Zubarev, Philos. Trans. R. Soc. A **378**, 20200002 (2020)
58. D.V. Alexandrov, Eur. Phys. J. Special Topics **229**, 383 (2020)
59. D.V. Alexandrov, Acta Mater. **49**, 759 (2001)
60. D.V. Alexandrov, A.P. Malygin, I.V. Alexandrova, Ann. Glaciol. **44**, 118 (2006)
61. D.L. Aseev, D.V. Alexandrov, Int. J. Heat Mass Trans. **49**, 4903 (2006)
62. D.V. Alexandrov, I.G. Nizovtseva, Int. J. Heat Mass Trans. **51**, 5204 (2008)

63. P.K. Galenko, D.V. Alexandrov, Philos. Trans. R. Soc. A **376**, 20170210 (2018)
64. P.K. Galenko, D.V. Alexandrov, E.A. Titova, Philos. Trans. R. Soc. A **376**, 20170218 (2018)
65. D.V. Alexandrov, I.A. Bashkirtseva, L.B. Ryashko, Philos. Trans. R. Soc. A **376**, 20170216 (2018)
66. I.G. Nizovtseva, D.V. Alexandrov, Philos. Trans. R. Soc. A **378**, 20190248 (2020)
67. G.P. Yasnikov, J. Eng. Phys. **42**, 163 (1982)
68. Yu.A. Buyevich, Yu.M. Goldobin, G.P. Yasnikov, Int. J. Heat Mass Trans. **37**, 3003 (1994)
69. Yu.A. Buyevich, N.A. Korolyova, I.A. Natalukha, Int. J. Heat Mass Trans. **36**, 2223 (1993)
70. Yu.A. Buyevich, N.A. Korolyova, I.A. Natalukha, Int. J. Heat Mass Trans. **36**, 2233 (1993)
71. K. Masters, *Spray drying in practice* (Spray Dry Consult, Charlottenlund, Denmark, 2002)
72. A.A. Ivanov, D.V. Alexandrov, I.V. Alexandrova, Philos. Trans. R. Soc. A **378**, 20190246 (2020)
73. J. Schlichtkrull, Acta Chem. Scand. **11**, 439 (1957)
74. J. Schlichtkrull, Acta Chem. Scand. **11**, 1248 (1957)
75. D.V. Alexandrov, A.A. Ivanov, I.G. Nizovtseva, S. Lippmann, I.V. Alexandrova, E.V. Makoveeva, Crystals **12**, 949 (2022)

Pressure-induced long-time phase transitions in selected choosen vegetable oils

Leszek T. Pawlicki
Warsaw University of Technology Faculty of Physics
Koszykowa 75 00-662 Warszawa

Abstract: *Research on vegetable oils was already carried out in the industrial era. Oils are used not only in the food industry, but also in the cosmetics and pharmaceutical industries. Due to the beneficial effect on the human body, they have been studied more and more thoroughly. The development of high pressure food preservation has further accelerated this process. Due to the use of pressure in the production and preservation of food, it turned out to be important to study the phase transitions induced by pressure in these oils. Due to their long-term nature, these transformations may damage the machines used in the industry. So far well-researched vegetable oils in this regard are castor oil, rapeseed oil, soybean oil, sunflower oil and olive oil. Research on other oils will be conducted in the future.*

Introduction

Vegetable oils are one of the substances produced by man for the longest time. In antiquity, they were produced, among others, in China, India, Egypt, Greece and Rome. Even then, their beneficial influence on human health was known. They were an ingredient of many dishes, they were used as a natural medicine and used for body care. The health-promoting effect of vegetable oils on the human body is also widely discussed today [1-4].

Of great importance for example olive oil, the myth of the protection of Athens may prove. The scene depicting this mythical event was presented, among others in the center of the west tympanum of the Parthenon (temple dedicated to the goddess Athena) located on the Acropolis in Athens [5].

The ancient Egyptians also used oils in many ways for example, as a "sunscreen" to protect against sunburn.

Oils were extruded originally using cloth bags, to which sticks were attached and the whole thing was tightly twisted until the juice ran out. Olives placed on canvas, in a stone hole, with wooden hamers, were also churned. The juice, on the other hand, was collected under the cloth. It was also possible to put olives in a cloth, tied bag and tread them [6]. Later, much more productive methods of obtaining oils appeared. Heavy stone rollers were rolled over the seeds or olives. Then, millstones were used to obtain oils [6]. Eventually, presses began to be used for the production of oil. These were lever and screw presses and wedge-shaped and finally hydraulic. With the advent of the industrial revolution, these presses began to be driven mechanically, thermodynamically and eventually electrically. The industrial production of oils resulted in lower prices and greater availability.

All this made people more interested in oils. Their physical, chemical and medical properties began to be explored. It turned out that they can be used not only in the food industry, but also in the cosmetics and pharmaceutical industries.

Research on oils

Vegetable oils were very valuable and very unstable at the same time. They broke quickly. Research has shown that not only microbes and pollution, but also the access of air or sunlight have a negative impact on their condition. For this reason, good quality oils were sealed in dark glass bottles. Research has also begun on how to get rid of microorganisms from oils without depriving them of such valuable nutrients. The use of ultraviolet and then X-rays caused the breakdown of many molecular bonds and impoverished the composition of the oil. The oil was heated as well. Cold-pressed oil is of a higher quality than hot-pressed oil for a reason [7-9]. Additionally, these two pasteurization methods resulted in the formation of new, often poisonous substances in the oil. So other methods of preservation were sought. Ultimately, due to the fact that the oils were produced using pressure, it was decided to check whether this preservation could not be obtained with the high-pressure method. It turned out that this method is not only effective in killing microorganisms, but also (if properly carried out) allows to preserve the nutrients of oils and at the same time does not create new hazardous substances. This resulted in the rapid development of high-pressure food preservation methods, which continues to this day [10-18].

Research on vegetable oils has been conducted at the Warsaw University of Technology since 1975. They were initially devoted to the selection of fluids for piston high pressure standards. Since the rheological parameters of the working fluid constitute a significant part of the formula defining the effective piston cross-section of such a standard, the tests of compressibility and viscosity of castor oil, commonly recommended for this application, were started. These were the classic measurements of density and viscosity carried out in the range up to approx. 0.3 GPa. Initially, these studies did not show any phase transitions. Phase transitions for vegetable oils were observed for the first time in castor oil in 1989 [19].

Phase transitions caused by temperature changes in oils have been known for a long time [20-24], while such a pressure-induced transformation has not been observed before.

Initially, attempts were made to explain the observed transformation with the properties of fatty acids whose acid residues constituted the triglyceride chains of castor oil. For this reason, studies of pressure changes in oleic, linoleic and other acids have been carried out [25-30].

Monoglycerides [31] and diglycerides of fatty acids [32-36] have also been studied.

Initially, the influence of pressure was limited to the study of PVT (pressure-volume-temperature) characteristics [37-38]. Significant progress was later made [39-40] by optical observation of pressure-induced crystallization of triglycerides. The properties of edible oils were also tested in high-pressure laboratories. These experiments were a continuation of previous studies on changes in pressure physical properties of castor oil [41]. Measurements of optical properties of triglycerides [42] showed the occurrence of the first kind of phase transitions. The phenomenon of pressure-induced phase transformation has been studied by many methods, showing discontinuous changes in volume [43], refractive index [42], dielectric permittivity [44] and viscosity [45-48] during the phase transition. Most of these effects are summarized in [41]. Further progress was achieved thanks to the study of pressure changes in the triolein [38, 47, 49-53]. These studies showed similar phase changes as in castor oil. Both of these substances are mixtures of fatty acid triglycerides. On this basis, the occurrence of a phase change was predicted in a wide class of edible oils with the above properties [54-60]. These predictions were confirmed by observations of phase transformations in rapeseed oil [54-55]. Moreover, the measurements of the dependence V(p) (volume from pressure) and ε (p) (relative permittivity from pressure) were performed for soybean oil [56], showing similar behavior. All these transformations taking place in oils showed a long-time character (these transformations lasted much longer than for standard substances - even several days). In the meantime, physical research on the quality of oils (including olive oil) began [61, 62]. Therefore, sunflower oil and olive oil were selected for further high-pressure tests carried out by me. As part of these tests, measurements of mechanical properties were made, which confirmed the occurrence of long-time phase transitions in these oils. Electrical quantities were tested for the same oils (in terms of composition) [63-67]. The previously used method of testing phase transitions in vegetable oils based on the measurement of electric permittivity has been developed much more precisely. The physical causes of changes in the values of electric parameters of oils were established. The

change in the value of electric permittivity was related both to the concentration of molecules, their shape and their mutual position [68]. Resistivity was used for the first time to study phase transitions. Changes in its value have been carefully analyzed and related to changes in the arrangement, shape, size and decay rate of ion channels. Also for the first time to analyze phase changes in vegetable oils, electrical phase diagrams were used along with impedance changes contained in them. These charts are arranged in characteristic shapes resembling triangles. All these electrical methods (based on the measurement of permittivity, resistivity as well as with the use of impedance phase diagrams) showed high sensitivity to physical processes occurring during phase transitions. They also turned out to be resistant to external factors (except the pressure chamber). These methods also turned out to be one of the easiest to use. Providing clear and distinct results, unlike, for example, temperature measurements. This is due to the long-time phase transformations taking place in oils [54-60, 63-67].

Summary and conclusions

Vegetable oils have been produced since ancient times and were valued in many ancient countries [5]. Today they are also valued for their pro-health properties [1-4]. Vegetable oils have always been pressed from seeds or fruit, and the methods of pressing them have evolved over time [6]. At one point, the oils were investigated and it was discovered that the rate of their deterioration was influenced not only by microorganisms but also by light and air. Therefore, appropriate maintenance methods were applied. Some of them based on heating and radiation have turned out to be harmful. For this reason, a method of pressure oil preservation has been developed, which allows to preserve their nutritional value [10-18]. Pressurized extracting and preservation of oils contributed to the acceleration of research on pressure-induced phase transitions in vegetable oils.

So far, the components of vegetable oils, including fatty acids [25-31], diglycerides [32-36], and triglycerides [38-41, 47-52], have been well researched in terms of pressure-induced phase changes. Some oils have also been well researched in this respect, including: castor [19, 42-46], rapeseed [54-55], soybean [56], sunflower [57, 66-67] and olive oil [58-65]. The remaining oils are still not well researched in this regard and will likely be tested in the future.

These studies were carried out using, inter alia, thermodynamic [31, 37, 43, 63, 66], ultrasonic [32, 34, 35, 48, 59], resonance [64], optical [36, 42, 58, 61, 62], x-ray [25] and electric [29, 30, 44, 65, 67] methods.

Due to the long-time nature of phase transformations occurring in vegetable oils, a rapid change in the physical properties of the oil during them and the use of pressure for their extracting and preservation, the constant expansion of knowledge about these changes is crucial for the safe operation of machines, both in the food, cosmetic and pharmaceutical industries.

References

[1] R.W. Owen, A. Giacosa, W.E. Hull, R. Haubner, G. W¨urtele, B. Spiegelhalder, and H. Bartsch. Olive-oil consumption and health: The Possible Role of Antioxidants. Lancet Oncology, 1(2):107–112, (2000).

[2] D. Boskou, M. L. Clodoveo, Olive Oil: Processing Characterization, and Health Benefits, Foods 9(11) 1612, (2020).

[3] A. Foscolou, E. Critselis, S. Tyrovolas, Ch. Chrysohoou, L. S. Sidossis, N. Naumovski, A. L. Matalas, L. Rallidis, E. Polychronopoulos, J. L. Ayuso-Mateos, J. M. Haro and D. Panagiotakos, The Effect of Exclusive Olive Oil Consumption on Successful Aging: A Combined Analysis of the ATTICA and MEDIS Epidemiological Studies, Foods 8(1), 25 (2019).

[4] E. M. Yubero-Serrano, J. Lopez-Moreno, F. Gomez-Delgado, J. Lopez-Miranda, Extra Virgin Olive Oil: More Than a Healthy Fat, Europian Journal of Clinical Nutrition 72, 8-17 (2019).

[5] M. Beard, Partenon, Dom Wydawniczy Rebis, Poznań (2018)

[6] T. Lofthouse, G. Lofthouse, Oliwa, Różne Rodzaje Oliwy I Jej Zastosowania, Wydawnictwo Liber K. E., Warszawa (2008).

[7] B. C. Roy, M. Sasaki, M. Goto, Effect of Temperature and Pressure on the Extraction Yield of Oil from Sunflower Seed with Supercritical Carbon Dioxide, Journal of Applied Sciences 6(1) (2006).

[8] A. Pietsch, R. Eggers, Gas-assisted Oilseed Pressing - Design of and Tests with a Novel High-pressure Screw Press, Procedia Food Science 1 1381-1387 (2011).

[9] B. S. Adesina, Y. O. Bankole, Effects of Particle Size, Applied Pressure and Pressing Time on the Yield of Oil Expressed from Almond Seed, Nigerian Food Journal v. 31 issue 2, p. 98-105 (2013).

[10] D. Knorr, Effects of High-hydrostatic-pressure Processes on Food Safety and Quality, Food Technology, 47 (6), 156-161 (1993).

[11] J. A. Torres and G. Velásquez, Commercial Opportunities and Research Challenges in the High Pressure Processing of Foods, Journal of Food Engineering 67 (2005), pp. 95-112.

[12] T. Norton, Da-Wen Sun, Recent Advances in the Use of High Pressure as an Effective Processing Technique in the Food Industry. Food Bioprocess Technology, 2008, 1, 2-34.

[13] C. Tonello, Case Studies on High-pressure Processing of Foods, Nonthermal Processing Technologies for Food.. Wiley-Blackwell, Oxford . 2010, pp. 36-50.

[14] S. Jung, C. Tonello-Samson, High Hydrostatic Pressure Food Processing: Potential and limitations, Alternatives to Conventional Food Processing, Ed. A. Proctor. RSC Publishing, London 2011, pp. 254-305.

[15] V. M. Balasubramaniam, G. V. Barbosa-Canovas, H. Lelieveld, High Pressure Processing of Food, Principles, Technology and Applications, Springer, New York (2016).

[16] M. Zulkurnain, F. Maleky, V. M. Balasubramaniam, High Pressure Processing Effects on Lipids, Thermophysical Properties and Crystallization Kinetics, Food Engineering Reviews (2016) p. 1-21.

[17] J. Szczepańska, S. Skąpska, J. M. Lorenzo & K. Marszałek, The Influence of Static and Multi-Pulsed Pressure Processing on the Enzymatic and Physico-Chemical Quality, and Antioxidant Potential of Carrot Juice During Refrigerated Storage, Food and Bioprocess Technology 14, 52-64 (2021).

[18] K. Marszałek, Ł. Woźniak, S. Skąpska, & M. Mitek, High Pressure Processing and Thermal Pasteurization of Strawberry Purée: Quality Parameters and Shelf Life Evaluation During Cold Storage, Journal of Food Science and Technology 54, 832-841 (2017).

[19] R. M. Siegoczyński, J. Jędrzejewski and R. Wiśniewski, Long Time Relaxation Effect of Liquid Castor Oil Under High Pressure Condition, High Pressure Research. 1, 225 – 301 (1989).

[20] R. H. Ferguson and E. S. Lutton, The Polymorphism of Triolein, Journal of the American Chemical Society 69(6), pp. 1445–1448 (1947).

[21] Ch. Akita, T. Kawaguchi and F. Kaneko, Structural Study on Polymorphism of Cis-Unsaturated Triacylglycerol: Triolein, The Journal of Physical Chemistry B 110 p. 4346-4353 (2006).

[22] F. F. Hollander, S. X. M. Boerrigter, J. van de Streek, P. Bennema, H. Meekes, J. Yano and K. Sato, Comparing the Morphology of β-n.n.n. with β'-n.n+2.n and β'-n.n.n-2 Triacylglycerol Crystals, The Journal of Physical Chemistry B 107 p. 5680-5689 (2003).

[23] K. Sato, Solidification and Phase Transformation Behaviour of Food Fats – a review, Fett/Lipid 101(12), pp. 467–474 (1999).

[24] K. Sato, Crystallization Behaviour of Fats and Lipids – a review, Chemical Engineering Science 56 p. 2255-2265 (2001).

[25] J. Przedmojski, R. M. Siegoczyński, X-ray Diffraction Investigation of Oleic Acid Under High Pressure, Phase Transitions 75 p. A p. 581-585 (2002).

[26] R. Kościesza, L. Kulisiewicz, and A. Delgado. Observations of a High-pressure Phase Creation in Oleic Acid. High Pressure Research, 30(1):118–123, (2010).

[27] K. Wieja, R. Tarakowski, R. M. Siegoczyński, and A. J. Rostocki. Pressure-induced Changes in Electronic Absorption Spectrum in Oleic Acid. High Pressure Research, 30(1):130–134, (2010).

[28] K. Wieja, R. Tarakowski, R. M. Siegoczyński, and A.J. Rostocki. Investigation of Rhodamine 6g in Oleic Acid Solution Fluorescence Under High Pressure. High Pressure Research, 31(1):158–162, (2011).

[29] R. Kościesza and R. M. Siegoczyński, Influence of High Pressure on the Relative Permittivity of Oleic Acid. High Pressure Research, 31(1):237–242, (2011).

[30] R. Kościesza, R.M. Siegoczyński, A.J. Rostocki, D.B. Tefelski, A. Kos, and W. Ejchart. Relative Permittivity Behavior and Temperature Changes in Linoleic Acid During the Phase Transition, Journal of Physics: Conference Series, 121(PART 14), (2008).

[31] V. Romain, A. Ch. Ngakegni-Limbili, Z. Mouloungui, J. Ouamba, Thermal Properties of Monoglycerydes from Nephelium Lappaceum L. Oil, as a Natural Source of Saturated and Monounsaturated Fatty Acids, Industrial & Engineering Chemistry Research 52, 39, 14089-14098 (2013)
[32] A. J. Rostocki, A. Malanowski, R. Tarakowski, K. Szlachta, P. Kiełczyński,
M. Szalewski, A. Balcerzak and S. Ptasznik, The Sound Velocity Measurement in Diacylglycerol Oil Under High Pressure, High Pressure Research 33 p. 172-177, (2013).
[33] A. Malanowski, A. J. Rostocki, P. Kiełczyński, M. Szalewski, A. Balcerzak, R. Kościesza, R. Tarakowski, S. Ptasznik and R. M. Siegoczyński, Viscosity and Compressibility of Diacylglycerol Under High Pressure, High Pressure Research 33 p. 178-183 (2013).
[34] P. Kiełczyński, M. Szalewski, A. Balcerzak, A. Malanowski, R. M. Siegoczyński, S. Ptasznik, Investigation of High-pressure Phase Transitions in DAG (Diacylglycerol) Oil Using the Bleustein-Gulyaev Ultrasonic Wave Method, Food Research International 49 p. 60-64 (2012).
[35] P. Kiełczyński, M. Szalewski, A. Balcerzak, K. Wieja, A. Malanowski, R. Kościesza, R. Tarakowski, A. J. Rostocki, and R. M. Siegoczyński. Determination of Physicochemical Properties of Diacylglycerol oil at High Pressure by Means of Ultrasonic Methods, Ultrasonics, 54(8):2134–2140, (2014).
[36] R. Kościesza, D.B. Tefelski, S. Ptasznik, A.J. Rostocki, A. Malanowski, and R.M. Siegoczyński. A study of the high pressure phase transition of diacylglycerol oil by means of light transmission and scattering. High Pressure Research, 32(2):323–329, (2012).
[37] A. J. Rostocki, D. B. Tefelski , S. Ptasznik, Compressibility Studies of Some Vegetable Oils up to 1 GPa, High Pressure Research, Volume 29, Issue 4, Pages 721-725 (2009).
[38] A. J. Rostocki, D. B. Tefelski and K. Wieja, The Equation of State of Triolein up to 1 GPa, High Pressure Research 31 p. 168-171 (2011).
[39] P. Ferstl, S. Gillig, C. Kaufmann, C. Dürr, C. Eder, A. Wierschem, and W. Ruß, Pressure Induced Phase Transitions in Triacylglycerids, Annals of the New York Academy of Science 1189, pp. 62–67 (2010).
[40] P. Ferstl, C. Eder, W. Ruß and A. Wierschem Pressure-induced Crystallization of Triacylglycerides, High Pressure Research Vol. 31, No. 2, 339–349 (2011).
[41] R. M. Siegoczyński Reports of Institute of Physics, Publishing House of the Warsaw University of Technology, Warsaw (1998).
[42] R. M. Siegoczyński, J. Jędrzejewski, R. Wiśniewski; The Influence of Pressure on the Refractive Index of Castor Oil up to 0.8 GPa., High Pressure Research, 8, 439-441 (1991).
[43] R. Wiśniewski, J. Jędrzejewski, R. M. Siegoczyński, A. Tkacz, Volume Changes of Castor Oil During its Transformation to the High Pressure Phase, High Pressure Research, 11, 385 –391 (1994).
[44] R. Wiśniewski, J. Jędrzejewski, R. M. Siegoczyński, Dielectric Permittivity and Dielectric Loss of Castor Oil During its Transformation to the High Pressure Phase, High Pressure Research., 13, 41 – 45 (1994).
[45] R. Wiśniewski, R. M. Siegoczyński, A. J. Rostocki, Viscosity Measurement of Some Castor Oil Based Mixtures Under High Pressure Conditions , High Pressure Research, 25, 63-70, (2005).
[46] R.M. Siegoczyński, R. Wiśniewski, and W. Ejchart. On the Structure of a Pressure-induced New Phase in Castor Oil. Journal of Molecular Liquids, 107(1-3):257–261, (2003).
[47] R. M Siegoczyński, A.J. Rostocki, P Kiełczyński and M. Szalewski, A Viscosity Measurement During the High Pressure Phase Transition in Triolein, Journal of Physics: Conference Series 121 142010 (2008).
[48] A. J. Rostocki, R. M. Siegoczyński, P. Kieczyński, M. Szalewski, An Application of Love SH Waves for the Viscosity Measurement of Triglycerides at High Pressures, High Pressure Research, Volume 30, Issue 1, Pages 88-92 (2010).
[49] D. B. Tefelski, C. Jastrzębski, M. Wierzbicki, R. M. Siegoczyński, A. J. Rostocki, K. Wieja & R. Kościesza, Raman Spectroscopy of Triolein Under High Pressures, High Pressure Research v. 30, p. 124-129 (2010).
[50] A. Kos, D. B. Tefelski, R. Kościesza, A. J. Rostocki, A. Roszkiewicz, W. Ejchart, C. Jastrzębski and R. M. Siegoczyński, Certain Physico-chemical Properties of Triolein and Methyl Alcohol-triolein Mixture Under Pressure, High Pressure Research 27 p. 39-42 (2007).
[51] D. B. Tefelski, A. J. Rostocki, A. Kos, R. Kościesza and R. M. Siegoczyński, Pressure Induced Volume Changes in Triolein with Addition of Methyl Alcohol, High Pressure Research 27 p. 57-61 (2007).
[52] R. Wiśniewski, R.M. Siegoczyński, A. Długosz, M. Przewłocki, M. Szymański, and M. Trzeciecki. Investigations of Triolein Under High Pressure. High Temperatures - High Pressures, 33(2):231–236, (2001).
[53] A. Roßbach, L. A. Bahr, S. Gäbel1, Andreas S. Braeuer, A. Wierschem, Growth Rate of Pressure-induced Triolein Crystals, Journal of the American Oil Chemists' Society, v. 96 pp. 25-33 (2019).
[54] A. J. Rostocki, R. Wiśniewski, T. Wilczyńska, High Pressure Phase Transition in Rape-seed Oil, Journal of Molecular Liquids 135 (2007) p. 120-122.
[55] R. Kościesza, A. J. Rostocki, A. Kos, D. B. Tefelski, R. M. Siegoczyński and Ł. Zych, Observation of Pressure-induced Phase Transitions in Rapeseed Oil with Methyl Alcohol Mixtures, High Pressure Research 27 (2007) p. 51-55.
[56] A. J. Rostocki, R. Kościesza, D. B. Tefelski, A. Kos, R. M. Siegoczyński and Ł. Chruściński, Pressure-induced Phase Transition in Soy Oil, High Pressure Research 27 (2007) p. 43-46.
[57] Á. Guinda, M. C Dobarganes, M. V. Ruiz-Mendez, M. Mancha, Chemical and Physical Properties of a Sunflower Oil with High Levels of Oleic and Palmitic Acids, European Journal Lipid Science Technology 105, 130–137, (2003).
[58] R. Tarakowski, A. Malanowski, R. Kościesza, R. M. Siegoczyński, VIS Spectroscopy and Pressure Induced Phase Transitions – Chasing the Olive Oils Quality, Journal of Food Engineering 122 (2014) p. 28-32.
[59] A. J. Rostocki, R. Tarakowski, P. Kiełczyński, M. Szalewski, A. Balcerzak, S. Ptasznik, The Ultrasonic Investigation of Phase Transition in Olive of Oil up to 0.7 GPa, Journal of the American Oil Chemists Society 90 (2013) p. 813-818.
[60] B. Guignon, C. Aparicio and P. D. Sanz, Volumetric Properties of Sunflower and Olive Oils at Temperatures Between 15 and 55 ˚ C Under Pressures up to 350 MPa, High Pressure Research 29 (2009) p. 38-45.
[61] A. G. Mignani, L. Ciaccheri, H. Ottevaere, H. Thienpont,l. Conte, M. Marega, A. Cichelli, C. Attilio, A. Cimato, Visible and Near-infrared Spectral Signatures for Adulteration Assessment of Extra Virgin Olive Oil, Optical Sensing and Detection v. 7726 (2010)
[62] A. G. Mignani, L. Ciaccheri, A. A. Mencaglia, R. Paolesse, C Di Natale, A. Del Nobile, R. Benedetto, A. Mentana, Quality Monitoring of Extra-virgin Olive Oil Using an Optical Sensor, Optical Sensing II v. 6189 (2006).
[63] L. T. Pawlicki, R. M. Siegoczyński, S. Ptasznik, K. Marszałek, Compressibility Studies of Olive Oil, Journal of Biotechnology and Biomedicine 4, 187-195 (2021).
[64] L. T. Pawlicki, M. K. Urbański, D. Tefelski, R. M. Siegoczyński, Viscosity Measurement of Olive Oil Under Pressure, Food Science & Nutrition Technology 6 issue 5 (2021).
[65] L. T. Pawlicki, R. M. Siegoczyński, S. Ptasznik, K. Marszałek, Electric Properties of Olive Oil Under Pressure, European Food Research and Technology, 247(8), 1933-1937 (2021).
[66] L. T. Pawlicki, A. J. Rostocki, D. B. Tefelski, R. M. Siegoczyński and S. Ptasznik, Mechanical Properties of Sunflower Oil Under Pressure, European Food Research and Technology 248 p. 283-287 , (2022).
[67] L. T. Pawlicki, A. J. Rostocki, D. B. Tefelski, R. M. Siegoczyński and S. Ptasznik, Electric Properties of Sunflower Oil Under Pressure, International Journal of Scientific Engineering and Applied Science v. 8, issue, 214-227 (2022).
[68] A. L. McClellan, Tables of Experimental Dipole Moments, W. H. Freeman, San Francisco, CA, 1963.

Electronic properties of carbon nanostructures

Halyna Yu. Mykhailova, Mykola Ya. Shevchenko
G. V. Kurdyumov Institute for Metal Physics of the N.A.S. of Ukraine
36 Academician Vernadsky Boulevard, UA-03142 Kyiv, Ukraine
E-mail: mihajlova.halina@gmail.com

Abstract: *The properties of an array of carbon nanostructures or a material containing its is differ from the properties of individual components. For bulk array of carbon nanostructures it is unknown to what extent the electrons of each layer participate in conductivity, the role of defects is not defined. properties. So, this work presents some answers to these questions.*
Key words: *carbon nanotubes, electrical properties, composite, mechanical properties*

Introduction

The needs of resources for various industries are growing, this causes resource, technological, environmental and social problems. The exhaustion of fossil fuel and energy sources stimulates the development of methods of using alternative and ecologically safe energy sources, which contributes to their widespread implementation.

Today the shortage of energy resources is partially covered by the use of direct conversion of thermal and radiant energy into electrical energy using photothermoelectric converters (solar cells). But there are a number of limitations here: this type of energy production occupies large areas for its stations. In addition, this type of energy production is conditionally ecological: the production of solar panels and their disposal greatly pollutes the environment.

Carbon nanostructures have a unique anisotropic structure that determines their electronic properties [1-5], a special place is occupied by carbon nanotubes (CNTs), its can be sources of intense self-electron emission [6]. This feature of them, the inertialessness of electron moving along the CNT axis and the tunneling mechanism of their exit, does not require large energy costs. Such materials are of great interest in the field of energy storage and conversion due to their unique properties [7]. It is necessary to descry between the electrical conductivity of individual particles of carbon nanostructures and the conductivity of a composite or material containing such structures.

Today, using of carbon nanomaterials in the energy industry contributes to the improvement of already existing elements and contributed to the development of thermocouples for energy storage systems [8], the main problem of alternative energy sources is that they do not adapt to the demand of energy problems, so the urgent issue is not only in the search for new materials that will expand the possibilities of their application, and it is necessary to simultaneously develop elements for storing this energy. And carbon nanomaterials open up opportunities to solve these problems in both directions [9-13].

Carbon nanomaterials have shown high efficiency when used in solar batteries [14], which confirms the uniqueness of such structures.

Authors of the work [14] showed the possibilities of using carbon nanomaterials in thermoelectric elements. Such materials can serve as thermoelectric generators, and composites based on them increase their characteristics even more.

Defects in CNTs can occur during synthesis (growth defects) or during external exposure, for example, high-energy irradiation.

Experimentally obtained CNTs may contain defects that lead to distortion of their structure and differences in properties. The formation of bent, column-shaped, serpentine CNTs, as well as tubes of variable diameter occurs only in the presence of topological defects, which are associated with rehybridization and unsaturated bonds [15]. The presence of defects will contribute to the expansion of the spheres of application of carbon nanostructures.

Therefore, the search and research of new materials with increased functional properties for the needs of alternative energy is one of the priority directions for solving the above-mentioned problems. A special place is occupied by carbon-containing materials promising for use in storage devices and direct energy converters.

Experiment

The electrical conductivity of the array of carbon nanotubes was measured in a dielectric cylinder. The latter was filled with nanotubes that were compressed when the piston was lowered. The bottom of the cylinder and the piston were made of copper and served as electrodes. After reaching the maximum compression to a density of ~1.5 g/cm^3, the piston was gradually raised. At the same time, the electrical contact between the nanotubes and the electrodes was maintained, which is due to the elastic relaxation of the previously compressed array of carbon nanotubes. This allowed measuring electrical conductivity during discharge. The termination of the elastic relaxation of nanotubes led to the opening of electrical contacts and a sharp increase in electrical resistance, which was determined by the dependence of electrical conductivity on the density of the material $\sigma(\rho)$.

Multilayer nanotubes in diameter were obtained by chemical vapor deposition (CDV).

Results

Multilayered carbon nanotubes (MCNTs) differ from single-layered ones in a wider variety of shapes and configurations. Most often, these are coaxially nested single-layer nanotubes. Of course, the situation for an array of individual nanotubes or a material consisting of them may be different due to the presence of contacts between adjacent nanotubes, electrodes, contact pressure and other factors. When changing the volume in which an array of electrically conductive CNTs is placed above a certain critical value, the closure of nanotubes may occur with the manifestation of characteristic signs of the percolation transition. The latter, as is known, is a geometric analogue of the metal-insulator transition [16].

The electrical conductivity of multilayer (fig. 1*a*) and single-layer (fig. 1*b*) carbon nanotubes was studied. In accordance with the basic assumption of transmission electron microscopy that the contrast intensity of images directly depends on the amount of scattering substance, so darker areas in positive images correspond to thicker areas of the sample or heavier atoms present in the sample, the observed narrow dark bands refer to the walls of the nanotube.

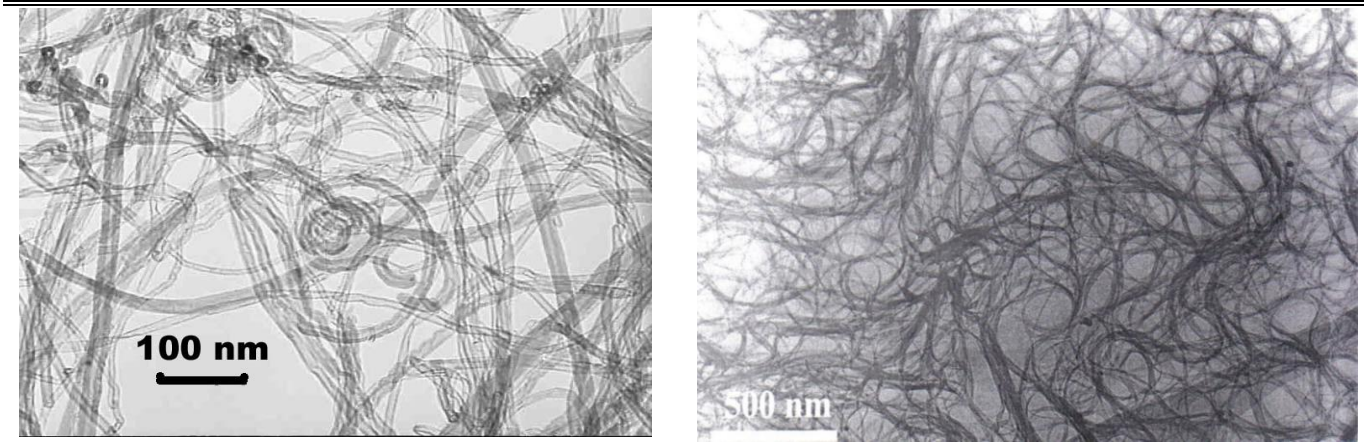

a) *b)*

Fig. 1 *– TEM image of multilayer (a) and single-layer (b) carbon nanotubes*

The statistical distribution of MCNT by outer diameter showed that the diameter of its is in the range of 7-25 nm. Most tubes have a diameter of 9-15 nm. The thickness of the CNT walls varies between 3 and 4 nm. Nanotubes have 5-17 carbon layers, with the most likely value of 9 carbon layers (fig. 1a).

Single-layer CNTs were obtained by electric arc evaporation on a Ni/Y catalyst (fig. 1 *b*). Cleaning was carried out by oxidation in air and washed in HCl solution, without the use of surface-active substances. The specific gravity of CNT is 93-94%. The main impurities are graphite particles with a size of 2-4 μm and impurities of metals Ni, Y, Cu, Zn ($\sum$ = 1.3%). The specific surface area is 375 m^2/g, the proportion of open nanotubes is 24%.

When the volume in which the interacting nanotubes are placed decreases, the electrical circuit closes and the system (nanotube-air) goes into a conductive state, which corresponds to the dielectric-metal transition.

Fig. 2 shows the dependence of the electrical conductivity of an array of arbitrarily oriented CNTs on its density. At the initial stage of compression, the regrouping of nanotubes occurs, the density of their packing increases, which leads to the closing of the electrodes and the appearance of electrical conductivity in the region of the percolation transition. It can be seen that the initial density of the array of interacting CNTs, which is sufficient for measuring electrical conductivity and at which the transition to the conductive state occurs, is 0.13 g/cm^3.

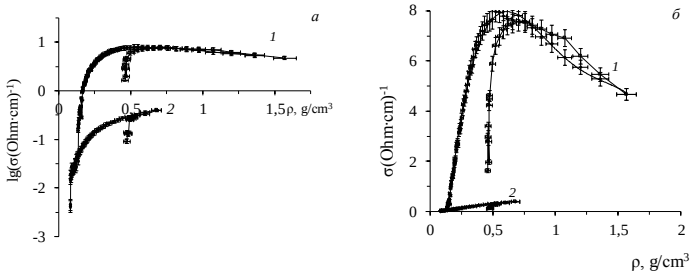

Fig. 2 *– Dependence of the electrical conductivity of an array of single-layer and multilayer CNTs in the process of compression deformation. a – along of the ordinate axis is lgσ, b – the real value of σ. 1 – SCNT, 2 – MCNT, ♦ - loading, □ - unloading*

During the compression under the piston, the electrical conductivity jumps up by 3 orders of magnitude, reaching a maximum value of 8.0 $(\Omega \cdot cm)^{-1}$ at a density of 0.5 g/cm^3. Subsequent compression to a density of 1.6 g/cm^3 leads to a decrease in electrical conductivity to 4 $(Ohm \cdot cm)^{-1}$. Deformation leads to the appearance of mechanical stresses, which contribute to the appearance of additional potentials, at which conduction electrons are scattered during the passage of current. This causes a drop in electrical conductivity.

The observed effects (fig. 2) are explained by the action of two competing mechanisms: 1) an increase in the total contact area between neighboring CNTs, which contributes to the growth of electrical conductivity; 2) elastic deformation, which contributes to a decrease in electrical conductivity.

After compressing the sample to ρ≈1.6 g/cm^3, the piston was raised and simultaneously measured the electrical conductivity of the elastically relaxing material, which is restored to the maximum value and ensures contact with the electrodes. The reverse course of the curve σ(ρ) in the process of elastic relaxation of the CNT repeats the course of the curve during compression on a large segment of the piston path. Completion of the relaxation process was recorded by a sharp increase in electrical resistance σ(ρ) and opening of the electrical circuit. This process was fixed by the density of the relaxation transition. The appearance of hysteresis between the transition to the conducting state and the relaxation transition is caused by inelastic processes that are associated with the displacement of nanotubes during deformation.

The electrical conductivity of SCNTs was 1.5 orders of magnitude lower than that of MWNTs (fig. 2). The density of the transition to the conducting state decreases to 0.08 g/cm^3, but they have a much lower elastic limit (30%).

This difference in electrical conductivity is due to the different type of conductivity in CNTs.

c

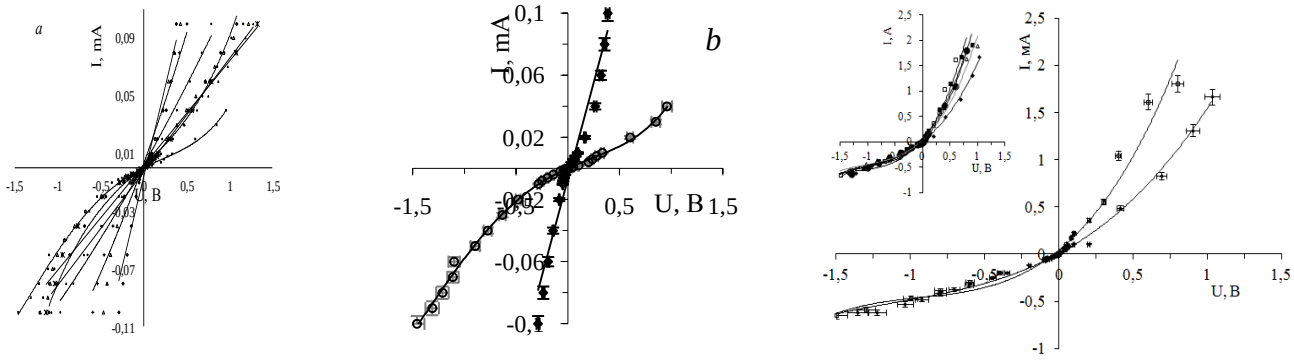

Fig. 3 *– VCC of MCNT for different compression densities of the array. a – range of densities ρ=0.13-0.51 g/cm^3, b – at minimum and maximum compression density. ▲ – ρ=0.13 g/cm^3, ■ – ρ=0.136 g/cm^3, Δ – ρ=0.147 g/cm^3, ○ – ρ=0.15 g/cm^3, g – ρ=0.152 g/cm^3, ● – ρ=0.155 g/cm^3, ◊ – ρ=0.18 g/cm^3,+ – ρ=0.26 g/cm^3, Δ – ρ=0.35 g/cm^3, ♦ – ρ=0.51 g/ cm^3; c - SCNT: a - current-voltage characteristics for different compression densities of the CNT array ♦ - ρ=0.51 g/cm^3, Δ - ρ=0.60 g/cm^3, ■ - ρ=0.68 g/cm^3, ● - ρ=0.78 g/ cm^3,□ - ρ=0.92 g/cm^3*

The study of the current-current characteristics (VCC) for different compression densities of the CNT array showed that the VCC of the bulk MCNT array during the compression process was not always linear in nature: at a density of up to ρ=0.35 g/cm^3, the VCC has a nonlinear symmetrical appearance, which indicates van der Waals interaction in the array of CNTs at a certain density (fig. 3 *a*). With the subsequent increase in density and maximum compression, the I-V characteristic is linear (fig. 3, b). This behavior of the VCC confirms the close relationship between the electrical properties of CNTs and the mechanical load.

SCNT have an asymmetric VCC for all compression densities in the range of ρ=0.51-0.92 g/cm^3 (Fig. 3*c*), which indicates the semiconducting nature of the conductivity.

Conclusions

In the process of deformation of an array of unoriented MWNTs, the electrical conductivity jumps up by 3 orders of magnitude, reaches a maximum (8 (Ω·cm)$^{-1}$ at a density of ρ=0.5 g/cm^3) and decreases by a factor of two upon further compression. The observed effects are explained by the action of two competing mechanisms: 1) an increase in the total area of van der Waals contacts between the outer shells of neighboring CNTs, which leads to an increase in electrical conductivity; 2) elastic deformation of CNTs, which leads to a decrease in electrical conductivity.

References

1. Yao Zh., Postma H. W. Ch., Balents L., Dekker C., Imaging and Characterization of Molecules and One- Dimensional Crystals Formed within Carbon Nanotubes *Nature*, V. 402. 1999.P. 273.
2. Curran S. A., Talla J., Dias S., Zhang D.,Carroll D. Electrical transport measurements of highly conductive carbon nanotube / poly (bisphenol A carbonate) composite *J. Appl. Phys.*V. 105. 2009. P. 073711.
3. Ahmad K., Pan W., Shi S. L. Electrical conductivity and dielectric properties of multiwalled carbon nanotube and alumina composites *Appl. Phys. Lett.*V. 89. 2006.P. 133122.
4. Sandler J. K. W., Kirk J. E., Kinloch I. A., Shaffer M. S. P., Windle A. H. Ultra-low electrical percolation threshold in carbon-nanotube-epoxy composites *Polymer*.V. 44. 2003. P. 5893.
5. Bryning M. B., Islam M. F., Kikkawa J. M., Yodh A. G. Very Low Conductivity Threshold in Bulk Isotropic Single - Walled Carbon Nanotube – Epoxy Composites *Adv. Mater.*V. 17. 2005. P. 1186.
6. Kymakis E., Alexandou I., Amaratunga G. A. Electrical Properties of Soluble Carbon Nanotube / Polymer Composite Films *Synthetic Metals*.V. 127. 2002. P. 59.
7. Sundaram R. M., Sekiguchi A., Sekiya M., Yamada T., Hata K. *R. Copper / carbon nanotube composites: research trends and outlook Soc. Open Sci.*V. 5.Iss. 11. 2018. P. 180814.
8. Collins P. G. Extreme oxygen sensitivity of electronic properties of carbon nanotubes *Science*.V. 287. 2000. P. 1801.
9. Li Guo- ran, Wang Feng, Jiang Qi- wei, Gao Xue- ping, Shen Pan- wen. Carbon Dioxide Capture by Superbase-Derived Protic Ionic Liquids *Carbon, Advantante Chemie*.V. 49. 2010.P. 3653.
10. Nishchenko M.M., Mykhailova H.Yu., Arkhipov E.I., Koda V.Yu., Prikhodko G.P., Sementsov Yu.I. Electrical conductivity of an array of multilayer carbon nanotubes during compression deformation Metallofizika i Noveishie Tekhnologii. T. 31. № 4. 2009.P. 437.
11. Mikhailova G.Yu., Nishchenko M.M., Pimenov V.N.,Starostin E.E., Tovtin V.I. Thermoelectric and Elastic Properties of Carbon Nanotubes Irradiated with High-Energy Electrons *Inorganic Mater.: Appl. Res.*V. 10.No. 5. 2019.P. 1052.
12. Nishchenko M.M., Mikhailova G.Yu., Kovalchuk B.V., Sidorchenko I.M., Anikeev V.V., Shevchenko N.A., Poroshin V.M., Prikhodko G.P. Thermoelectric Properties of an Array of Carbon Nanotubes under Uniaxial Compression after Annealing Metallofizika i Noveishie Tekhnologii. T. 40. № 2. 2018.P. 169.
13. Zhang S., Ji Ch., Bian Zh., Liu R., Xia X., Yun D., Zhang L., Huang Ch., Cao A. Single-wire dye-sensitized solar cells wrapped by carbon nanotube film electrodes *NanoLett.* V. 11. (2011).P. 3383.
14. Mavrinsky A.V., Andriychuk V.P., Baitinger E.M. Thermoelectromotive force of powdered tubulens // News of the Chelyabinsk Scientific Center. - 2002. - No. 3. - P. 16-20.
15. Harris P. Uglerodnye nanotrubki i rodstvennye struktury. Novye materialy HHI Veka / P. Harris. – M.:Tehnosfer, 2003. – 335 p.
16. SHevchenko V.G. Osnovy fiziki polimernyh kompozicionnyh materialov / V.G. SHevchenko. – M.: MGU, 2010, 256 p.

The effects of graphite additive on hydrogen sorption/desorption behavior by the Mg/C composite

Inna Kirian, Andrey Lakhnik, Alexander Rud
G.V. Kurdyumov Institute for Metal Physics N.A.S. of Ukraine, Kyiv, Ukraine
kiryan.inna@gmail.com

Absract: *The reactive ball milling technique was applied to fabricate the Mg-based composite with graphite additives. The sorption/desorption kinetics of the composites were investigated under isothermal conditions. The best hydrogen sorption/desorption kinetics was attained for the magnesium-carbon composite synthesized using the low surface area graphite powder as an active additive. This sample is characterised by the best kinetics performance compared to other composites. It releases 4.2 wt.% of hydrogen at 270 ºC within ~18 min and uptakes 4.6 wt/.% of hydrogen for ~130 min at 200 ºC.*

Keywords*: HYDROGEN STORAGE, Mg, GRAPHITE ADDITIVE, SORPTION/DESORPTION*

1. Introduction

The most ecologically clean source of energy is hydrogen. Its combustion in the heated element leads only to the formation of water, which prevents pollution of the environment by combustion products. However, several drawbacks prevent the widespread use of hydrogen. One of these obstacles is the development of efficient and safe hydrogen storage systems, which is associated with its low density (gaseous state ~0.09 kg/m^3), low liquefaction temperature, and high explosiveness [1]. The requirements of the US Department of Energy (DOE) are guided during the development of promising hydrogen storage systems [2]. There are several ways of storing and transporting hydrogen [3, 4], namely in:

- a gaseous state under pressure (high pressure cylinders);
- a liquid state in cryogenic containers;
- the solid-phase bound state in metal hydrides;
- an adsorbed state on cryoadsorbents at low temperatures;
- a chemically bound state in liquid media;
- combined systems.

However, none of the above hydrogen storage methods meets the requirements of the Department of Energy. Developing a safe, efficient, and cost-effective way to store hydrogen is an important task.

The metal/intermetallic hydrides are the most suitable and promising method to store and transport hydrogen in large amounts. Some of these compounds have fast hydrogen uptake/desorption kinetics at near-ambient temperatures, a simple activation process, and moderate hydrogenation pressure. However, most of them have a low hydrogen capacity [5-8].

One of the most promising candidates for long-term hydrogen storage and transport is magnesium due to its high theoretical reversible hydrogen storage capacity (7.6 wt. %) and low cost [9]. Moreover, magnesium is widely distributed in nature, non-toxic and safe to use when preventing its oxidation. The equilibrium modification of MgH_2 is a tetragonal α-MgH_2 phase. Under the high pressure impact, α-MgH_2 undergoes polymorphic transformations with the formation of two modifications: γ-MgH_2 and β-MgH_2, which have a rhombic structure and a hexagonal structure, respectively [10]. However, some drawbacks limit the practical use of MgH_2 as a hydrogen storage medium. These include high values of operating temperatures ~300 ºC, slow sorption/desorption kinetics, difficulty of activation, and deterioration of properties during cycling [11]. Various methods have been offered to overwhelm the disadvantages pointed out above. The mechanical activation of magnesium with various additives/catalysts attracts particular attention. The mechanical activation process provides the controllable synthesis of the nanosized materials distinguished by "softer" hydrogen sorption/desorption modes. The catalytic additives significantly reduce the operating temperatures and facilitate the kinetics of interaction between hydrogen and magnesium [12-18], also.

In this paper, we used graphite powders with different specific surface areas as an active additive to magnesium. The samples were synthesized by reactive ball milling under a hydrogen atmosphere.

2. Materials and method

The reactive ball milling technique under hydrogen (Fritsch Pulverisette P-6 ball mill) was applied to fabricate Mg-based composites. A special stainless steel milling bowl was designed to execute the mechanical activation procedure under a high-pressure hydrogen medium. The composition of the samples and specific surface area values (S_{BET}(C)) of the used graphitic powders are listed in table 1. The total duration of ball milling process for all samples was 30 hours. The milling process was divided into 15 min intervals to prevent the grinding container from overheating. Every 15 min milling interval was followed by a 1 min pause. The speed of rotation of the grinding container (n) and the ratio of the mass of the balls to the mass of the powder ($m_b : m_p$) were unchanged in all experiments and were n = 400 rpm. and $m_b : m_p = 30 : 1$, respectively. X-ray diffraction studies are carried out on the standard diffractometer with filtered Co K_α radiations in the Bragg-Brentano geometry. The interaction of magnesium-based composites with hydrogen was investigated on a homemade Sievert-type apparatus under isothermal conditions.

Table 1: *Chemical composition of samples.*

Sample №	The composition of the composite, wt. %		S_{BET}(C), m^2/g
	Mg	C (graphite)	
Mg-C0	100	-	-
Mg-C1	90	10	8,135
Mg-C2	90	10	329

3. Result and discussion

The XRD patterns of as-milled Mg-based composite are shown in Fig. 1.

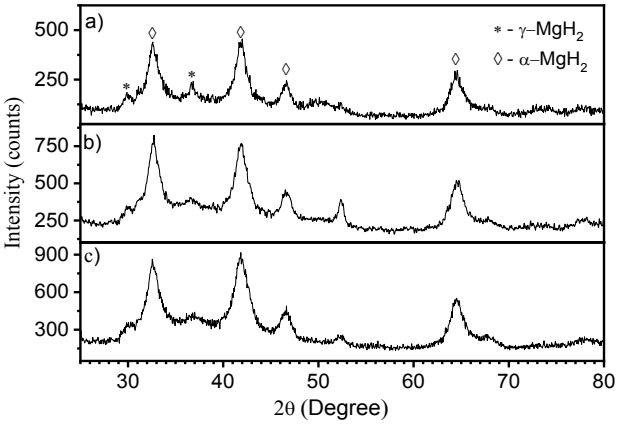

Fig. 1 *XRD pattern of as-milled Mg-based composite: a* – Mg-C0; *b* – Mg-C1; *c* – Mg-C2.

It should be noted the all samples have wide diffraction maximums with positions close to γ-MgH_2 and α- MgH_2 phases. It has been found by the Rietveld refinement procedure the graphite-free sample (Fig. 1, a) contains two phases: ~ 63 wt.% of α-MgH2 and ~ 37 wt.% of γ-MgH2. The crystallite sizes are 150 and 100 Å for α- MgH_2 and γ-MgH_2, respectively. Graphite additive with the 8.1 m^2/g surface area to magnesium leads to decreases ~ 53 wt.% of α- MgH_2 phase in a composite Mg-C1 (Fig. 1, b). However, the percentage of the γ-MgH2 phase in the Mg-C1 sample rises to ~47 wt.%. The crystallite size for α-MgH_2 and γ-MgH_2 hydrides are 100 and 30 Å, respectively. The Mg-C2 composite which contains graphite additive with the 329 m^2/g surface area has ~ 60 wt.% of α-MgH_2 and ~ 40 wt.% γ-MgH_2 phase (Fig. 1, c). The crystallite size for both phases is 100 Å.

The hydrogen sorption/desorption kinetics of the Mg-based composites was examined under isothermal conditions by Sievert's technique for as-milled and activated samples at 300 and 270 °C, respectively. Kinetics measurements were executed for the temperatures when the fastest hydrogen uptake/release processes were.

Fig. 2 shows the hydrogen desorption curves at 300 °C for the as-milled Mg-C composites and pure Mg.

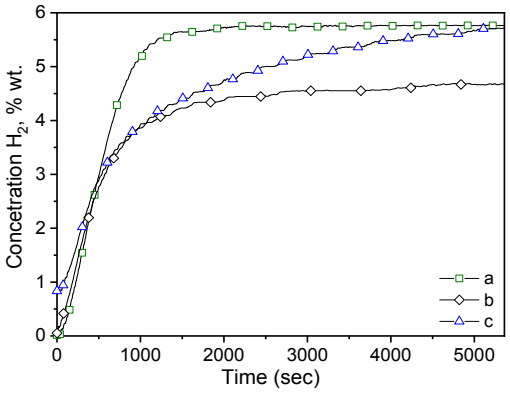

Fig. 2 *Desorption of hydrogen in isothermal conditions at T=300 °C for as-milled composites: a* – Mg-C0; *b* – Mg-C1; *c* – Mg-C2.

It is clear, that the best hydrogen kinetics and capacity are for the as-prepared graphite-free sample Mg-C0 (see Fig. 2, *a*). This sample desorbs 5.7 wt.% of hydrogen within 30 min at 300 °C. In contrast to the graphite-free sample, the graphite-containing ones show sluggish hydrogen release kinetics. So, the graphite containing samples Mg-C1 (Fig. 2, *b*) and Mg-C2 (Fig. 2, *c*) desorb 4.65 wt.% and 5.7 wt.% of H_2 more than twice slower for 80 and 85 min, respectively. It is worth noting that as-prepared composites Mg-C1 and Mg-C2 can release less hydrogen capacity and exhibit worse kinetics compared to pure magnesium.

After the activation of the samples, the behaviour of the hydrogen desorption curves is significantly different from the non-activated ones. Fig. 3 shows the hydrogen desorption curves recorded for the activated samples at 270 °C. A catalytic effect of graphite additive with different specific surface areas on the desorption process is noticeable. It can see that graphite less sample Mg-C0 (Fig. 3, a) at this temperature can desorb ~4.64 wt.% hydrogen for 57 min. Under the same conditions, Mg-C2 composite releases ~4.6 wt.% hydrogen within 59 min (Fig. 3, b). Thus, it is clear that the graphite powder with a specific surface area of 329 m^2/g affects the hydrogen desorption kinetics negligibly. The composite Mg-C1 with a small surface area of graphite additive ~8.1 m^2/g demonstrates an increased rate of dehydrogenation compared to other samples (Fig. 3, c). Under isothermal conditions, this sample releases ~4.2 wt.% of H_2 at 270 °C within 18 min.

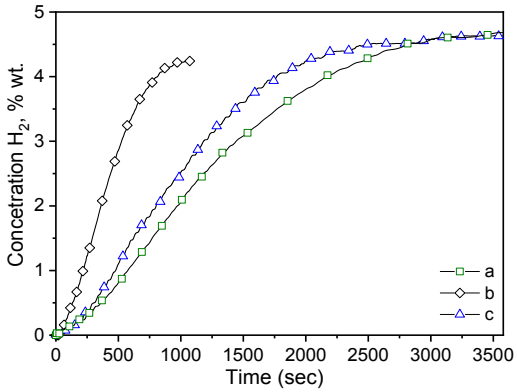

Fig. 3 *Desorption of hydrogen in isothermal conditions at T=270 °C for activated composites: a* – Mg-C0; *b* – Mg-C1; *c* – Mg-C2.

The studies of the hydrogen sorption kinetics under isothermal conditions at a temperature of 200 °C have been carried out (Fig. 4).

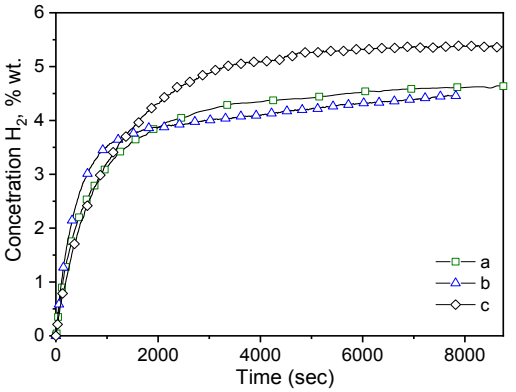

Fig. 4 *Sorption of hydrogen in isothermal conditions at T=200 °C for activated composites: a* – Mg-C0; *b* – Mg-C1; *c* – Mg-C2.

The maximum hydrogen storage capacity absorbed by Mg-C0 and Mg-C1 samples within 130 min is about 4.6 wt.% and 4.4 wt.%, respectively (Fig. 4, *a* and *b*). The composite Mg-C2 was saturated at a rate higher than Mg-C0 and Mg-C1 samples and reached a higher hydrogen capacity. It was found the Mg-C2 composite with graphite powder (329 m^2/g) uptakes 5.3 wt.% of hydrogen for 90 min (Fig. 4, *c*).

4. *Conclusion*

The Mg-C composites applying graphite powders with different specific surface areas (8.1 and 329 m^2/g) were produced by reactive ball milling technique in a hydrogen gas atmosphere. It was uncovered the surface areas of the graphite powder added to magnesium affect the hydrogen sorption/desorption kinetics of the Mg-based composites. The Mg-C1 composite (surface area of graphite is 8.1 m^2/g) shows the best hydrogen desorption kinetics. This sample releases ~4.2 wt.% of H_2 at 270 °C within 18 min. Also, the hydrogen sorption curves recorded under isothermal conditions for the 200 °C were analysed. It has been clarified that the Mg-C2 sample (surface area of graphite is 329 m^2/g) uptakes ~5.3 wt.% of H_2 within 90 min at 200 C.

5. Acknowledgments

This work is supported by youth project #06/01-2021(03) of the National Academy of Sciences of Ukraine.

6. References

1. L. Schlapbach, A. Züttel, Nature 414, 353 (2001)
2. Y. Huang, Y. Cheng, J. Zhang, *Ind. Eng. Chem. Res.* 60, 2737 (2021)
3. L. Schlapbach, *MRS Bull.* 27(09), 675 (2002)
4. A. Züttel, *Mater. Today* 6, 24 (2003)
5. H. Pan, Y. Liu, M. Gao, Y. Zhu, Y. Lei, *Int J Hydrogen Energy* 28(11), 1219 (2003)
6. Y. Kojima, Y. Kawai, S.-I. Towata, T. Matsunaga, T. Shinozawa, M. Kimbara, *J. Alloy. Compd.* 419, 256 (2006)
7. M. Kandavel, V. Bhat, A. Rougier, L. Aymard, G.-A. Nazri, J.-M. Tarascon, *Int. J. Hydrog. Energy* 33, 3754 (2008)
8. L. Pickering, J. Li, D. Reed, A.I. Bevan, D. Book, *Alloys. Compd.* 580, S233 (2013)
9. K. Wang, H. Du, Z. Wang, M. Gao, H. Pan, Y. Liu, *Int. J. Hydrog. Energy* 42, 4244 (2017)
10. I.P. Jain, C. Lal, A. Jain, *Int. J. Hydrog. Energy* 35, 5133 (2010)
11. A. Kadri, Y. Jia, Z. Chen, *Materials* 8, 3491 (2015)
12. Z.G. Huang, Z.P. Guo, A. Calka, D. Wexler, H.K. Liu, *Mater. Lett.* 61, 14-15 (2007)
13. A. Klimkowicz, A. Takasaki, Ł. Gondek, H. Figiel, K. Świerczek, *J. Alloys. Compd.* 645, S80 (2015)
14. G. Liu, Y. Wang, C. Xu, F. Qiu, C. An, L. Li, L. Jiao, H. Yuan, *Nanoscale* 5, 1074 (2013)
15. K. Alsabawi, T.A. Webb, E. MacA. Gray, C.J. Webb, *Int. J. Hydrog. Energy* 40, 10508 (2015)
16. C.Z. Wu, P. Wang, X. Yao, C. Liu, D.M. Chen, G.Q. Lu, H.M. Cheng, *J. Alloys. Compd.* 414, 259 (2006)
17. Y. Jia, Y. Guo, J. Zou, X. Yao, *Int. J. Hydrog. Energy* 37, 7579 (2012)
18. M. Lototskyy, J.M. Sibanyoni, R.V. Denys, M. Williams, B.G. Pollet, V.A. Yartys, *Carbon* 57, 146 (2013)

Effect of inoculation, cooling rate and charge composition on gray iron microstructure

Hirs Ana-Marija[1], Glavas Zoran[1], Strkalj Anita[1]
University of Zagreb, Faculty of Metallurgy, Sisak, Croatia [1]

E-mail: am.zamaria@gmail.com, glavaszo@simet.unizg.hr, strkalj@simet.unizg.hr

Abstract: *This paper analyses the effect of different charge compositions for melt production, cooling rate (i.e. casting wall thickness) and inoculation on the gray iron microstructure. In this study, three gray iron melts were produced that had almost the same chemical composition. The proportions of steel scrap (SS), pig iron (PI), gray iron return (GIR) and SiC in charge were as follows: melt 1 (10 % SS, 39.4 % PI, 49.2 % GIR, 0.6 % SiC), melt 2 (38.8 % SS, 9.9 % PI, 47.9 % GIR, 1.6 % SiC) and melt 3 (0 % SS, 0 % PI, 99.2 % GIR, 0.06 % SiC). One uninoculated and one inoculated stepped test casting with walls thicknesses of 5, 10, 20, 45 and 65 mm was casted from each melt. The inoculant was added in the melt stream during pouring in the mould in an amount of 0.23 wt.%. The type, size and distribution of graphite flakes in the analysed walls did not significantly depend on the charge compositions. The structure of the metal matrix, carbides precipitation and type, size and distribution of graphite flakes were largely dependent on the wall thickness. As the wall thickness increased, the cooling rate decreased and the type of graphite flakes changed, from D and E through B to A type. Carbide formation has occurred in the edge region of the 5 mm thick walls. With the decrease of the cooling rate and increasing the proportion of D and E type graphite flakes, the ferrite content in the metal matrix increased. The carbide content in the edge region of the 5 mm thick walls was significantly reduced by inoculation. Inoculation increased the proportion of A type graphite flakes in the middle of 5 mm thick wall and in walls with a thickness from 10 to 65 mm. In addition, inoculation significantly reduced the proportion of B, D and E type graphite flakes or were completely eliminated. Wall thickness has affected this effect.*

Keywords: GRAY IRON MICROSTRUCTURE, INOCULATION, COOLING RATE, CHARGE COMPOSITION

1. Introduction

Gray iron belongs to the group of cast irons in which carbon precipitates in the form of graphite [1 - 3]. Due to the flake shape of the graphite particles, gray iron has low tensile strength, hardness, toughness, elongation and modulus of elasticity and increased section sensitivity. The positive characteristics of gray iron are good machinability, very good damping of vibration, resistance to heat shocks, good castability and high compressive strength. It is widely used in various fields, such as machine building, production of castings for stoves and furnaces, process industry and energetics, motor vehicle industry, various constructions and decorative castings, and in many other areas.

The properties of gray iron depend on its microstructure. Through changes in the microstructure, different properties can be achieved. Numerous factors influence the microstructure of the gray iron, but the most important are: the chemical composition, the cooling rate of the casting in the mould during and after solidification (i.e., casting section thickness), raw materials for melt production, preconditioning and inoculation [4 - 20].

This article analyses the effect of different charge compositions for melt production, casting wall thickness and inoculation on the microstructure of gray iron.

2. Experimental

Three gray iron melts were produced in a medium-frequency induction furnace. The shares of the components in the charge are shown in Table 1. The chemical composition of the charge components is shown in Table 2.

Table 1: *Shares of components in charge.*

Component	Share in charge, wt.%		
	Melt 1	Melt 2	Melt 3
Pig iron (PI)	39.4	9.9	0
Steel scrap (SS)	10	38.8	0
Gray iron return (GIR)	49.2	47.9	99.2
SiC	0.6	1.6	0.06
FeP	0.7	0.6	0.06
FeS	0	0.1	0.08
Recarburizer	0.2	1.1	0.6

Table 2: *Chemical composition of charge components.*

	Share, wt.%						
	PI	SS	GIR	SiC	FeP	FeS	Recarburizer
C	4.41	0.09	3.56	2.90	0.1	0.3	min. 98
Si	1.25	0.13	2.05	-	1.86	0.96	-
Mn	0.13	0.71	0.43	-	1.91	-	-
P	0.08	0.024	0.32	-	25.72	0.01	-
S	0.02	0.014	0.091	0.05	0.04	49.37	max. 1.2
Cu	0.01	0.03	0.19	-	-	-	-
Cr	0.01	0.027	0.071	-	-	-	-
Al	-	-	-	0.06	-	0.01	-
Ti	-	-	-	-	1.2	-	-
SiC	-	-	-	90.04	-	-	-
SiO_2	-	-	-	2.8	-	-	-
Fe	bal.	bal.	bal.	0.4	bal.	bal.	-

Two stepped test castings (STC) containing 5, 10, 20, 45 and 65 mm thick walls were cast from each melt. One STC was cast without and the other with the addition of inoculant in the melt stream during pouring in the mould. The addition of inoculant was 0.23 wt.%. The inoculant of the following chemical composition was used: 73 - 78 wt.% Si, 0.1 wt.% Ca, 0.6 - 1 wt.% Sr, 0.5 wt.% Al, and the rest is Fe. It follows from the above that the STC 1, 3 and 5 are uninoculated and STC 2, 4 and 6 are inoculated.

Samples for metallographic analysis were cut from the middle of each wall in the STC. In addition, samples were taken from the edge of the wall thickness of 5 mm from all STC. Microstructure was analysed using light metallographic microscope with a digital camera. Samples were etched with 5 % natal.

3. Results and discussion

The chemical composition of the gray iron melts is shown in Table 3. It can be seen that the melts have a very similar chemical composition. This eliminates the influence of differences in chemical composition on the microstructure.

Table 3: *Chemical composition of gray iron melts.*

	Chemical composition, wt.%							
	C	Si	Mn	P	S	Cu	Cr	CE
Melt 1 (STC 1 and 2)	3.5	2.1	0.46	0.33	0.084	0.15	0.07	4.31
Melt 2 (STC 3 and 4)	3.53	2.12	0.4	0.36	0.1	0.18	0.07	4.36
Melt 3 (STC 5 and 6)	3.57	2.08	0.45	0.32	0.1	0.19	0.1	4.37

Figures 1 *and 2 show the microstructure of STC in unetched condition at 100x magnification.*

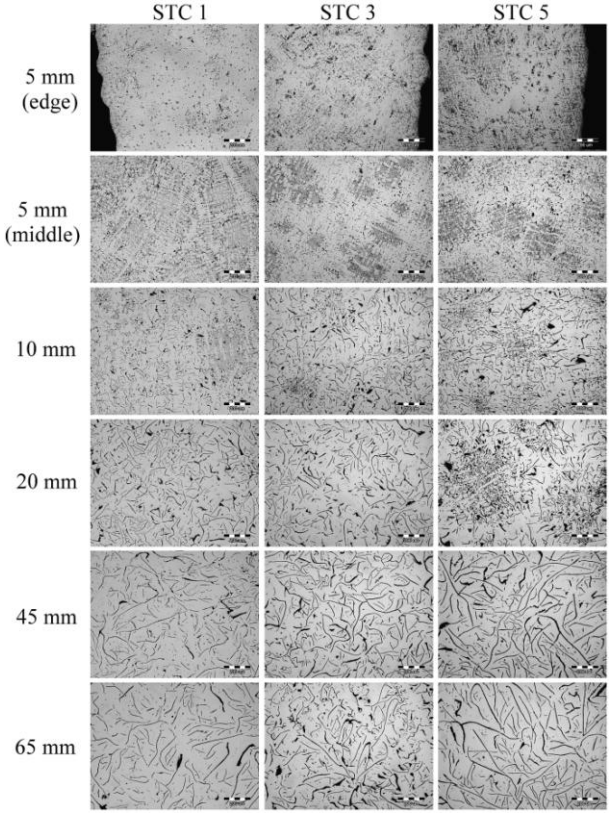

Fig. 1 *Microstructures of uninoculated STC (unetched).*

Figure 1 shows that small graphite flakes D and E type and a high proportion of carbides are present in the microstructure of the edge of 5 mm thick wall in uninoculated STC 1, 3 and 5. The highest proportion of carbides and the smallest proportion of graphite particles is present in STC 1, which was cast from the melt produced from the charge with the highest proportion of pig iron. The high solidification rate of the edge zone caused a large undercooling of the melt, which, in combination with inadequate nucleation and graphitization potential (originating from a low content of silicon), resulted in the formation of carbides. In addition, rapid solidification and greater undercooling of the melt favour the creation of D and E type graphite flakes. Inoculation improves the nucleation potential of the melt, which is why the 5 mm thick wall from STC 2, 4 and 6 contains a higher proportion of graphite phase and a smaller proportion of carbides, which are almost completely eliminated in STC 6 (Figure 2). Graphite flakes are still D and E type.

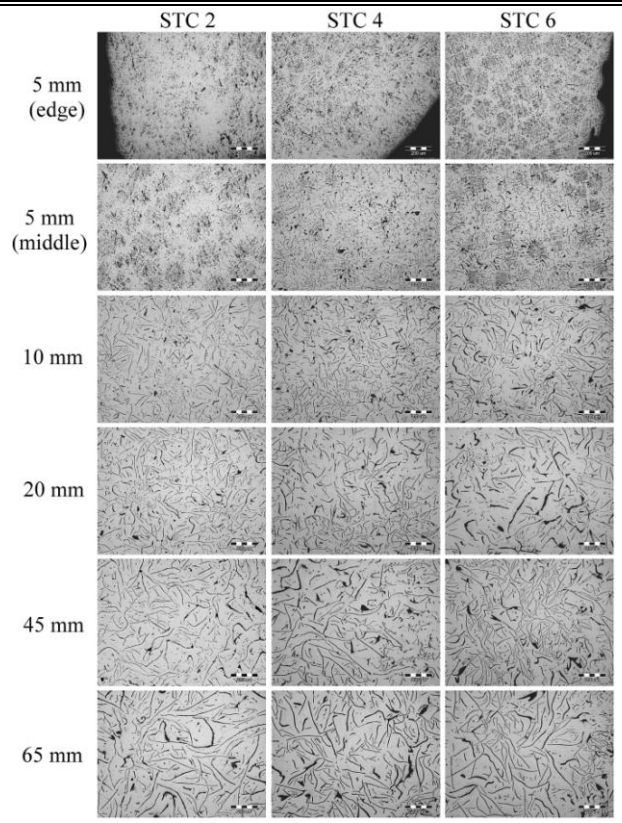

Fig. 2 *Microstructures of inoculated STC (unetched).*

In the microstructure of the middle part of the 5 mm thick wall from STC 1, D type graphite flakes predominate, with a smaller proportion of E type graphite flakes (Figure 1). STC 3 and 5 also contain D type graphite flakes, but their proportion is smaller than in STC 1 (Figure 1). In addition, their microstructure contains a certain proportion of A and B type graphite flakes. The presence of graphite flakes A and B type indicates a more favourable nucleation potential and less undercooling of the melt (especially in the case of A type graphite flakes). In the middle of the wall thickness of 5 mm from STC 1, 3 and 5 carbides are not present, although they are not inoculated. Slower solidification of the central part relative to the edge of the wall with a thickness of 5 mm prevented the formation of carbides. Figure 2 shows that the improvement of nucleation potential by inoculation favourably affected the morphology of graphite flakes. STC 2 contains a smaller proportion of D type graphite flakes compared to STC 1. STC 4 contains graphite flakes A and B type, not graphite flakes D type as STC 3, which was cast from the same melt but without the addition of inoculant. STC 6 also contains A and B type graphite flakes and a very small proportion of D type graphite flakes (significantly smaller than in STC 5).

The wall thickness of 10 mm from STC 1 contains A and B type graphite flakes and a smaller proportion of D type graphite flakes (Figure 1). Inoculation eliminated D type graphite flakes and increased the proportion of A type graphite flakes (STC 2, Figure 2). The slower solidification of the wall thickness of 10 mm compared to the wall thickness of 5 mm resulted in a lower undercooling of the melt. This favours the formation of B type graphite flakes, but also the formation of A type graphite flakes if the undercooling is low and the nucleation potential of the melt is favourable. STC 3 and 5 contain A and B type graphite flakes, and a smaller proportion of C type graphite flakes, which appear due hypereutectic composition of the melt (Figure 1). Inoculation increased the proportion of A type graphite flakes and decreased the proportion of B type graphite flakes (STC 4 and 6, Figure 2).

Type A graphite flakes are present in the microstructure of a 20 mm thick wall from STC 1, 3 and 5 (Figure 1). In addition, the STC 5 also contains a certain proportion of B type graphite flakes (Figure 1). This indicates a favourable nucleation potential and

slower solidification. Improving nucleating potential by inoculation increased the proportion of A type graphite flakes and eliminated B type graphite flakes (Figure 2).

Figure 1 shows that the wall thickness of 45 mm in all STC contains A type graphite flakes and a smaller proportion of C type graphite flakes. The slower cooling and sufficiently suitable nucleation potential of the melt favoured the formation of A type graphite flakes. Inoculation further increased the proportion of A type graphite flakes and reduced their size to some extent (Figure 2).

Figure 1 shows that the wall thickness of 65 mm in all STC contains A and C type graphite flakes. Similar effects as in a 45 mm thick wall were achieved by inoculation.

Comparing the microstructures shown in Figures 1 and 2, it can be seen that increasing the wall thickness results in a change in the type of graphite flakes - from D and E through B to A type. Increasing the wall thickness decreases the cooling rate and the undercooling of the melt. This creates favourable conditions for the formation of A type graphite flakes, which are also the most suitable. In addition, it can be seen that the number of A and C type graphite flakes decreases and their size increases with increasing wall thickness, which is the result of slower solidification.

STC 1 and 2 which are casted from the melt produced from the charge with 39.4 wt.% of pig iron did not prove superior in terms of the morphology of the graphite flakes in comparison to other STC that are made from melts without or with very low content of pig iron in the charge. It should be taken into consideration that the charge for making melt 2 contained the highest proportion of steel scrap, but also the highest proportion of SiC. The strong preconditioning of the melt with SiC had a beneficial effect on its nucleation potential, which ultimately affected the type, size and distribution of graphite flakes and carbide formation.

Figures 3 and 4 show the microstructure of STC in etched condition at 100x magnification.

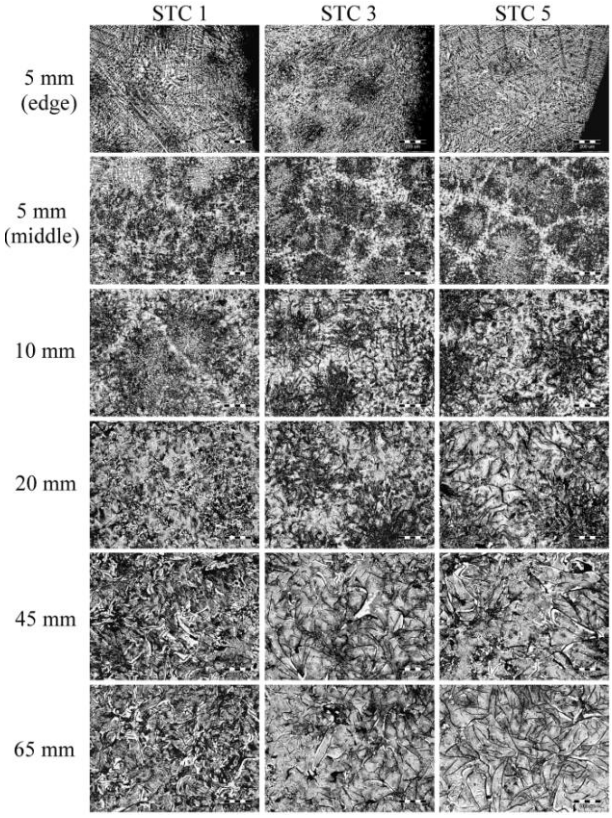

Fig. 3 *Microstructures of uninoculated STC (etched).*

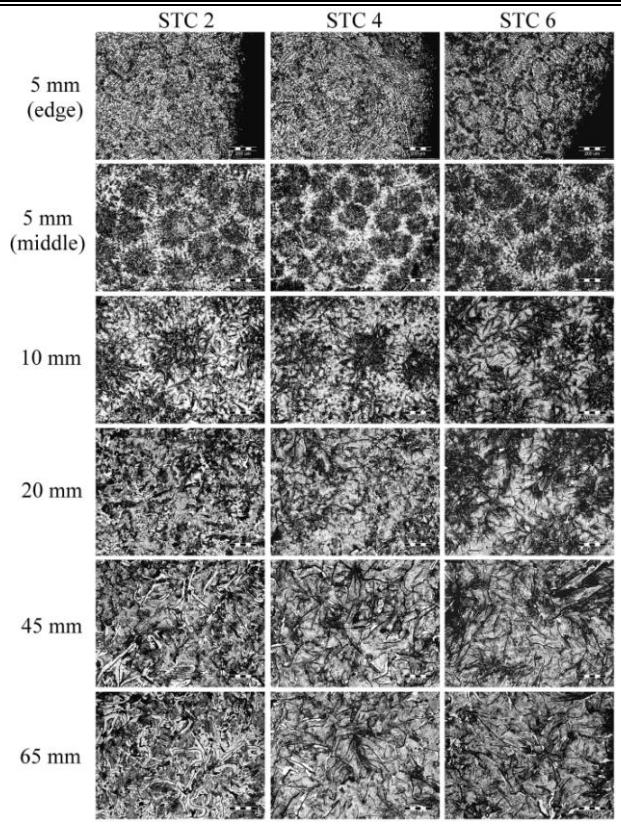

Fig. 4 *Microstructures of inoculated STC (etched).*

Figure 3 shows that in STC 1, 3 and 5 the edge of the wall thickness of 5 mm has a pearlitic metal matrix, while in STC 2, 4 and 6 the metal matrix is ferritic-pearlitic (Figure 4). Pearlite content is much higher than ferrite content due to high solidification rate. Ferrite is present in areas where D type graphite flakes are found. Because they are extremely small and branched flakes, the carbon diffusion paths from austenite are significantly shortened. This facilitates the reduction of the carbon content in austenite and its transformation into ferrite. In addition to the constituents mentioned above, carbides and a phosphide eutectic network were found in the microstructure. The increased phosphorus content in melts resulted in the formation of a phosphide eutectic.

The middle of the wall thickness of 5 mm in all STC (inoculated and uninoculated) has a pearlitic-ferritic metal matrix (Figures 3 and 4). As well as on the edge, the pearlite content is greater than the ferrite content, which is found around the D type graphite flakes. The phosphide eutectic network can be clearly seen in all samples. Carbides are not present in the middle of this wall, but not in other thicker walls because of slower cooling.

The metal matrix of the wall thickness of 10 mm in all STC contains a high proportion of pearlite (Figures 3 and 4). Ferrite is present in a smaller proportion, mainly in areas where small flakes of graphite are found (B and D type), and to a lesser extent around A type graphite flakes. As in the previous wall, a phosphide eutectic, which is located along the grain boundaries, is also present in this wall.

The wall thickness of 20 mm in all STC has a pearlitic-ferritic metal matrix with a high content of pearlite (Figures 3 and 4). Ferrite is located around graphite flakes. A phosphide eutectic is also present in the microstructure. It is surrounded by pearlite, as in the previously mentioned walls.

The 45 and 65 mm thick walls in all STC also have a pearlitic-ferritic metal matrix and contain a phosphide eutectic (Figures 3 and 4). The ferrite content is higher than in the previous walls due to the slower cooling, which is a result of the greater thickness of the walls.

4. Conclusion

Based on the results of research of the influence of different charge compositions for melt production, casting wall thickness and inoculation on the gray iron microstructure, the following can be concluded:

- the type, size and distribution of graphite flakes in the analysed wall thicknesses of 5, 10, 20, 45 and 65 mm did not significantly depend on the content of pig iron, steel scrap and gray iron return in the charge,
- preconditioning with SiC improves the nucleation potential of the gray iron melt, which is especially evident in the melt made from the charge containing a relatively high proportion of steel scrap (~ 40 %),
- solidification rate, i.e. the wall thickness, greatly influences the type, size and distribution of graphite flakes, carbide formation and the structure of the metal matrix,
- in thin walls (5 mm), due to the high solidification rate, a large undercooling of the melt is produced, which ultimately results in the formation of D and E type graphite flakes,
- with increasing wall thickness (from 10 to 65 mm), i.e. with decreasing solidification rate, the conditions for the formation of A and B type graphite flakes are created,
- in thin walls (5 mm), the presence of carbides can be expected, especially in the edge region where the solidification rate is greatest,
- with decreasing cooling rate and increasing the proportion of D and E type graphite flakes increases the proportion of ferrite in the metal matrix of gray iron,
- inoculation significantly affects the microstructure of gray iron because it improves the nucleation potential of the melt,
- corresponding addition of inoculant reduces or almost completely eliminates the formation of carbides in thin walls, decreases the proportion of B, D and E type graphite flakes, and increases the proportion of A type graphite flakes,
- phosphorus content > 0.3 wt.% results in the formation of phosphide eutectic in wall thicknesses of 5, 10, 20, 45 and 65 mm.

5. References

[1] T. Fugal, G.M. Goodrich, V. Patterson, M. Mroczek, J. Ward, G. Goodrich, C. Callison, C.A. Bhaskaran, L. Helm, A. Shturmakov, J. Way, Introduction to Gray Cast Iron Processing, American Foundry Society, Des Plaines, Illinois, SAD 2000.

[2] D.B. Craig, M.J. Hornung, T.K. McCluhan, Gray Iron, chapter in ASM Handbook, Volume 15, Casting, ASM International, Metals Park Ohio, 1998., 1365 - 1404.

[3] J.R. Brown, Foseco Ferrous Foundryman's Handbook, Butterworth-Heinemann, Oxford, 2000.

[4] E. Weiss, G. Fedorko, P. Futáš, A. Pribulová, I. Vasková, Dependence of Quality Properties for Grey Iron on Used Raw Materials, Metalurgija 48(2009) 1, 43 - 45.

[5] …, The Use of Foundry Pig Iron in Grey Iron Castings, https://www.metallics.org/assets/files/Public-Area/Fact-Sheets/_7_Foundry_Pig_Iron_Fact_Sheet_rev3.pdf (Accessed: June 19, 2019)

[6] D. Bartocha, K. Janerka, J. Suchoń, Charge Materials and Technology of Melt and Structure of Gray Cast Iron, Journal of Materials Processing Technology 162–163 (2005), 465–470.

[7] K.B. Rundman, Metal Casting, Reference Book for MY4130, Michigan Tech. University, 1986.

[8] J. Dawson, S. Maitra, Recent Research On the Inoculation of Cast Iron. British Foundryman 60(1967) 4, 117 - 127.

[9] M. Jacobs, T. Law, D. Melford, M. Stowell, Basic Processes Controlling the Nucleation of Graphite Nodules in Chill Cast Iron, Metals Technology 1(1974) 1, 490 -500.

[10] T. Elbel, J. Senberger, A. Zadera, J. Hampl, Behaviour of Oxygen in Cast Irons, Archives of Materials Science and Engineering 33(2008) 2, 111 - 116.

[11] J. Campbell, A Hypothesis for Cast Iron Microstructures, Metallurgical and Materials Transactions B 40(2009) 6, 786 - 801.

[12] M. Chisamera, I. Riposan, S. Stan, C. Militaru, I. Anton, M. Barstow, Inoculated Slightly Hypereutectic Grey Cast Irons, Journal of Materials Engineering and Performance 21(2012) 3, 331 – 338.

[13] I. Riposan, M. Chisamera, S. Stan, T. Skaland, A New Approach to Graphite Nucleation Mechanism in Gray Irons, Proceedings of the AFS Cast Iron Inoculation Conference, September, 29-30, 2005, Schaumburg, Illinois, 31 – 41.

[14] W. Weis, The Metallurgy of Cast Iron, Proceedings of the Second International Symposium on the Metallurgy of Cast Iron, The Metallurgy of Cast Iron, eds. B. Lux, I. Minkoff, F. Mollard, Georgi Publishing, Geneva, Switzerland, 29 – 31 May 1974., 69 – 79.

[15] D.M. Stefanescu, Science and Engineering of Casting Solidification, Kluwer Academic/Plenum Publishers, New York, 2002.

[16] … Overview of Alloying Elements and their Effects in Grey Iron, Tehnical Information 12A, Elkem ASA, Oslo, Norway, 2011. http://foundrygate.com/upload/artigos/7ZmcrE9zgVGm6iKwHxeNNjbEdqt1.pdf. (Accessed: June 19, 2019).

[17] M.I. Onsoinen, T. Skaland: Preconditioning of Gray Iron Melts Using Ferrosilicon or Silicon Carbide, AFS Transactions 109(2001), Paper 01-093.

[18] …, Preseed Preconditioner, Elkem, Foundry Products, Oslo, 2012. https://www.yumpu.com/en/document/view/32276377/preseedtm-preconditioner-elkem (Accessed: June 19, 2019).

[19] Z. Glavaš, F. Unkić, J. Martišković, Predobrada i metalurška kvaliteta talina sivih željeznih ljevova, Ljevarstvo 51(2009) 2, 47 - 56.

[20] I. Riposan,M. Chisamera, S. Stan, Enhanced Quality in Electric Melt Grey Cast Irons, ISIJ International 53(2013) 10, 1683 – 1695.

The features of recrystallization of steels under laser action

Svetlana Gubenko
Iron and Steel Institute of National Academy of Science of Ukraine,
Prydniprovska State Academia of Civil Engineering and Architecture
Dnepr, Ukraine
sigubenko@gmail.com

Abstract. *The features of recrystallization of steels with different chemical composition and type of crystal lattice under laser action were investigated. These processes are of great importance in high-speed laser heating and cooling, as well as in the formation of the microstructure of steels under the influence of residual heat.*
It was found that recrystallization under laser action has signs of a dynamic process due to an increase in the dislocation density. In addition, the dislocation substructure of steel is inherited from the initial hot-deformed state. It is shown that the mechanism of laser recrystallization depends on the type of steel, chemical composition, and crystal lattice.
In different steels, the development of primary, collective, and secondary recrystallization was observed. In this case, the change in the grain structure of steels took place against the background of an increased density of dislocations and the formation of a cellular dislocation substructure.
KEYWORDS: *STEEL, RECRYSTALLIZATION, LASER ACTION, MICROSTRUCTURE, STRESSES, HIGH SPEED RELAXATION*

1.Introduction.

Laser processing is widely used to strengthen various steel products. During this treatment, structural and phase transformations in steel proceed at a very high rate. In this case, the critical points of transformations are shifted upward on the temperature scale relative to their equilibrium value by 50...100 °C [1-3]. Numerous studies have established that the effect of strengthening steels under laser irradiation is achieved by high-temperature strengthening, martensitic transformation, obtaining an ultrafine structure, dissolution of carbides and non-metallic inclusions, saturation of the matrix with their components, microchemical inhomogeneity, an increase in the number of defects in the crystal structure and plastic shears [1-11] . All these factors act simultaneously and it is not always possible to separate their influence in the study of steels traditionally subjected to laser processing, especially in steels with a complex structure. The goal of the work was to study the features of high-speed recrystallization in steels with different chemical composition and type of crystal lattice under laser action.

2. Materials and Procedures.

Specimens made of hot-deformed steels 08Yu, 08Kp, 08H18N10T, E3 were irradiated by laser in GOS-30M and Quantum-16 installations with an excitation voltage of 2,5kV and pulse energy of 18 J at heating rate of 10^5 °C/s and cooling rate of 10^6 °C/s with action time of 3,6 $\cdot 10^{-3}$ s. These steels can be considered model alloys because they have a single-phase structure or a structure with a small amount of a second phase and contain little carbon (see tabl. 1). Such a set of research objects made it possible to obtain relatively simple types of matrix with different impurities and crystal lattices. The microstructure of steels in the laser impact zone was studied using a Neophot-31 light microscope and a Tesla electron microscope. The dislocation density, block sizes, and texture in a thin surface layer were evaluated on a DRON-2.0 X-ray diffractometer.

Table 1. *Chemical composition of the steels*

Steel	Element content, %									
	C	Mn	Si	Cu	Cr	Al	Ti	Ni	S	P
08Kp	0,09	0,32	0,01	0,22	0,05	0,01	-	0,05	0,025	0,009
08Yu	0,07	0,29	0,01	0,07	0,03	0,04	-	0,05	0,022	0,007
E3	0,035	0,10	3,1	0,09	0,05	0,013	-	0,09	0,005	0,005
08H18N10T	0,08	1,2	0,80	0,07	18,0	-	0,6	10,1	0,021	0,006

3. Results and discussion.

In [2, 5], the features of phase transformations, in particular, the austenitization of steels during laser heating, were studied. It has been established that phase transformations are accompanied by polygonization [12] and recrystallization [5] due to internal strengthening and having a static character. It was shown in [13] that the kinetic regularities of recrystallization upon conventional and laser annealing are similar. However, it was established in [2, 14, 15] that, during laser treatment, the dislocation density increases by several orders of magnitude, and the level of microdistortions of the crystal lattice increases by several times, which indicates plastic shears and is directly stated by the authors of [15].

Structural changes in the zone of laser impact in low-carbon steels took place under conditions of high temperature and a powerful shock pulse. The short duration of such a powerful impact inevitably generates shock microwaves. The impact of a laser beam is similar to a microexplosion (thermal shock), shock waves develop huge pressures [2], leading to plastic deformation, which manifests itself in a very short time of shock compression. Under these conditions, the stresses in the thin surface layer of steel exceed the yield strength and the material is able to flow. As a result, dislocations and vacancies multiply, dislocation reactions occur, and a significant concentration of nonequilibrium vacancies is created.

An analysis of the microstructure of hot-rolled steels showed that in the zone of laser irradiation, the grains become larger by 1 ... 3 points (from 8 to 5 ... 6 points, GOST 5639) compared with the initial state, i.e., collective recrystallization occurs. Steels 08Yu and 08kp differ in the chemical composition by the presence of aluminum in the former. After laser treatment in steel 08Yu, the grain size increased by 1...2 points (from 8...10 to 6...7 points), in steel 08kp - by 2...3 points (from 8 to 5...6 points) (Fig. 1, a, b). Such a difference in the degree of grain size increase is associated with the barrier effect of aluminum nitride particles AIN (Fig. 1c). At the moment of laser exposure, inclusions of aluminum nitrides partially dissolve: in these places, the grain boundaries are capable of migration and the grains grow. The laser exposure zone is characterized by the presence of wavy grain boundaries, which in the surface layers are perpendicular to the sample surface. This is due to the direction of exposure and heat removal and causes the appearance of signs of a columnar structure.

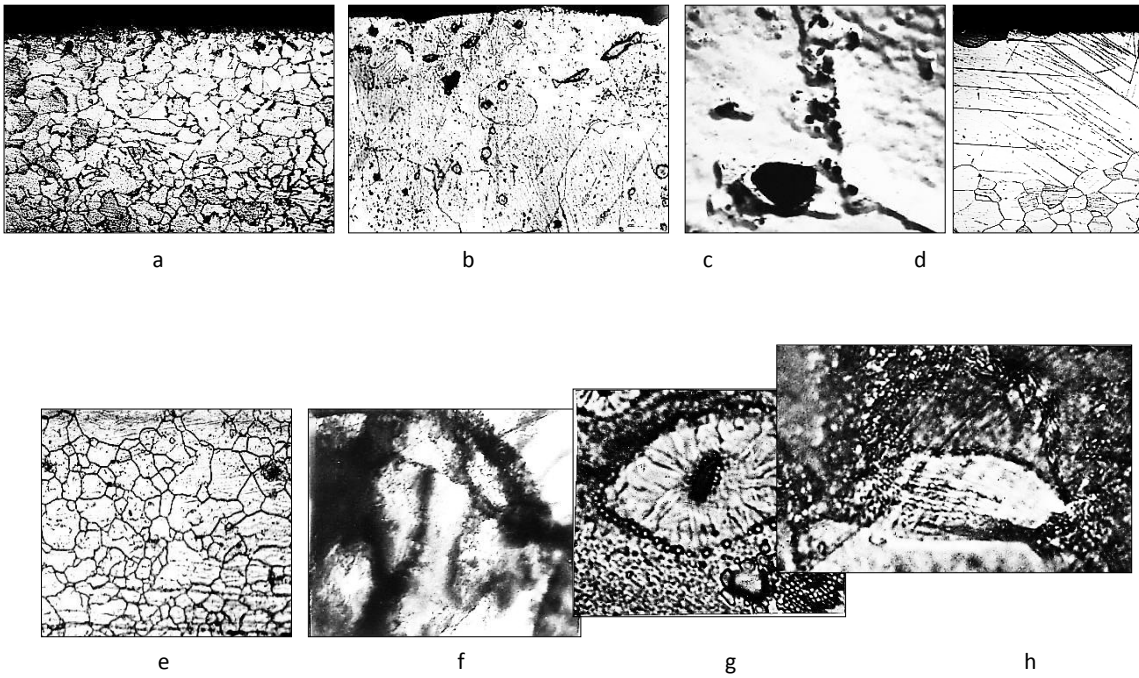

Figure 1. *Microstructure of hot-rolled steels 08Yu (a, c, g), 08kp (b, h), E3 (d), 08Kh18N10T (e, f) in the laser impact zone: a, b, d, e, h, x600, c - x20000, f - x50000, g - x1000.*

In E3 steel, ferrite grains increased by one point (from 4 to 3 points). It is known that this steel is practically not prone to collective recrystallization, since the grain boundaries in the alloyed ferrite are inactive due to their fixation by particles of dispersed precipitates and the resulting recrystallization texture [15]. Secondary recrystallization or anomalous grain growth was observed in the zone of laser impact of E3 steel in places with favorably oriented grains (Fig. 1d). In austenitic steel 08H18N10T, the grains also became coarser by 1...2 points (from 9...10 to 7...8 points) in comparison with the initial sizes (Fig. 1, e). In the zone of laser impact, a lot of so-called "dangling" boundaries are visible, which is typical for this steel [16]. In steel 08Yu, fragments of grain boundaries and subboundaries are also visible. Recrystallization under laser action of 08H18N10T and 08Yu steels was accompanied by spliting of the grain boundaries and formation of the special boundaries in their structure. Thus, in the case of laser action, as in conventional annealing, collective recrystallization is suppressed in alloyed ferrite and austenite, but secondary recrystallization develops.

Non-metallic inclusions were the centers of nucleation of recrystallized grains in the steel, as in conventional annealing or any type of high-speed heating [16, 17], while the short time allotted for the relaxation of deformation and thermal stresses creates conditions for the nucleation of several recrystallization nucleus near one inclusion, where recrystallized grains of a specific petal character appear (Fig. 1g).

In the zone of laser impact in all hot-worked steels, the slip lines and microcracks were observed, indicating significant plastic deformation (Fig. 1h). In the grains of E3 steel, a large number of twins of the several systems were found that intersect each other (see Fig. 1, d). In addition, traces of the sliding along several systems were revealed. In some places, the deformation had a clearly vortex (rotational) character, the sliding “torches” were observed at the intersections of twins with each other and with the grain boundaries, as well as zones of deformation by the dumping**.** During laser processing, plastic-plastic relaxation in hot-worked steels proceeds by the shear and rotational mechanisms. Observations testify to the high-speed nature of the deformation, which has a number of features: the number of dislocation sources and slip systems increases, and the velocity of dislocations in slip planes increases too [1–4, 15]. The short duration and locality of the laser impact contributes to the constraint of plastic deformation when local plastic rotations of microregions are carried out. The fields of elastic stresses can relax due to plastic rotations of the lattice of conjugated grains. The constraint of plastic stress relaxation under laser irradiation is also due to the specifics of high-speed mass transfer [18, 19], which is realized, in contrast to diffusion processes occurring during conventional heating.

The study of fine structure of steel 08Yu using an electron microscope showed that in the zone of laser action there are areas with dislocation clusters and a developed cellular substructure (Fig. 1f), which occupy 40 and 60% of the area of the studied samples, respectively. The dislocation substructure of steel after laser exposure differs from the initial hot deformation substructure by the presence of small dislocation coils and thin mid-angle subboundaries. The formation of a cellular substructure in the 08Yu steel during laser exposure indicates a significant plastic deformation that has taken place in the grains. In austenitic steel 08H18N10T, the areas of interlacing and flat accumulations of dislocations are also observed, there are zones with a cellular substructure. Table 2 shows the dislocation density in the steels in the hot-rolled state and after laser processing. It can be seen that the density of dislocations in the zone of laser action in all steels increased by two orders of magnitude compared to the hot-rolled state. In addition, laser processing resulted in almost 3-fold refinement of the blocks (from 61.10^{-5} to $19.5.10^{-5}$ cm), which indicates the presence of microdistortions in the crystal lattice of the solid solution.

Table 2. *Dislocation density ρ before (1) and after laser exposure (2)*

Steel	Dislocation density ρ, cm^{-2}	
	1	2
08Yu	$1,3 \times 10^{8}$	$3,54 \times 10^{10}$
08Kp	$2,0 \times 10^{9}$	$1,4 \times 10^{11}$
08H18N10T	$4,6 \times 10^{8}$	$8,2 \times 10^{10}$

X-ray studies showed that a weakly developed crystallographic texture (110)α arose in the laser impact zone; part of the grains is oriented by this plane parallel to the sample surface.

The mode of laser irradiation used in the present studies was selected empirically in order to exclude heating of the steel above the structure change induced by phase transformation $\alpha \leftrightarrow \gamma$ start point. The proof that no polymorphic transformation occurred under the studied irradiation conditions is evidenced by the following facts:

- steel grains have grown, not crushed. If a polymorphic transformation occurred, and even a double one (during heating and cooling), at such high heating and cooling rates, the many phase transformation centers would arise and the structure would form fine-grained; - the same results were obtained both for steels in which polymorphic transformation is possible (08kp, 08Yu), and for steels where it is excluded (E3, 08KH18N10T), moreover, having a different crystal lattice;

- sulfide inclusions did not melt during heating, but they melt at temperatures above 950 ^{o}C [11, 20, 21].

4. Conclusions.

In the zone of laser action of hot-worked steels, structural signs of two processes are observed - collective or secondary recrystallization and high-speed shear or rotational plastic deformation. These processes run in parallel, so it should be considered that at the moment of pulsed laser irradiation, dynamic collective or secondary recrystallization develops in steels. The specific conditions of laser exposure, mainly its short duration and localized powerful energy, ensured the processes of restoring the structure of a dynamic nature.

5. Literature.

1. Vedenov A.A., Gladush G.G. Physical processes in laser processing of materials. - Moscow: Energoatomizdat, 1985, 207 p.

2. Redi J. Industrial applications of lasers. - Moscow: Mir, 1981, 638 p.

3. Laser and electron-beam processing of materials / Rykalin N.N., Uglov A.A., Zuev I.V., Kokora A.N. - Moscow: Mashinostroenie, 1985, 496 p.

4. Laser and electroerosion hardening of materials / Kovalenko V.S., Verkhoturov A.D., Golovko L.F., Podchernyaeva I.A. - Moscow: Nauka, 1986, 276 p.

5. Stavrev D., Shtarbakov V., Dikova Ts. Structure and properties of iron-carbon alloys after impact with concentrated energy flows. - Bulgaria, Varna: STENO, 2015, 264 p.

6. Gubenko S.I. Structural effects near nonmetallic inclusions in laser treatment of steels. Materials Science, 1999, v. 35, N6, pp. 818 – 823.

7. Gubenko S.I. Possibilities of transformation of non-metallic inclusions and interphase inclusion-matrix boundaries under high-energy treatments / Metal Physics, New Technologies, 2014, V. 36, N 3, pp. 287-315

8. Gubenko S.I. Zones of contact interaction in steel matrix near inclusions under the laser action. Materials Science, 2011, v. 46, No 4, pp. 448-452.

9. Gubenko S.I., Nikulchenko I.A. Fragmentation of Nonmetallic Inclusions during Local Remelting upon Laser Steel Processing. Steel in Translation, 2020, vol. 50, No. 3, pp. 203-208.

10. Gubenko S. I. Strucrural Effects near Nonmetallic Inclusions in Laser Treatment of Steels. Materials Science, 2000, v.35, No 6, pp. 818-827.

11. Gubenko S.I., Oshkaderov S.P. Non-metallic inclusions in steel. – Kiev: Naukova dumka, 2016, 528 p.

12. Nowitzki M. Lasers in electronic technology and material processing. Moscow: Mashinostroenie, 1981, 149 p.

13. Strengthening of parts with a laser beam / Kovalenko V.S., Golovko L.F., Merkulov G.V., Strizhak A.I. - Kiev: Technique, 1981, 131 p.

14. Leontiev P.A., Chekanov N.T., Khan M.G. Laser surface treatment of metals and alloys. - Moscow: Metallurgy, 1986., 142 p.

15. Krishtal M.A., Zhukov A.A., Kokora A.N. Structure and properties of alloys treated with laser radiation. - Moscow: Metallurgy, 1973, 192 p.

16. Gubenko S.. Physical nature of the ductility and strengthening of metals during deformation. - Germany-Mauritius, Beau Bassin: Palmarium academic publishing, 2020, 341 p.

17. Ivanov V.I., Osipov K.A.. Recovery and recrystallization in metals during rapid heating. - Moscow, Nauka, 1984, 185 p.

18. Larikov L.N., Mazanko V.F., Falchenko V.M. Mass transfer in metals under pulsed loading. Physics of Metals and Metallurgy, 1983, No. 6, pp. 144-145.

19. Gurevich ME, Zhuravlev AF, Kornyushin Yu.V., Pogorelov AE On the nature of mass transfer in metals under laser irradiation. Metallophysics, 1985, vol. 7, No. 2, pp. 113-114

20. Gubenko S.I., Varavka V. N. Behavior of sulfide inclusions during laser thermal strengthening of steel. Physics and chemistry of material processing, 1985, No 6, pp.23-27.

21. Gubenko S.I., Varavka V. N. Behaviour of Sulphide Inclusions in Laser Thermal Hardening of Steel. Technical Translations, Cambridge (United Kingdom), 1986.

The Electrothermal Processes During High-voltage Electric Pulse Consolidation of Refractory Powder Materials

Evgeny Grigoryev.[1], Oleg Kuznechik[2], Alexander Chumakov[3], Irina Nikonchuk[3], Evgeny Strizhakov[4], Stanislav Nescoromniy[4], Stanislav Ageev[4]
Merzhanov Institute of Structural Macrokinetics and Materials Science Russian Academy of Sciences, Chernogolovka, Russia[1]
State Scientific Institution "POWDER METALLURGY INSTITUTE", Minsk, Belarus[2]
B. I. Stepanov Institute of Physics, National Academy of Sciences of Belarus, Minsk, Belarus[3]
Don State Technical University, Rostov-on-Don, Russia[4]
eugengrig@mail.ru

Abstract: *The main features of high-voltage electric pulse consolidation (HVC) of refractory powder materials and the resulting unique capabilities of the method are considered. The electro-thermal processes of HVC at the contacts between powder particles and at the macroscale of the entire consolidated sample are analyzed. The results of experimental studies of the parameters of high-voltage electrical impulse action in the processes of consolidation of high-temperature powder compositions, high-voltage welding of dissimilar materials, as well as high-voltage discharges in liquid are presented. The results of measuring the intensity of thermal radiation of the investigated materials under high-voltage electrical impulse action, recorded by the method of pulse photometry using photodiode sensors, which, together with the Rogowski coil, are components of the measuring complex developed by the authors, are presented.*
Keywords*: HIGH-VOLTAGE ELECTRIC PULSE CONSOLIDATION, REFRACTORY POWDER MATERIALS, ELECTROTHERMAL PROCESSES*

1. Introduction

The method of high-voltage consolidation of powders is effective for the production of refractory composite materials that retain their strength properties at ultrahigh temperatures under aggressive external influences. The short duration of high-temperature exposure in the process of high-voltage consolidation makes it possible to preserve the structural-phase state of the initial powder material in the consolidated compact material. A feature of this method is the high density concentration of the released energy in the area of contacts between powder particles. The initial state of the surface of powder particles (the thickness and structure of oxide films, the presence of foreign impurities, etc.), the shape of powder particles and their sizes significantly affect the regularities of high-voltage consolidation process. Along with the characteristics of the powder, the determining factors are: the rate of input of the energy of the electromagnetic field into the powder material, the magnitude and nature of the mechanical pressure acting on the powder blank during high-voltage consolidation. The high energy density in the particle contact zones leads to a local change in the state of aggregation of the powder substance in these zones. Along with the inhomogeneity of powder heating in interparticle contacts, a macroscopically inhomogeneous distribution of the current density in the volume of the consolidated sample is possible. The formation of the structure of a powder material during high-voltage consolidation is determined by processes of different scales occurring at interparticle contacts, in powder particles, in the bulk of the entire sample, and by the mutual influence of these processes. The advantages of the high-voltage consolidation method can be fully realized with optimal process parameters, since intense electro-thermal action on the powder material can lead to instability of the consolidation process, the formation of an inhomogeneous structure of the material to be consolidated, and even to the destruction of the consolidated sample and technological equipment. The study of electro-thermal phenomena, both in the particle contact zones and on the scale of the entire consolidated sample, makes it possible to establish the optimal parameters of high-voltage consolidation.

2. Theoretical analysis

As a result of theoretical analysis of electro-thermal processes in contacts between powder particles during high-voltage consolidation [1], the threshold value of the current density j* in the interparticle contact was established, the excess of which causes an electrothermal explosion:

$$j_* = \sqrt{\frac{2\xi\sigma}{\rho h}} T_b^2 \quad , \qquad (1)$$

where: σ is the Stefan-Boltzmann constant; $\xi \le 1$; T_b is the boiling point (loss of conductivity) of the powder material, ρ is the resistivity of the material, h is the thickness of the interparticle contact. The validity of criterion (1) was confirmed experimentally on grains of the nickel heat-resistant alloy (EP741), and the results were published in [2]. Non-uniform heating of the powder material in the consolidated sample may be due to the non-uniform distribution of the current density along the radius of the cylindrical sample. This phenomenon is associated with the displacement of the current to the periphery as a result of the skin effect, as well as with a change in the conductivity of the powder during the flow of a powerful current pulse through it. The thickness of the skin layer - Δ is determined by the expression:

$$\Delta = (\sqrt{\mu\mu_0\omega/\rho})^{-1} \quad , \qquad (2)$$

where: μ – relative magnetic permeability, $\mu_0 = 4\pi \cdot 10^{-7}$ H/m, ρ – powder resistivity, ω – current pulse frequency. To obtain a consolidated sample with a uniform density, a uniform distribution of energy over the volume of the sample is necessary. The uniform distribution of the input energy is possible if the condition $R \le \Delta$ is satisfied, where R is the radius of the cylindrical sample. For example, for current pulses with a discharge frequency ω = 10 kHz, and for samples made of hard alloy powder (WC-Co20%) with a radius R = 5 mm, the value of the parameter R/Δ = 0.4, which ensures a fairly uniform distribution of the input energy along the radius of the sample. The temperature distribution along the height of the consolidated sample is determined by heat removal to the punch electrodes. As an example, Figure 1 shows the results of calculating the temperature in a hard alloy sample (WC-Co20%) for various times.

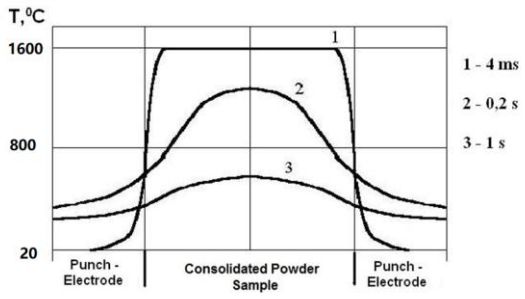

Fig. 1. *Temperature distribution along the axis of the consolidated sample.*

The calculation results (Figure 1) clearly show that the effect of heat removal during the first 4 ms manifests itself only in a narrow near-surface zone (200–300 microns) of the sample in contact with the punches. The short duration of exposure to high temperatures on

the consolidated powder material prevents grain growth and ensures the preservation of the original microstructure of the powder particles in the consolidated material.

3. Experimental method

High-voltage consolidation uses the constant pressure and high voltage pulse electric current to provide the resistive heating of powder sample by Joule effect. High voltage pulse electric current are generated by experimental equipment described in [3]. Registration of the parameters of a high-voltage current pulse and the intensity of thermal radiation of the consolidated powder materials was carried out using a measuring complex developed by the authors. This complex consists of a Rogowski coil with an integrating circuit, which registers the parameters of a high-voltage current pulse, photodiode sensors that register the intensity of thermal radiation, which is transmitted through a special optical waveguide from the consolidated powder materials, systems for triggering and synchronizing the components of the measuring complex. The radiation during high-voltage electric pulse consolidation of powder materials was recorded by a calibrated photodetector with a maximum sensitivity in the spectral range of 800–900 nm based on a silicon photodiode (FD-21 KP) with a fiber optic light guide diameter 1.5 mm. To calibrate the photodetector, a light-measuring tungsten tape lamp (SI 10-300U No. 70) calibrated for the spectral density of the energy brightness of radiation in the region from 300 nm to 2500 nm was used. A schematic diagram of the measurement of powder thermal radiation is shown in Fig. 2.

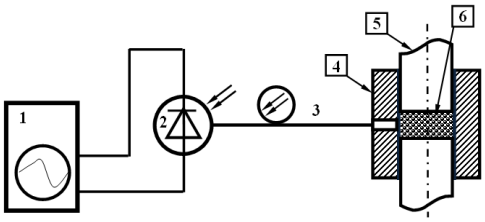

Fig. 2. *Scheme for measuring the thermal radiation of a powder during electropulse consolidation.*
1 - oscilloscope; 2 – photodiode; 3 - optical fiber (light guide); 4 – dielectric die; 5 - electrodes-punches; 6 – powder

The dielectric die is a hollow ceramic cylinder with a height of 30 mm, an inner diameter of 10 mm, and an outer diameter of 30 mm. The height of the powder filling is 10 mm. The compressive force of the punch electrodes provides a pressure on the powder of 20–25 MPa.

4. Results and Discussion

Testing of the measuring complex for recording electro-thermal parameters of high-voltage consolidation was carried out in experiments with copper powder. Fig. 3 and 4 show synchronous oscillograms of current pulses recorded using a Rogowski coil (in Fig. 3 the maximum value corresponds to current amplitude of 41 kA, and in Fig. 4 - 94 kA) and oscillograms of signals from a photodetector that registers the radiation of a powder material during consolidation process.

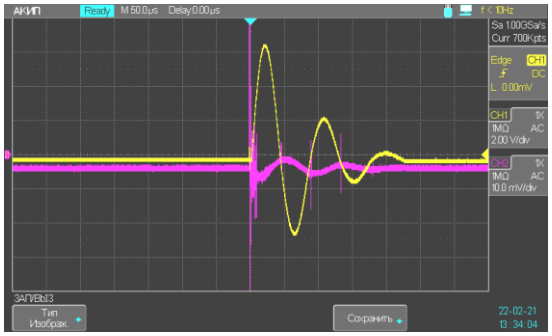

Fig. 3. *Synchronous oscillograms of current pulses (CH1) and the radiation of a powder material (CH2) during consolidation process (capacitive energy storage voltage U_{max} = 1.5 kV).*

Fig. 4. *Synchronous oscillograms of current pulses (CH1) and the radiation of a powder material (CH2) during consolidation process (capacitive energy storage voltage U_{max} = 3 kV).*

The radiation brightness of the studied sample B_{exp} was determined by comparison with the brightness of the reference sample B_{ref}, taking into account the corresponding solid angles Ω_{ref} and Ω_{exp}, the cross sections of the optical fiber (receiver) during calibration S_{et} and in the experiment S_{exp}, as well as the amplitudes of the photodetector signals during calibration U_{ref} and during experiments U_{exp} according to the following formula (3):

$$B_{exp} = B_{ref} \times \frac{\Omega_{ref} \cdot S_{ref} \cdot U_{exp}}{\Omega_{exp} \cdot S_{exp} \cdot U_{ref}} \quad (3)$$

The experimental value of the radiation brightness of the studied sample B_{exp} obtained in this way was compared with the brightness of the black body radiation at the effective wavelength of the calibrated photodetector (900 nm) using the Wien formula, which is true for the conditions of our experiments. Thus, from the ratio for the brightness of black body radiation (Wien's formula):

$$B_{exp} = \frac{2\pi hc^2}{\lambda^5} \times e^{\frac{hc}{\lambda kT}}, \quad (4)$$

where h is Planck's constant, c is the speed of light, λ is the radiation wavelength, k is Boltzmann's constant, and T is the desired brightness temperature of the source under study.

Based on the above approach, when processing the data of test experiments on electropulse consolidation of copper powder when charging the energy storage device to 3 kV, we obtain the amplitude value of the brightness temperature of the sintered sample of 1465 K, which slightly exceeds the value of the copper melting temperature of 1356 K under stationary conditions. When the voltage on the energy storage device decreases to 1.5 kV, the amplitude value of the brightness temperature of the consolidated copper sample, determined by this method, drops to 1366 K, which is only 10 degrees higher than the melting point of copper under stationary conditions.

Testing of the measuring complex capable of recording the electrothermal parameters of the impact on materials by a high-voltage current pulse was also carried out in experiments on high-voltage welding of dissimilar materials and in electric discharges in water.

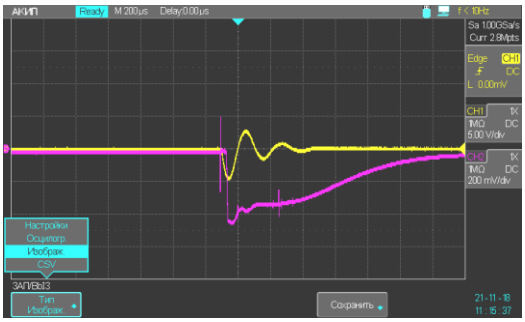

Fig. 5. *Synchronous oscillograms of current pulse (CH1) and the radiation (CH2) of the contact zone of Fe-Cu metal welding (capacitive energy storage voltage Umax = 2.2 kV).*

Fig. 5 shows synchronous oscillograms of a current pulse (the maximum value corresponds to current amplitude of 29 kA) and a photodetector signal that records the radiation of the contact zone of Fe-Cu metal welding.

Certain values of the brightness temperature of the area of resistance welding of Cu-Fe in air are T = 2048 ± 50 K. It should be noted that the obtained values of the brightness temperature in the area of contact welding significantly exceed the melting temperatures of copper and iron under stationary conditions in air.

With an electric pulse discharge in water, an expanding brightly luminous gas-vapor bubble is formed with hot vapors of water and electrode material, the dimensions of which are many times greater than the dimensions of the input window of the photodetector. This leads to an overestimation of the value of the spectral brightness of the discharge region, and, as a result, to an overestimated value of the brightness temperature of the discharge region. In addition, under the conditions of an electric pulse discharge in water, a noticeable contribution from the radiation of the intense spectral line of oxygen at 777 nm is possible, which can also lead to an overestimation of the brightness temperature measured by a calibrated photodiode with a maximum spectral sensitivity of the photodetector in the region of ~900 nm. Therefore, the obtained value of the brightness temperature of the electric pulse discharge in water T = 4140 K is overestimated.

Fig. 6 shows synchronous oscillograms of a current pulse (the maximum value corresponds to a current amplitude of 8.8 kA) and a photodetector signal that records the radiation of electropulse discharge in water.

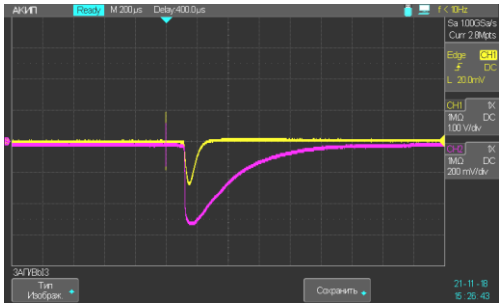

Fig. 6. *Synchronous oscillograms of current pulse (CH1) and the radiation (CH2) of the electropulse discharge in water (capacitive energy storage voltage Umax = 1.5 kV).*

Experimental studies of the parameters of high-voltage electric impulse action during the consolidation of high-temperature HfC powder compositions have been carried out. As an example, Fig. 7 and 8 show the microstructures of consolidated HfC samples in various modes of high-voltage consolidation.

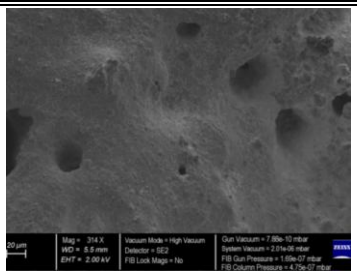

Fig. 7*. The structure of HfC consolidated at the cumulative mode.*

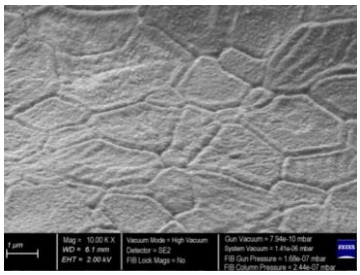

Fig. 8. *The structure of HfC consolidated at the optimum mode.*

Fig. 7 shows a photograph of the microstructure of a hafnium carbide sample obtained in the cumulative mode [1] of high-voltage consolidation. The optimal mode of high-voltage consolidation of HfC powder makes it possible to obtain a high-density consolidated sample, the microstructure of which is shown in Fig. 8.

5. Conclusion

It is worth mentioning that the fabrication of high-density refractory samples by the HVC method requires accurate identification of the optimal values of the pulsed current amplitude applied to the specimen since the optimal values of this parameter are close to the critical ones, which define the boundary between stable and unstable modes of HVC.

6. References

1. E. Grigoryev, M. Abedi, V.Goltsev, A. Osintsev, A. Plotnikov, D. Moskovskikh, Metall Mater Trans B, **53**, 1552 (2022)
2. E. Grigoryev G., E. Olevsky, Scr. Mater., 66, 662 (2012)
3. E. Strizhakov, S. Neskoromny, D. Minko, *Discharge-pulse processing of materials* (Rostov - on - Don: DSTU, 2016)

Modified assembly for spraying fine powder

Aliaksandr Ilyushchanka[1, 2], Iryna Charniak[2], Aleksey Kusin[2], Ruslan Kusin[3], Yriy Filippov[4], Evgeniy Eremin[4]
State research and production powder metallurgy association[1] – Minsk, Republic of Belarus
State Scientific Institution "O.V. Roman Powder Metallurgy Institute" [2] – Minsk, Republic of Belarus
Educational establishment "Belarus State and Agrarian Technical University" [3] – Minsk, Republic of Belarus
Omsk State Technical University [4] – Omsk, Russia

E-mail: alexil@mail.belpak.by, irinacharniak@tut.by, 2312444@mail.ru, 19081877@mail.ru, weld_techn@mail.ru

Abstract: *The results of testing a nozzle with a zero angle of attack for obtaining atomized metal powders are presented, which indicate its increased overhaul life, a satisfactory yield of fine fraction powders with a good spherical powder shape.*
KEYWORDS*: INSTALLATION FOR OBTAINING POWDERS, SPRAYING UNIT, SHOWER, SPRAYED BRONZE POWDERS*

1. Introduction

One of the ways to increase the powders yield of fine fractions obtained by dispersing a metal melt with a gas flow is a nozzle developed on the basis of a Laval nozzle, which ensures an increase in the yield of fine powder fractions up to 80% [1, 2]. However, the developed nozzle has a relatively short overhaul period of the spraying unit, associated with the sticking of melt particles on the lower end of the nozzle for the outflow of the melt jet, and therefore, it is necessary to stop work and replace the part in the spraying unit. As a result, the output of fine powder per shift due to time losses is no more than 6 kg (which corresponds to the weight of the melt in one crucible).

Work purpose - study of the possibility of increasing the overhaul life of the nozzle, developed on the basis of the Laval nozzle, by changing the direction of the gas flow.

2. Experiment results and their discussion

To solve this issue, a small-sized installation was developed to study the processes of obtaining and producing copper-based powders (Fig. 1).

For the experiments, a spray assembly was made, in which the nozzle had a zero angle of attack (Figure 1). It was assumed that this would prevent sticking of metal to the end of the pipe for the outflow of the melt jet, and the process of dispersion of the melt jet would occur due to ejection and a sharp expansion of the air flow.

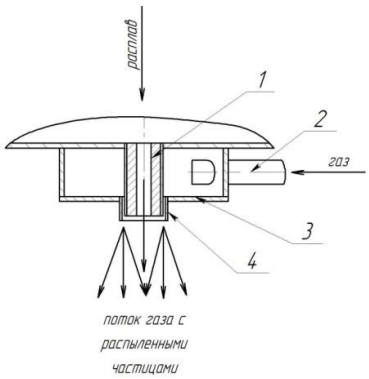

Fig. 1. *The design of the spray unit: 1 - ceramic branch pipe for the outflow of the melt jet; 2 - branch pipe for supplying gas-energy carrier; 3 - nozzle; 4 - nozzle*

Approbation of the nozzle design was carried out as part of a laboratory installation with a metal receiver capacity of up to 10 kg (nominal volume 6 kg).

The appearance of the installation during the spraying process is shown in Figure 2.

Fig. 2. *The process of spraying copper-based powders*

The experiments were carried out in the preparation of powders of tin-phosphorous bronze of the BrO10F1 grade (the charge included copper, tin of the O1 grade, and phosphorous copper of the MF 10 grade). The melt was overheated by 2500 s above the melting point of copper. Within no more than 30 seconds from the moment of readiness, the melt entered the metal receiver and then into the nozzle, which was simultaneously supplied with compressed air. The dispersed powder particles were cooled in water located in the lower part of the apparatus housing. Then the powder was dried in an oven for 2.5 hours at a temperature of 110–120°C, its granulometric composition was determined by sieve analysis, and the shape factor was studied according to the method [3] using the Mini-Magiskan automatic image analyzer by Joyce Loebl . The appearance of the powder is shown in Figure 3, the granulometric composition (averaged data for four experimental batches of powder are given) - in Figure 4. The shape factor was in the range of 0.95-0.97.

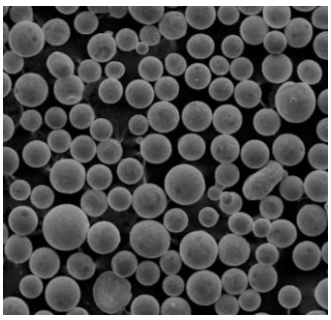

Fig. 3. *Appearance of the manufactured powder*

Fig. 4. *Particle size distribution histogram of manufactured powder*

In the experiments course, 40 kg of powder was produced, after which it became necessary to replace the nozzle for the outflow of the melt jet, that is, in comparison with the previous design, the service life was increased by more than 6 times. However, despite the fact that the yield of fine fractions is quite high (at the level of 75% of particles with sizes less than 160 μm), it decreased by 5–10% [4] (depending on the particle size (up to 160 or 100 μm). On the whole, it can be concluded that it is expedient to use the proposed nozzle design.

Conclusion. The results of testing a nozzle with a zero angle of attack for obtaining atomized metal powders are presented, which indicate its increased overhaul life, a satisfactory yield of fine fraction powders with a good spherical shape of the powder. It has been established that, compared with the previous design, the service life can be increased by more than 6 times. At the same time, the yield of fine fractions is quite high (at the level of 75% of particles with sizes less than 160 μm), although it decreased by 5-10%. In general, it can be concluded that it's expedient to use the proposed nozzle design.

4. References

1. Kusin R.A., Kaptsevich V.M., Charniak I.N., Kusin A.R., Zhegzdrin D.I. A new nozzles design for the production of spherical fine powders by spraying the metal melt with air. Surface engineering. New powder composite materials. Welding. Minsk: Institute of Powder Metallurgy SSPI PM NAS of Belarus, 2009. P. 2. P. 218-222. (R. Kusin, V. Kaptsevich, I. Charniak, A. Kusin, D. Zhegzdrin).

2. Ilyushchanka A.Ph., Kusin R.A., Charniak I.N., Zhegzdrin D.I., Dechko M.M., Manoilo E.D., Radchenko A.A., Ignatovich Z.V. Investigation of the process of obtaining powders based on aluminum by the method of spraying a melt jet with a gas stream / Powder metallurgy: Minsk: Belarusian science, 2014. Is. 37. pp. 34-38. **(**A. Ilyushchanka, R. Kusin, I.Charniak, D. Zhegzdrin, M. Dechko, E. Manoilo, A. Radchenko, Z. Ignatovich).

3. Vityaz P.A., Kaptsevich V.M., Sheleg V.K. Porous powder materials and products from them / Minsk, Vysh. school (1987). (P. Vityaz, V. Kaptsevich, V. Sheleg).

4. Ilyushchanka A. Kusin R.A, Manoylo E.D., Charniak I.M, Kusin A.R., Yurchanka S.O., Staselka A.S., Maiseyeva A.Ya, Kurylchyk I.D., Semenov V.I. Application of sprayed bronze powders of the BrSn10Ph1 and BrSn5Zn5Pb5 brands for applying protective coatings by gas-flame spraying. Nonequilibrium phase transformations. Bulgaria. 2021, Year VII, Is. 2. P.67-69. (A. Ilyushchanka, R. Kusin, E. Manoylo, I. Charniak, A. Kusin, S. Yurchanka, A. Staselka, A. Maiseyeva, I. Kurylchyk, V. Semenov).

Formation of nonequilibrium phases and preparation of advanced materials by mechanochemical method

Zara P. Cherkezova-Zheleva[1], Daniela G. Paneva[1], Iakovos Yakoumis[2], Dinos Sakkas[3]
Institute of Catalysis, Bulgarian Academy of Sciences, Acad. G. Bonchev Str., Bld. 11, Sofia 1113, Bulgaria[1]
MONOLITHOS Catalysts and Recycling Ltd, Athens, Greece[2]
YS Cypriot Catalysts Ltd., Psevdas, Cyprus[3]
zzhel@ic.bas.bg

Abstract: *Mechanochemical activation is recognized as a green and sustainable method for preparation of different advanced materials, incl. highly active and selective catalysts for chemical and automotive industry.*
The study investigates the possibility of preparation of advanced materials with unique properties and the formation of nonequilibrium phases by application of mechanochemical method. Numerous laboratory experiments revealed the possibilities for the design of mechanochemical reactions toward environmentally friendly, sustainable and economical synthesis of target materials. An important part of the investigation is the physicochemical characterization of mechanochemically processed materials. Special attention is paid to follow the changes of material composition at different stages of the treatment, as well as and the formation of nonequilibrium phases, which cannot be obtained by conventional synthesis methods.
The paper is a step toward the development of the scientific foundations of mechanochemistry by studying and modelling the multidirectional processes that take place in mechanochemically treated materials. Such investigations are of high practical importance for selection of mechanochemical reactions with potential industrial application

1. Introduction

Mechanochemical activation is recognized as a green and sustainable method for preparation of different advanced materials, incl. highly active and selective catalysts for chemical and automotive industry.

2. Problem discussion

Strategies and approaches for development of next generation advanced materials are connected to an improvement and optimization of methods of preparation and processing of new high-technology materials working . Special attention is paid on nanoscale materials - either in the form of bulk nanomaterials or in hierarchically organised structures. The produced new materials come with their new challenges: nanometrology - study of nanoparticles, single and multilayers and in situ studies, 3D element mapping, etc.

The main purpose of this work is to develop a model for an effective application of mechanochemical method toward formation of nonequilibrium phases and preparation of advanced materials.

An important part of the investigation is the physicochemical characterization of mechanochemically processed materials. Special attention is paid to follow the changes of material composition at different stages of the treatment, as well as and the formation of nonequilibrium phases, which cannot be obtained by conventional synthesis methods.

3. Objective and research methodologies

The study investigates the possibility of preparation of advanced materials with unique properties and the formation of nonequilibrium phases by application of mechanochemical method. Numerous laboratory experiments revealed the possibilities for the design of mechanochemical reactions toward synthesis of target materials by environmentally friendly, sustainable and economical synthesis.

Mechanical processing:
planetary ball-mill (PM-100, Retsch, Germany) under an ambient or inert atmosphere using numerous reactors and balls made by different materials.

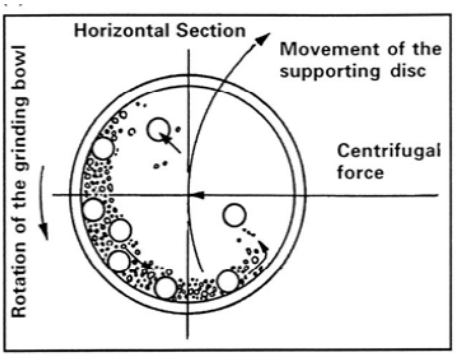

High-Energy Milling
Planetary mills exploit the principle of centrifugal acceleration instead of gravitational acceleration. The enhancement of the forces acting on the balls in relation to the conventional ball mill is achieved by the combined action of two centrifugal fields. The charge inside vials performs two relative motions: a rotary motion around the mill axis and a planetary motion around the vial axis. By observing certain conditions, these mills produce high mechanical activation after a relatively short milling time and at room temperature. The energy density in these mills is 100–1000 higher than the energy density used earlier in conventional milling equipment. So, preparation of advanced materials with unique properties and the formation of nonequilibrium phases by application of mechanochemical method and high energy ball milling.

Advanced characterisation of materials
Collection of process-relevant data are very important in order to build a complete understanding of the reaction mechanism and to obtain the suitable treatment mechanochemical conditions (i.e. milling agents and additives, ball milling parameters, etc.).

4. Conclusion

The paper is a step toward the development of the scientific foundations of mechanochemistry by studying and modelling the multidirectional processes that take place in mechanochemically treated materials. Such investigations are of high practical importance for selection of mechanochemical reactions with potential industrial application

.

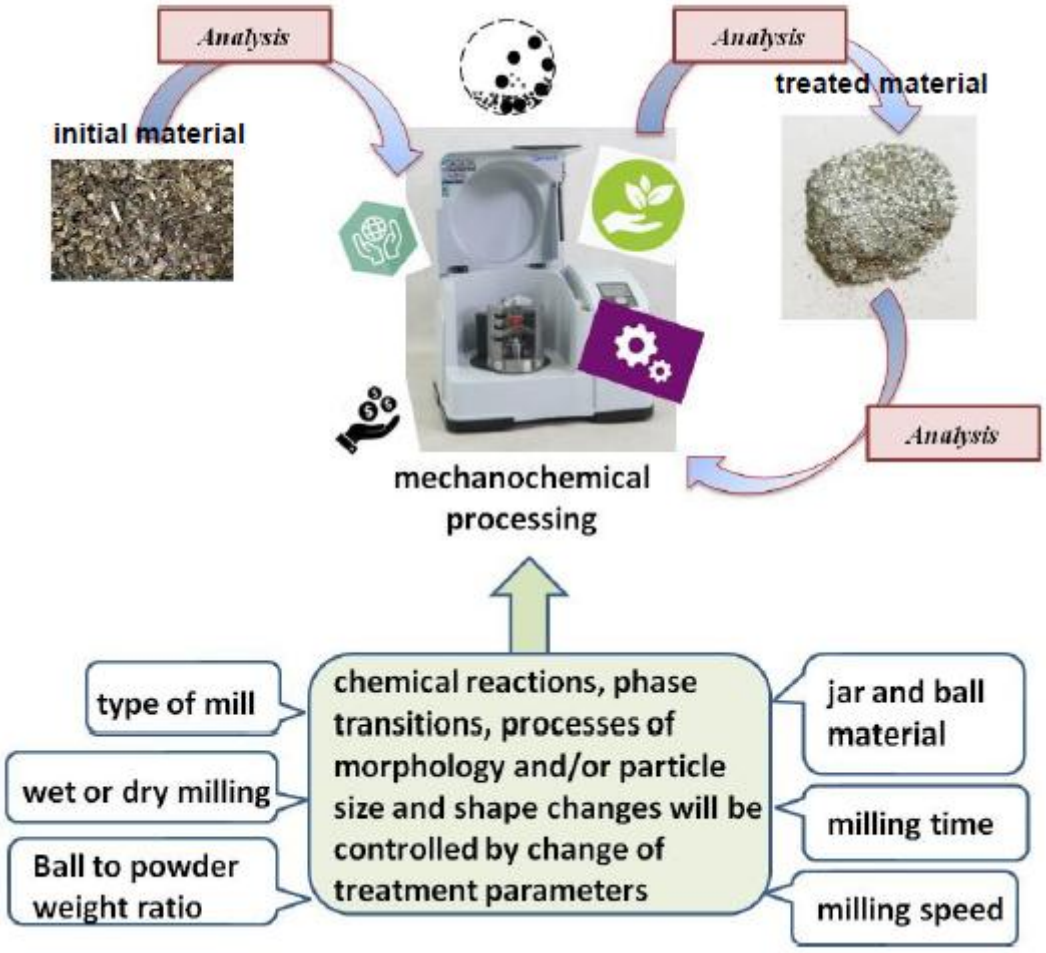

Acknowledgements:

The authors gratefully acknowledge the financial support of the Bulgarian National Science Fund at the Ministry of Education and Science - Project № КП-06-КОСТ/18/ 2019 and the project COST Action CA 18112 “Mechanochemistry for Sustainable Industry” (Mech@SustInd), supported by COST (European Cooperation in Science and Technology). This article is also based on the project activities of H2020-MSCA-RISE-2020 101007669: Chemistry of Platinum Group Metals, CHemPGM.

5. References

1. V. P. Balema in Materials Challenges in Alternative Energy, Wiley, 2011, p. 25.
2. Baláž, P.; Achimovičová, M.; Baláž, M.; Billik, P.; Cherkezova-Zheleva, Z.; Criado, J.M.; Delogu, F.; Dutková, E.; Gaffet, E.; Gotor, F.J.; et al. Hallmarks of Mechanochemistry: From Nanoparticles to Technology. Chem. Soc. Rev. 2013, 42, 7571–7637.
3. Baláž, M. Environmental Mechanochemistry, Recycling Waste into Materials Using High-Energy Ball Milling, Springer Nature Switzerland AG, 2021.
3. Ahluwalia, V.K.; Kidwai, M. Organic Synthesis in Solid State. In New Trends in Green Chemistry; Springer: Dordrecht, The Netherlands, 2004; pp. 189–231.
4. Varma, R.S. Greener and Sustainable Trends in Synthesis of Organics and Nanomaterials. ACS Sustain. Chem. Eng. 2016, 4, 5866–5878.
5. Anastas, P.T.; Warner, J.C. Green Chemistry: Theory and Practice; Oxford University Press: Oxford, UK, 1998; ISBN 9780198502340.
6. Tang, S.L.Y.; Smith, R.L.; Poliakoff, M. Principles of Green Chemistry: PRODUCTIVELY. Green Chem. 2005, 7, 761–762.

Усовершенствование методики расчета количества образующихся фаз в углеродистых сталях

Бобырь С.В., д.т.н, с.н.с., Парусов Э. В., д.т.н., с.н.с., Голубенко Т. М., к.т.н, Лошкарев Д. В.
Институт черной металлургии им. З. И. Некрасова НАН Украины, office.isi@nas.gov.ua

Improvement of calculating method for the number of phases formed in carbon steels

Bobyr S. V., Parusov E. V., Golubenko T. M., Loshkarev D. V.
Iron and Steel Institute Z. I. Nekrasov of NAS of Ukraine

КЛЮЧОВІ СЛОВА*: ФІЗИКО-ХІМІЧНЕ МОДЕЛЮВАННЯ, ФАЗОВІ ПЕРЕТВОРЕННЯ, ЛЕГОВАНІ СТАЛІ, ОХОЛОДЖЕННЯ, НЕРІВНОВАЖНА ТЕРМОДИНАМІКА, СТРУКТУРНІ ДІАГРАМИ.*
KEYWORDS: *PHYSICOCHEMICAL MODELING, PHASE TRANSFORMATION, ALLOY STEELS, COOLING, NONEQUILIBRIUM THERMODYNAMICS, STRUCTURAL DIAGRAMS.*

Modern studies on the modeling of phase transformations in low-alloy steels to a certain extent allow solving the problem of quantitative determination of phase transformations for a given chemical composition of steel and different cooling rates. However, the capabilities of the available universal software products for the analysis of complexly alloyed steels are currently very limited. To conduct research, steels 25Cr2Mo1V and 38CrNi3MoV and existing analytical models were used, which were adapted to carry out the corresponding calculations. Structural diagrams are plotted for the steels under study depending on the rate of continuous cooling. The amount of residual austenite was taken into account by the developed method for the first time. Steel 25Cr2Mo1V, with continuous cooling at a rate of 1.0 °C/s (conditions close to natural air cooling), consists of 18 % ferrite, 1 % pearlite, 80 % bainite and 1 % residual austenite. Steel 38CrNi3MoV cooled at a rate of 1.0 °C/s consists of 2 % ferrite, 47.5 % bainite, 50 % martensite and 0.5 % retained austenite. It is shown that for the conditions of natural air cooling, the calculated data correlate well with practical results.

На данный момент известно теоретическое выражение, позволяющее рассчитывать количество мартенсита, образующегося во время фазового превращения в углеродистых сталях:

$$n_\alpha = n_{\alpha 0} + L_{12} \cdot \sigma_\gamma \qquad (1),$$

где $n_{\alpha 0}$ – количество мартенсита, которое образуется при отсутствии напряжений в γ фазе; L_{12} – коэффициент, который зависит от размера структурных составляющих и определяется температурой превращения; σ_γ – напряжения в аустените.

Величина $n_{\alpha 0}$ может быть рассчитана по известной формуле Коэстинена-Марбургера:

$$n_{\alpha 0} = A_m \left\{1 - \exp\left[-K_\alpha \left(M_s - T\right)\right]\right\} \qquad (2),$$

где M_s – температура начала образования мартенсита; A_m – количество аустенита в структуре стали в критической точке M_s; K_α – эмпирический коэффициент, характеризующий скорость образования мартенсита вблизи температуры M_s (зависит от химического состава стали и параметров обработки).

Недостатком формулы (2) является то, что она учитывает только температуру начала образования мартенсита M_s. Ввиду изложенного, авторами разработана и предложена модифицированная формула Коестинена-Марбургера, которая также учитывает температуру окончания мартенситного превращения (M_f):

$$n_{\alpha 0} = A_m (1 - \exp\left(-K_\alpha \frac{M_s - T}{T - M_f} \right)) \qquad (3).$$

Учет температуры окончания мартенситного превращения (M_f) позволяет получить более достоверные прогнозные значения. По результатам проведенного моделирования превращения аустенита с использованием различных методик и сравнения их между собой: по формуле (2), а также предложенной усовершенствованной формуле (3) и по формуле (3) с K_α = 6,84 и K_α = 1,0, было получено следующее. Разница между функциями (2) и (3) проявляется при отрицательных температурах. Усовершенствованная формула (3) позволяет при изменении эмпирического коэффициента (K_α) описывать разнообразную кинетику превращения аустенита в мартенсит, поэтому она является более универсальной, чем существующая, и используется в настоящее время для прогнозного расчета количества мартенсита в углеродистых сталях широкого марочного состава.

Получаване, охарактеризиране и потенциални приложения на нановлакнести полимерни материали, съдържащи клиохинол

Наско Начев[1], Мария Спасова[1], Милена Игнатова[1], Невена Манолова[1], Илия Рашков[1], Младен Найденов[2]

[1] Лаборатория "Биологично активни полимери", Институт по полимери, Българска академия на науките, бл. 103А, 1113 София, България

[2] Катедра "Микробиология и екологични биотехнологии", Аграрен Университет, 4000 Пловдив, България

Болестта еска е една от най-ранно описаните болести по лозата, която разрушава дървесината и предизвиква увяхване на лозовите насаждения. Известно е, че причинители на болестта са гъби най-често от видовете *Phaeomoniella chlamydospora* и *Phaeoacremonium aleophilum*. Целта на настоящото изследване е да се получат влакнести материали на основата на биоразградимите и биосъвместими поли(3-хидроксибутират) (PHB), поливинилпиролидон (PVP) и 5-хлор-7-йод-8-хидроксихинолин (клиохинол, CQ) с противогъбична активност спрямо *Phaeomoniella chlamydospora* и *Phaeoacremonium aleophilum* чрез електроовлакняване или едновременно провеждане на електроовлакняване и електроразпръскване.

Схематично представяне и СЕМ микрографии на влакнестите материали

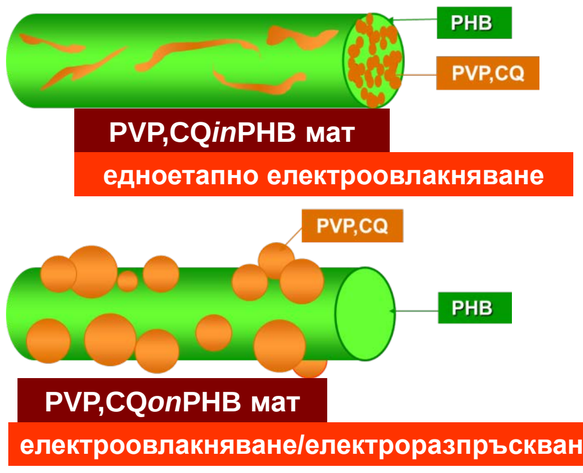

5-хлор-7-йод-8-хидроксихинолин (клиохинол) (CQ)

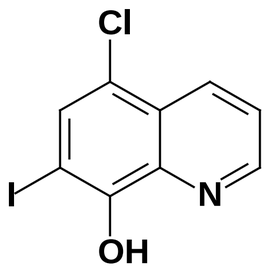

антимикробна и противогъбична активност

PVP*in*PHB

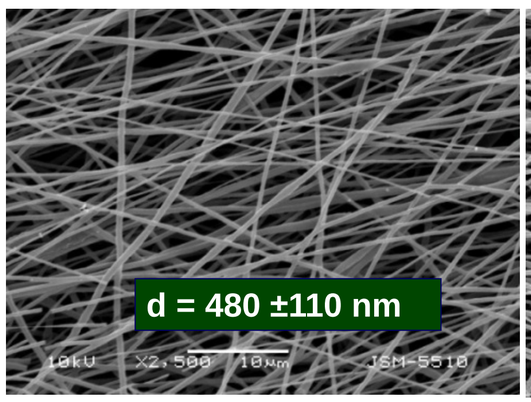

PVP,CQ*in*PHB

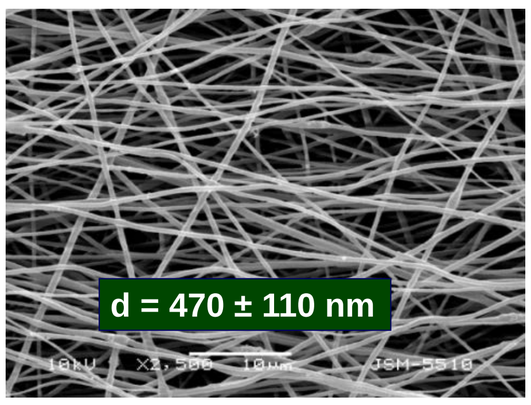

PVP,CQ*on*PHB

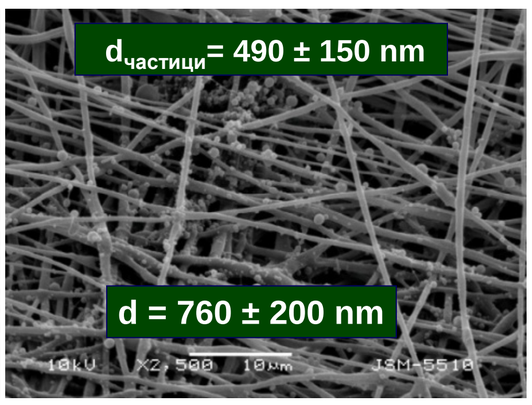

Контактен ъгъл на омокряне

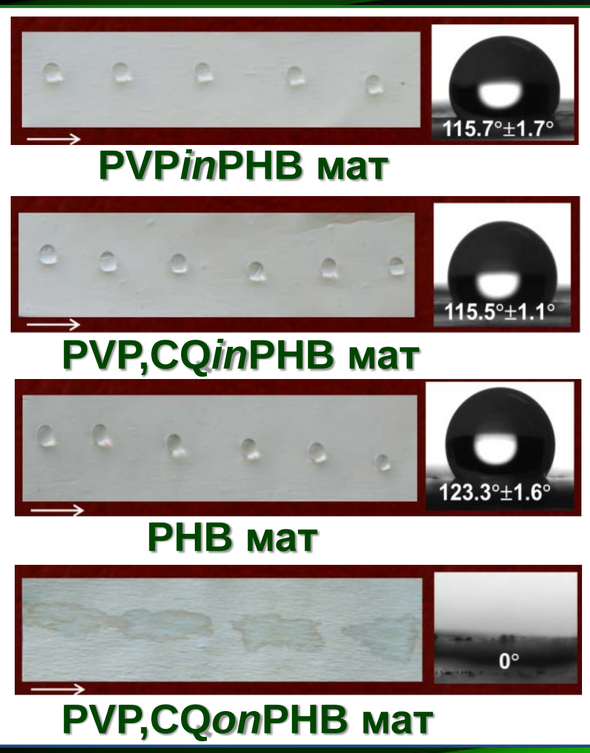

Рентгеноструктурен анализ

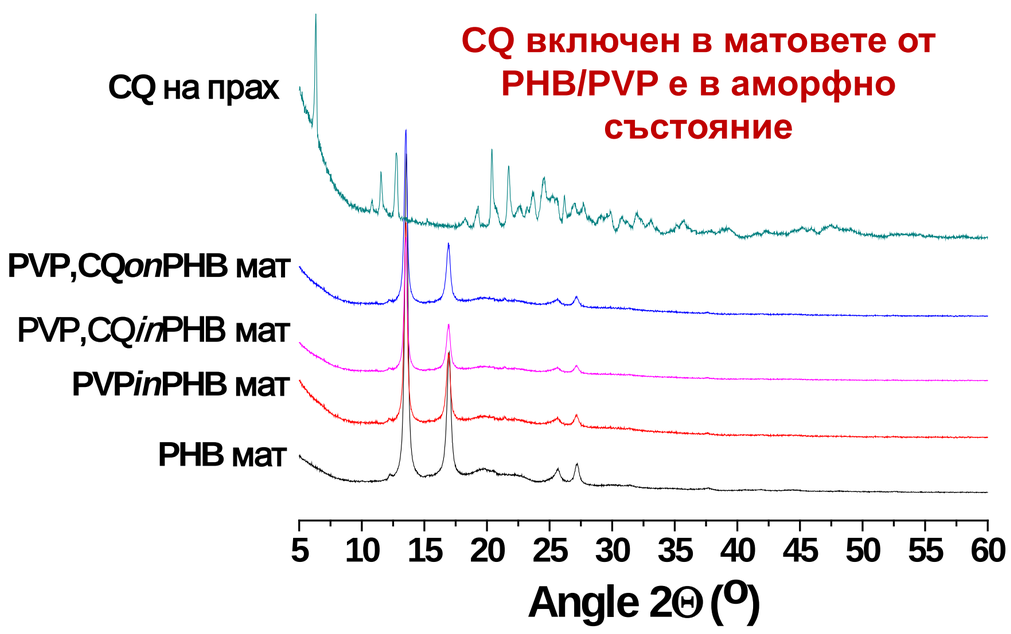

CQ включен в матовете от PHB/PVP е в аморфно състояние

ДСК

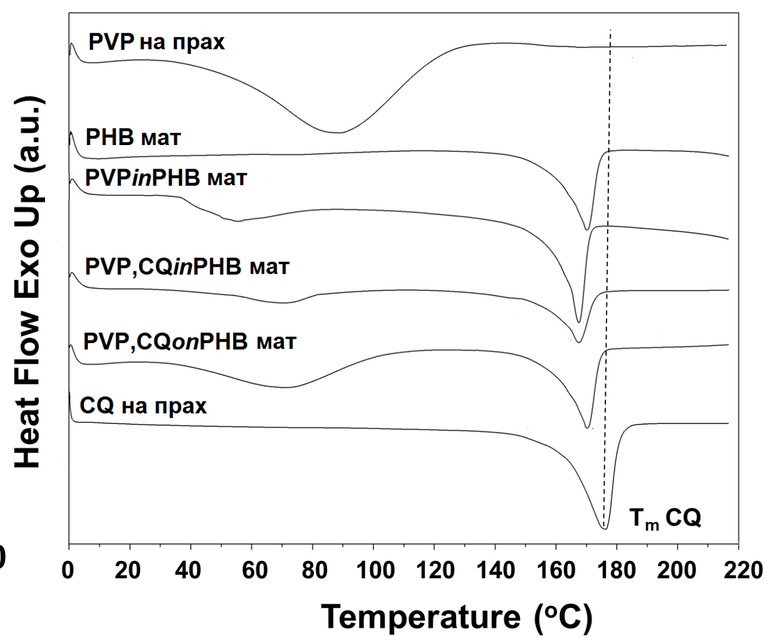

Профил на освобождаване на CQ

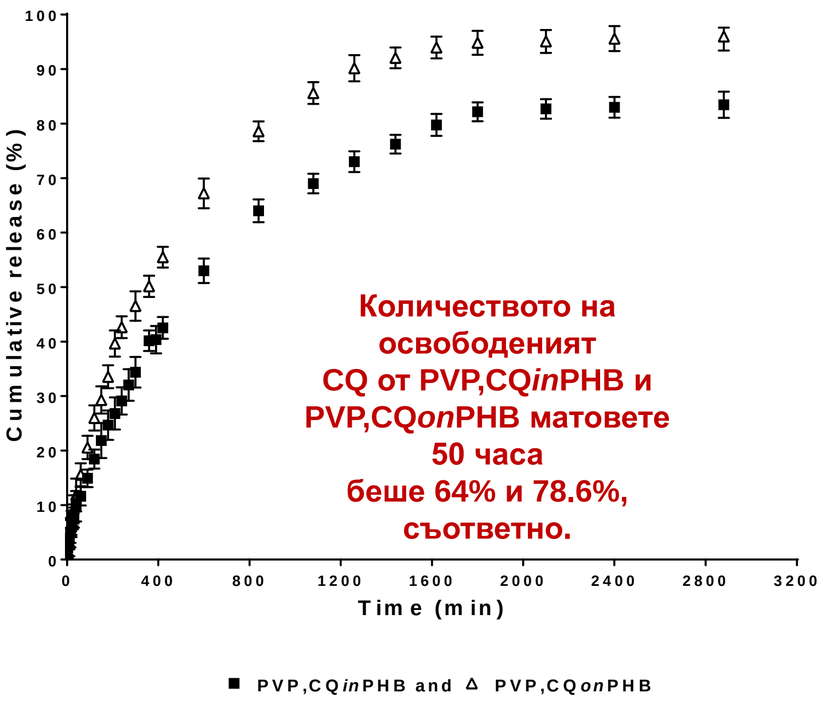

Количеството на освободеният CQ от PVP,CQ*in*PHB и PVP,CQ*on*PHB матовете 50 часа беше 64% и 78.6%, съответно.

Противогъбична активност

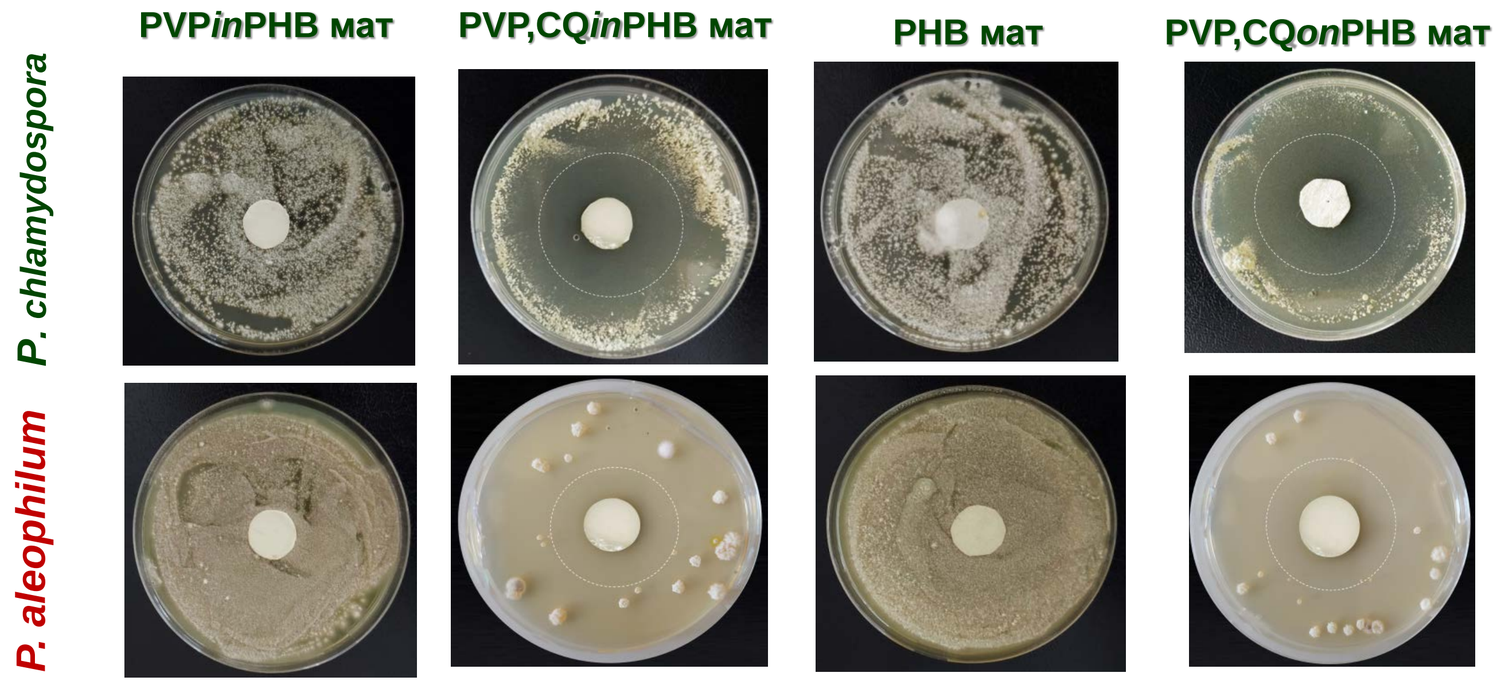

Заключение: Успешно бяха получени нови влакнести материали съдържащи CQ с оригинален дизайн чрез електроовлакняване (стратегия *"in"*) или едновременно електроовлакняване и електроразпръскване (стратегия *"on"*). Установено беше, че CQ включен в матовете от PHB/PVP е в аморфно състояние. Влакнестите материали (тип "*in*" и "*on*"), съдържащи CQ проявяват значителна противогъбична активност спрямо *P. chlamydospora* и *P. aleophilum*. Тези свойства правят получените влакнести материали обещаващи кандидати като активни протектори за приложение в селското стопанство за предпазване на лозови растения от проникването и развитието на двата главни гъбични агента предизвикващи заболяването еска.

Литература: [1] Ignatova M.; Nachev N.; Spasova M.; Manolova N.; Rashkov I.; Naydenov M. Electrospun 5-chloro-7-iodo-8-hydroxyquinoline (clioquinol)-containing poly(3-hydroxybutyrate)/polyvinylpyrrolidone antifungal materials prospective as active dressings against esca. *Polymers*, **2022**, 14, 367, 1-17.

Благодарности: Авторите изказват своята благодарност на ФНИ (Договор КП-06-ОПР03/2) за финансовата подкрепа.

Dendrite growth in an inclined flow

Titova E. A.[1, a)] Alexandrov D. V.[2]
[1]Department of Theoretical and Mathematical Physics, Laboratory of mathematical modeling of physical and chemical processes in multiphase media, Ural Federal University, Ekaterinburg, 620000, Russian Federation
[2]Department of Theoretical and Mathematical Physics, Laboratory of Multi-Scale Mathematical Modeling, Ural Federal University, Ekaterinburg, 620000, Russian Federation
[a)]Corresponding author: eatitova@urfu.ru

Abstract: *Crystal growth is always accompanied by liquid melt flux caused by gravity and temperature gradient. The convective contribution to heat transport can exceed the contribution from heat diffusion, which leads to the fact that the flow near the crystal will determine the dynamics of interfacial boundary motion. For example, involuntary flow instabilities caused by crystal and crucible rotation during extraction of a monocrystal from the melt (Czochralski method) lead to growth of spiral shapes of monocrystals of some oxides.*

The theory of boundary integrals is one of effective methods for solving heat and mass transfer problems with a moving boundary. The extension of this theory to the case of convective fluid flows allows one to significantly extend the class of problems with a moving boundary to be solved.

The boundary integral approach based on the Green's function allows to pass from the linear heat conduction equation with given boundary conditions to the general integro-differential equation that determines the shape of the interface depending on the total undercooling of the system [1, 2]. For a nonlinear equation in the presence of convection, a Green's function corresponding to a linear problem was proposed in [3]. In this case, the boundary integral is divided into two separate contributions, one of which corresponds to the motion of the front in the stationary melt. The convective contribution to the boundary integral contains a temperature gradient, so that consideration of convection leads to the fact that the shape of the interface depends on undercooling and the unknown temperature gradient. Integrating the Green's function with respect to time and interface, the solution of the boundary problem can be found in the form of the integro-differential boundary equation that determines the relationship between the shape of the interfacial surface and undercooling. The solution of the integro-differential boundary equation taking into account convection determines the effect of melt motion on the shape of the interface, and, thus, allows selecting a flow regime leading to the desired surface shape.

In this work, the growth of a single dendrite in an inclined flow is investigated. The undercooling at the dendrite surface as a function of Peclet, Reynolds, Prandtl numbers and flow inclination angle was obtained. It is shown that the found analytical solution has limit transitions to the previously known ones for the axisymmetric flow.

References:

1. J.S. Langer, Acta Metall. **25**, 1121–1137 (1977).
2. D.V. Alexandrov and P.K. Galenko, Physica A **469**. 420–428 (2017)
3. D. A. Saville and P. J. Beaghton, Phys Rev. A **37** 3423–3430 (1988).

Creation of porous titanium materials assisted blended elemental powder metallurgy

Oleksandr Stasiuk, Denys Oryshych
G.V. Kurdyumov Institute for Metal Physics N.A.S. of Ukraine, Kyiv, Ukraine

Titanium alloys has found acceptance in many areas due to their unique physical and mechanical properties. The creation of porous titanium products with the best specific strength is one of the most promising areas of damping materials development. Nowadays, titanium products obtained by traditional technologies (casting and hot deformation) are quite expensive. This aspect limits their usage, thus the economic technologies development for their production is an important area of research. **The aim** of the work is to establish the general principles of porous structure formation in titanium materials, factors and mechanisms that can effect on the controlled pore formation process.

Creation of biomedical alloys based on the Ti-Zr system from pre-alloyed hydride mixtures by powder metallurgy

Oleksandr Stasiuk, Denys Oryshych, Volodymyr Dekhtyarenko

G.V. Kurdyumov Institute for Metal Physics N.A.S. of Ukraine, Kyiv, Ukraine

Today, when obtaining biomedical alloys using powder technology, their additional processing after synthesis (cold and hot deformation) is necessary, and this, in turn, significantly complicates the production technology and increases the cost of finished products. In order to obtain a sufficient complex of physical and mechanical properties, in this work, it was proposed to use hydrides of previously obtained alloys, not simple metals, as starting materials. The main advantage of this approach is that hydrogen in the involved technological approach is only a temporary alloying element. Being released from the crystal lattice of the metal, during high-temperature synthesis, hydrogen leads to phase transformations that ensure the formation of highly defective states of dehydrogenated particles, which significantly activates diffusion processes and accelerates the formation of homogeneous alloys.